UNIVERSIDADE ESTADUAL DE PONTA GROSSA
SETOR DE CIÊNCIAS EXATAS E NATURAIS
PROGRAMA DE PÓS-GRADUAÇÃO EM CIÊNCIAS

ENRIQUE CHIPICOSKI GABRICK

COMPLEX DYNAMICS IN A SEASONAL INFECTIOUS DISEASE MODEL
DINÂMICA COMPLEXA EM UM MODELO PARA DOENÇAS INFECCIOSAS SAZONAIS

PONTA GROSSA
2025

ENRIQUE CHIPICOSKI GABRICK

COMPLEX DYNAMICS IN A SEASONAL INFECTIOUS DISEASE MODEL
DINÂMICA COMPLEXA EM UM MODELO PARA DOENÇAS INFECCIOSAS SAZONAIS

Thesis presented to the Graduate Program in Sciences, concentration area Physics, of the Universidade Estadual de Ponta Grossa, in partial fulfillment of the requirements for the degree of Doctor in Science.

Advisor: Prof. Dr. Antonio Marcos Batista.

Co-advisor: Prof. Dr. Dr. h.c. mult. Jürgen Kurths.

PONTA GROSSA

2025

Gabrick, Enrique Chipicoski
G117 Complex dynamics in a seasonal infectious disease model / Enrique Chipicoski Gabrick. Ponta Grossa, 2025.
91 f.

Tese (Doutorado em Ciências - Área de Concentração: Física), Universidade Estadual de Ponta Grossa.

Orientador: Prof. Dr. Antonio Marcos Batista.
Coorientador: Prof. Dr. Jürgen Kurths.

1. Seirs. 2. Seasonal infectious disease. 3. Chaos. 4. Multistability. 5. Vaccination. I. Batista, Antonio Marcos. II. Kurths, Jürgen. III. Universidade Estadual de Ponta Grossa. Física. IV.T.

CDD: 530

Ficha catalográfica elaborada por Maria Luzia Fernandes Bertholino dos Santos- CRB9/986

TERMO DE APROVAÇÃO

ENRIQUE CHIPICOSKI GABRICK

COMPLEX DYNAMICS IN A SEASONAL INFECTIOUS DISEASE MODEL

Tese aprovada como requisito parcial para obtenção do grau de Doutor em Ciências, no Programa de Pós-Graduação em Ciências, Área de Concentração Física Teórica, da Universidade Estadual de Ponta Grossa, pela seguinte banca examinadora:

gov.br Documento assinado digitalmente
ANTONIO MARCOS BATISTA
Data: 10/02/2025 12:33:00-0300
Verifique em https://validar.iti.gov.br

Orientador- _____

Dr. Antonio Marcos Batista – UEPG –

Titular/Presidente

gov.br Documento assinado digitalmente
ERVIN KAMINSKI LENZI
Data: 10/02/2025 10:47:52-0300
Verifique em https://validar.iti.gov.br

_____

Dr. Ervin Kaminski Lenzi – UEM – Titular

gov.br Documento assinado digitalmente
HAROLDO VALENTIN RIBEIRO
Data: 10/02/2025 10:50:24-0300
Verifique em https://validar.iti.gov.br

_____ _____

Dr. Haroldo Valentin Ribeiro – UEM – Titular

gov.br Documento assinado digitalmente
ANTONIO SERGIO MAGALHAES DE CASTRO
Data: 10/02/2025 11:50:04-0300
Verifique em https://validar.iti.gov.br

_____

Dr. Antonio Sérgio Magalhães de Castro – UEPG – Titular

gov.br Documento assinado digitalmente
MATHEUS ROLIM SALES
Data: 10/02/2025 10:37:13-0300
Verifique em https://validar.iti.gov.br

_____ _____

Dr. Matheus Rolim Sales – UNESP – Titular

Ponta Grossa, 10 de fevereiro de 2025.

To my mother, Marcia dos Santos – in memoriam.

ACKNOWLEDGEMENTS

I express my gratitude to my family, especially my mother, Marcia dos Santos, and my father, Laercio Chipicoski Gabrick, for their support during the academic journey. I extend my heartfelt thanks to my girlfriend, Ana Luiza Rodrigues de Moraes, and her family for their care.

I am profoundly grateful to my advisor, Prof. Dr. Antonio Marcos Batista, for his guidance during my academic journey. My sincere thanks go to Prof. Dr. Dr. h.c. mult. Jürgen Kurths for his invaluable supervision and the warm reception I received in Germany.

I also thank Prof. Dr. Iberê L. Caldas and Prof. Dr. Ervin K. Lenzi for their intensive collaboration and insightful contributions to my doctoral research. Special thanks to Prof. Dr. Ervin K. Lenzi and Dr. Fernando S. Borges for their support and feedback during my qualification exam. In addition, I thank Prof. Prof. Dr. Silvio L. T. de Souza for present the model that is the content of this thesis.

To all my collaborators, in particular those from the 105 Group Science, I deeply appreciate your shared knowledge and teamwork. I am also grateful to Dr. Eduardo L. Brugnago for the collaboration in the works present in this thesis.

I extend my gratitude to the members of the committee Prof. Dr. Ervin K. Lenzi, Prof. Dr. Haroldo V. Ribeiro, Prof. Dr. Antonio S. M. de Castro, Dr. Matheus Rolim, whose valuable feedback and suggestions have enriched my work.

I am thankful to Universidade Estadual de Ponta Grossa, Humboldt-Universität zu Berlin, and the Potsdam-Institut für Klimafolgenforschung for providing the institutional support necessary for my research.

Finally, I acknowledge the financial support from the Coordination of Superior Level Staff Improvement (CAPES), which made this research possible in Brazil and Germany, under grants 88887.650484/2021-00 and 88881.846051/2023-01, respectively.

" *Que há entre a vida e a morte? Uma curta ponte*".
Machado de Assis, Memórias Póstumas de Brás Cubas.

ABSTRACT

In this thesis, we investigate the dynamical aspects of a Susceptible–Exposed–Infected–Recovered–Susceptible (SEIRS) model with a time-dependent contact rate. Moreover, we explore how vaccination strategies can be used to control chaotic dynamics and reduce the number of infected individuals. First, we introduce fundamental concepts of nonlinear dynamics, such as local stability, bifurcation, chaos, and Lyapunov exponents. Following this, we present key ideas from mathematical epidemiology by describing the compartmental models: Susceptible–Infected (SI), Susceptible–Infected–Susceptible (SIS), Susceptible–Infected–Recovered (SIR), and Susceptible–Exposed–Infected–Recovered (SEIR). As a practical application, we show an extension of SEIR model incorporating two vaccination doses. The next chapter focuses on the dynamical behavior of the SEIRS model. We first obtain the equilibrium solutions, namely the disease-free and endemic states, and analyze their stability. Subsequently, we introduce a time-dependent contact rate and examine the effects of its frequency on Lyapunov exponents. Our findings reveal that certain frequencies lead to multistable solutions, where chaotic and periodic attractors coexist. Further, we fix the contact rate frequency to one year and investigate the influence of other model parameters in the dynamics. Through bifurcation diagrams, we observe that almost all parameters affect the dynamics, often resulting in bistable regimes where periodic and chaotic attractors coexist. Additionally, we find that the inverse of the latent period is crucial for epidemic forecasting, as it is associated with tipping points where solutions change from periodic to chaotic attractors, thus compromising the forecast horizon. The final part of the thesis incorporates a constant vaccination campaign into the model. We first derive the stationary solutions for the unforced model and then extend these solutions to include seasonal forcing. This approach allows us to establish a vaccination threshold for disease eradication, which we validate through numerical simulations and found its limitations. For parameter sets exhibiting bistable solutions, we explore the effects of the vaccination campaign and uncover that constant vaccination can either suppress bistability or sustain it, depending on specific values. By analyzing the impact of constant immunization programs on Lyapunov exponents, we identify complex structures in parameter planes, including shrimps. Overall, the results presented in this thesis illustrate the intricate dynamical behavior of seasonal infectious diseases governed by SEIRS models, highlighting both the challenges and opportunities in controlling such systems.

Keywords: SEIRS, Seasonal infectious disease, Chaos, Multistability, Vaccination.

RESUMO

Nesta tese, investigamos as propriedades dinâmicas de um modelo Suscetível–Exposto–Infectado–Recuperado–Suscetível (SEIRS) com uma taxa de contato dependente do tempo. Também, exploramos como estratégias vacinais podem ser usadas no controle da dinâmica caótica e na redução do número de infectados. Inicialmente, introduzimos conceitos fundamentais de dinâmica não linear, como estabilidade, bifurcação, caos e expoentes de Lyapunov. Em seguida, apresentamos conceitos da epidemiologia matemática através dos modelos compartimentais: Suscetível–Infectado (SI), Suscetível–Infectado–Suscetível (SIS), Suscetível–Infectado–Recuperado (SIR) e Suscetível–Exposto–Infectado–Recuperado (SEIR). Como um exemplo de aplicação, mostramos uma extensão do modelo SEIR, na qual duas doses de vacinação são incorporadas. O próximo capítulo se concentra no comportamento dinâmico do modelo SEIRS, para o qual obtemos as soluções de equilíbrio, isto é, os estados livres de doenças e endêmico. Ademais, analisamos as estabilidades dessas soluções. A seguir, introduzimos uma taxa de contato dependente do tempo e examinamos os efeitos da sua frequência nos expoentes de Lyapunov. Nossas descobertas revelam que certas frequências levam a soluções multiestáveis, onde atratores caóticos e periódicos coexistem. Após, fixamos a frequência da taxa de contato em um ano e investigamos a influência de outros parâmetros do modelo na dinâmica. Por meio de diagramas de bifurcação, observamos que quase todos os parâmetros afetam a dinâmica, geralmente resultando em regimes biestáveis onde atratores periódicos e caóticos coexistem. Através dessa análise, descobrimos que o inverso do período latente é crucial para a previsão de epidemias, pois está associado a pontos de inflexão onde as soluções mudam de atratores periódicos para caóticos, comprometendo assim o horizonte de previsão. A parte final da tese incorpora uma campanha de vacinação constante ao modelo. Primeiro, derivamos as soluções estacionárias para o modelo não forçado e, em seguida, estendemos essas soluções para incluir o forçamento sazonal. Essa abordagem nos permite estabelecer um limiar de vacinação para erradicação de doenças, que validamos por meio de simulações numéricas e encontramos suas limitações. Para conjuntos de parâmetros que exibem soluções biestáveis, exploramos os efeitos da campanha de vacinação e descobrimos que a vacinação constante pode suprimir a biestabilidade ou sustentá-la, dependendo de valores específicos. Ao analisar o impacto de programas de imunização constantes em expoentes de Lyapunov, identificamos estruturas complexas em planos de parâmetros, incluindo camarões. No geral, os resultados apresentados nesta tese ilustram o intrincado comportamento dinâmico de doenças infecciosas sazonais governadas por modelos SEIRS, destacando os desafios e as oportunidades no controle de tais sistemas.

Palavras-chave: SEIRS, Doenças infecciosas sazonais, Caos, Multiestabilidade, Vacinação.

SUMMARY

1 INTRODUCTION 10

2 FUNDAMENTAL CONCEPTS OF NONLINEAR DYNAMICS 13

2.1 ORDINARY DIFFERENTIAL EQUATIONS 13

2.1.1 Numerical solution 14

2.2 STABILITY 15

2.2.1 Stability Analysis 16

2.2.2 Hurwitz and Routh criteria 18

2.3 BIFURCATION 19

2.3.1 Transcritical bifurcation 20

2.3.2 Saddle-Node bifurcation 20

2.3.3 Period-doubling bifurcation 21

2.4 CHAOS 22

2.4.1 Lyapunov Exponents 23

2.4.2 Numerical determination of Lyapunov Exponents 24

3 EPIDEMIC MODELS 27

3.1 SI MODEL 28

3.2 SIS MODEL 32

3.3 SIR MODEL 36

3.4 SEIR MODEL 39

3.4.1 Application of SEIR 41

3.5 SUMMARY 45

4 MULTI-STABILITY, CHAOS, AND TIPPING POINT IN SEIRS 46

4.1 MODEL WITHOUT FORCING 46

4.1.1 DFE solution 47

4.1.2 Endemic solution 49
4.2 FORCED MODEL 50
4.3 INFLUENCE OF FREQUENCY INTO THE DYNAMICAL SYSTEM 52
4.4 MULTISTABILITY 56
4.5 BISTABILITY AND TIPPING POINT FOR SEASONAL FORCING 58
4.5.1 Bifurcation diagram for the inverse of latent period 60
4.5.2 Tipping point 63
4.6 SUMMARY 65

5 CONSTANT VACCINATION CAMPAIGN AND DYNAMICAL ASPECTS . . . 66
5.1 MODEL 66
5.1.1 DFE solution 67
5.1.2 Endemic solution 68
5.2 VACCINATION THRESHOLD 69
5.3 CONSTANT VACCINATION STRATEGY 70
5.4 DYNAMICAL BEHAVIOR FOR CONSTANT VACCINATION 75
5.5 SUMMARY 79

6 FINAL REMARKS 80

REFERENCES 81

1 INTRODUCTION

Throughout human history, many societies have been severely impacted by different diseases that affect the common well-being. These illnesses spread within communities, infecting a large number of individuals – humans, animals or plants. Depending on the number of infections and the geographical spread, they are classified as outbreaks, epidemics, or pandemics. An outbreak occurs when there are more cases of infections by one disease than expected for a defined community, season, or geographical area (1). Meanwhile, an epidemic refers to a sudden increase in the infected number of individuals for a given disease in a specific geographical area (2). Lastly, a pandemic is an epidemic that spreads across a large geographical region or even worldwide, typically affecting a huge number of individuals (3).

It is widely recognized that the spread of diseases causes significant socioeconomic damage. However, some illnesses have left a deeper mark on history than others. To mention a few examples, we refer to the Black Death in the mid-ages, which caused more than 25 million deaths in Europe (4), the Spanish flu (1918-1919), responsible for killing around 20 to 50 million people worldwide (5), and the COVID-19 pandemic (6), causing around 7 million deaths (7). Nevertheless, many other diseases affected and continue to affect life on Earth (8–10). Therefore, understanding how diseases spread through populations and how to mitigate their effects remains a critical scientific challenge.

Although there are various ways to study the aforementioned problem, one of the most powerful approaches is through mathematical models (11, 12). Using this approach, it is possible forecast disease spread (13) and simulate control methods (14, 15) for it. Different mathematical frameworks can be employed to understand the dynamics of disease spread, such as classical regression models (16), machine learning techniques (17), and others (18).

In general, the most successful epidemiological models are compartmental ones, typically governed by first-order Ordinary Differential Equations (ODEs) (11). They originated from the pioneering work of McKendrick and Kermack, published in 1927 (19), 1932 (20), and 1933 (21). In mathematical epidemiology, compartmental models are well-know for their simplicity and effectiveness in describing real data (22–24).

Since 1927, compartmental models have been used to describe a wide range of infectious diseases, including those that exhibit patterns of recurrent infections (25), particularly seasonal infectious diseases (26). The recurrence of such infections can be attributed to various factors, such as weather conditions (27) or school holidays (28), depending on the specific disease. Notable examples of seasonal infectious diseases include influenza (29), measles (30), and dengue fever (31).

Compartmental models with a constant contact rate are unable to simulate seasonal infectious diseases. To include the seasonal effects, it is necessary to introduce a nonlinear contact rate into the model (26). This additional term can drive the system toward chaotic solutions, as observed in real-world time series data (32). Chaos in epidemiological models is an importat research topic because it highlights the complexity of seasonal infectious diseases and reveals the challenges in forecasting them (33–38). The presence of chaos significantly reduces the predictability horizon, and therefore, an important problem is the development of methods to control chaotic dynamics and restore predictability.

In terms of control methods, one of the most effective is the vaccination campaigns (39–41). These strategies are widely studied in the sense of reducing the number of infected individuals and can be implemented via the immunization of healthy individuals (42), which can be administrated in pulsed (43), time-dependent (44), or others way (45–47). Despite, there are many studies about the effects of vaccination in mitigating epidemics, less is known about the impacts on chaotic dynamics.

This thesis primarily addresses two problems: the complex dynamics of seasonal infectious diseases and the impact of vaccination strategies. The main contributions of this work are as follows: (i) We show that a simple epidemiological model with seasonal forcing can generate highly complex dynamics, ranging from chaotic to multistable, where chaotic and periodic attractors coexist. (ii) The unpredictability of seasonal infectious diseases is related to tipping phenomena. (iii) Vaccination strategies can give rise to intricate dynamics, including complex structures such as shrimps, while specific immunization strategies can serve as a control method for bistable solutions.

This thesis is organized as follows: In Chapter 2, we discuss concepts of nonlinear dy-

namics, such as a briefy introduction to Ordinary Differential Equations, stability of stationary solutions, bifurcations, chaos, and Lyapunov exponents.

In Chapter 3, we introduce fundamental concepts of compartmental models, such as the basic reproduction number and epidemic size. We begin Chapter 2 by presenting the Susceptible–Infected (SI) model, for which we derive the analytical solution. Next, we extend the analysis to the Susceptible–Infected–Susceptible (SIS) model, where we calculate the basic reproduction number and provide an analytical solution. By incorporating a recovered compartment, we discuss the Susceptible–Infected–Recovered (SIR) model and define the epidemic size by examining its asymptotic solution. Following this, we explore the basic properties of the Susceptible–Exposed–Infected–Recovered (SEIR) model, demonstrating how it can be applied to model a scenario involving two doses of vaccination using a Cellular Automata (CA) approach.

In Chapter 4, we introduce the Susceptible–Infected–Exposed–Recovered–Susceptible (SEIRS) model with seasonal forcing. We obtain the equilibrium points and analyzing their stability. Then, we investigate the effects of seasonal frequency on the model dynamics, observing transitions from periodic to chaotic behavior, as well as the emergence of multistable solutions where different attractors coexist. Following this, we restringe the analysis into the bistable solutions of the model, where chaotic and periodic attractors coexist. By examining the inverse of the latent period as a control parameter, we demonstrate the existence of tipping phenomena.

The Chapter 5 focuses on exploring a constant vaccination strategy within the forced SEIRS model and examining the impacts of such an immunization program on the model dynamics. We demonstrate how the equilibrium points and their stability are affected when constant vaccination is implemented. Additionally, we derive an expression for the minimum vaccination coverage, which we verify numerically. We observe that, under constant vaccination, transitions from periodic to chaotic dynamics can occur due to crises or period-doubling bifurcations. For a given set of parameters, we also demonstrate the existence of shrimp-like structures.

Finally, we drawn our final remarks in Chapter 6.

2 FUNDAMENTAL CONCEPTS OF NONLINEAR DYNAMICS

This chapter presents fundamental concepts of nonlinear dynamics employed along the thesis. We begin by presenting ordinary differential equations (ODEs) in Section 2.1. After that, we discuss general notions of local stability (Section 2.2) and bifurcations (Section 2.3). Finally, we present the concept of chaos, attractors, basin of attraction, and Lyapunov exponents (Section 2.4).

2.1 ORDINARY DIFFERENTIAL EQUATIONS

A *system* is defined as a set of objects coupled by a specific interaction (48). An example of a system is the Earth and the Moon, where the interaction is governed by the gravitational force. To characterize this system, we consider two variables: position and velocity. The system is *dynamical* if one or both variables change over time. Thus, a dynamical system is a system whose variables evolve over time and it description can be done via differential equations (49). Along this work, we consider dynamical systems described by ODEs.

To introduce fundamental concepts of ODEs, consider a generic n-dimensional dynamical system, which is governed by the following set of ODEs:

$$\frac{dx_1}{dt} = f_1(x_1, x_2, ..., x_n, t), \tag{2.1}$$

$$\frac{dx_2}{dt} = f_2(x_1, x_2, ..., x_n, t), \tag{2.2}$$

$$\vdots \tag{2.3}$$

$$\frac{dx_n}{dt} = f_n(x_1, x_2, ..., x_n, t). \tag{2.4}$$

Note that for an n-dimensional system we have n differential equations. As we are dealing with n equations, it is convenient to use a vector notation, that compact the equations to

$$\frac{d\mathbf{x}}{dt} = \mathbf{f}(\mathbf{x}, t), \tag{2.5}$$

where $\mathbf{x} = (x_1, x_2, ..., x_n)$ is an n-dimensional vector, and $\mathbf{f}$ is a function relating $\mathbf{x}$ to its

derivative. In terms of notation, sometimes we use $d\mathbf{x}/dt$ as $\dot{\mathbf{x}}$ and $f'(x) = df(x)/dx$.

The system described by Eqs. (2.5) is called *autonomous* if $\mathbf{f}$ does not explicity depends on time, and *nonautonomous* if $\mathbf{f}$ explicity depend on time (50). The variables $\mathbf{x}$ are referred as *state variables*, while $\mathbf{f}$ represents the *vector field* (48).

The motion of the system corresponds to the time evolution of the n state variables, which can be represented in an n-dimensional coordinate system, with the n variables being the axes. This representation is named as the *phase space* (51). It is important to note that the dimension of the phase space is equal to the dimension of the system.

Given an initial condition ($\mathbf{f}(\mathbf{x},0) \equiv \mathbf{x}_0$) together with Eqs. (2.5), we define an initial value problem, where the solutions can be determined analytically or numerically, depending on the case. For such problems, there is only one solution – assuming the validity of the theorem of existence and uniqueness (49). In general words, this theorem states that, for a given initial value problem, there is a unique solution. Consequently, trajectories in the phase space do not intersect each other (51).

2.1.1 Numerical solution

Analytical solutions for an initial value problem are treatable in specific cases, typically when $\mathbf{f}$ is linear. However, real-world scenarios often involve nonlinear interactions, making analytical solutions extremely challenging, or even untreatable. To solve this issue, we employ numerical approximations. One particularly effective approach for numerical approximations is the 4th order Runge-Kutta method (49).

The method involve the weighted average of $\mathbf{f}(\mathbf{x},t)$ in different points in the range $t_n < t \leq t_{n+1}$. For Eqs. (2.5) with $\mathbf{x}_0$, the approximate solution using this method is given by

$$\mathbf{x}_{n+1} = \mathbf{x}_n + \frac{1}{6}(\mathbf{k}_1 + 2\mathbf{k}_2 + 2\mathbf{k}_3 + \mathbf{k}_4), \tag{2.6}$$

where

$$\mathbf{k}_1 = \mathbf{f}(\mathbf{x},t), \tag{2.7}$$

$$\mathbf{k}_2 = \mathbf{f}(\mathbf{x}+0.5*h*\mathbf{k}_1,t+0.5*h), \tag{2.8}$$

$$\mathbf{k}_3 = \mathbf{f}(\mathbf{x}+0.5*h*\mathbf{k}_2,t+0.5*h), \tag{2.9}$$

$$\mathbf{k}_4 = \mathbf{f}(\mathbf{x}+h*\mathbf{k}_3,t+h), \tag{2.10}$$

$$t = t+h, \tag{2.11}$$

with h beign the time step (49, 52). The global truncation error is proportional to h^4 (49). To obtain numerical solutions, we implement the 4th order Runge-Kutta method in C language, and the results are plotted in Gnuplot. We choose this method because of its simplicity and accuracy, in the the sense that a method similar to the Euler introduces numerical errors for our goals and a more robust method, for example with adaptative step is more than we need to achieve the objectives of the work. As a matter of curiosity, other methods can be consulted in the Ref. (49).

2.2 STABILITY

Let us suppose that Eqs. (2.5) describe the flight of an airplane. To model realistic motion, it is necessary to incorporate principles from fluid mechanics, atmospheric conditions, the airplane's velocity, and other relevant factors. This results in a nonlinear set of ODEs, whithout exact analytical solution, but in the perturbative regime, asymptotic solutions offer a good description. Despite that, by setting appropriate parameters and initial conditions, it is possible to compute a numerical trajectory for the flight, using the 4th order Runge-Kutta method, for example. However, this solution is limited; for instance, it does not gives the conditions under which the flight is stable. Thus, besides we have the numerical trajectory, a crucial question remains open: under what conditions is the flight safe/stable? In addition to the numerical approach, it is worth mentioning that in the perturbative regime, asymptotic solutions offer a good description.

Stability is a key concept used to describe the behavior of a solution. The *stability* of a

solution is determined by examining the behavior of solutions with initial conditions close to the stable solution (48). A stable state means that, given a perturbation into the state, it will return to its initial position after a certain time (56), namely asymptotically stable. In some cases, the stable state coincides with a stationary solution.

Stationary solutions ($\mathbf{x}^*$) are characterized by no variation over time of the trajectory, i.e., $\dot{\mathbf{x}} = 0$ (49). In other words, these solutions represent states where the flow vanishes: $\mathbf{f}(\mathbf{x}^*, t) = 0$ (51). This implies that any solution starting at $\mathbf{x}^*$ will remain there for all time, since $\dot{\mathbf{x}} = 0$. For an autonomous system, the stationary solution is also a fixed point. For example, in the case of a pendulum, the equilibrium position is both a fixed point and a stationary solution. However, if the pendulum is periodically forced (nonautonomous), the stationary solution varies with time and is not a fixed point.

In the Lyapunov sense, an equilibrium point is asymptotically stable when all trajectories $\mathbf{x}(t)$, with initial conditions in a hypersphere of radius η centered at $\mathbf{x}^*$, converge to $\mathbf{x}^*$ as $t \to \infty$ (48, 52). The equilibrium point is locally stable if η is finite; otherwise, it is globally stable. That means, when the radius is infinite and encompasses the whole phase space, the equilibrium point is global stable. In both cases, the equilibrium point is referred to as an *attractor*, and the open set of initial conditions that evolve toward this attractor is called the *basin of attraction* (48). Thus, given the point $\mathbf{x}^*$, its basin of attraction is the set of initial conditions $\mathbf{x}_0$ for which $\mathbf{x}(t) \to \mathbf{x}^*$ as $t \to \infty$ (50, 52).

On the other hand, the equilibrium point $\mathbf{x}^*$ is said to be *unstable* if it is not stable (50). In this case, the trajectories do not converge to $\mathbf{x}^*$. Note that our definition of stability and instability is based on the concept of distance, which is taken to be Euclidean.

2.2.1 Stability Analysis

To perform a stability analysis, consider a two-dimensional dynamical system described by the following equations:

$$\dot{x} = f(x,y), \tag{2.12}$$

$$\dot{y} = g(x,y), \tag{2.13}$$

where the fixed point is the pair (x^*, y^*), where $(f(x^*, y^*), g(x^*, y^*)) = (0, 0)$. Introducing a small disturbance from the fixed point, we define $(u, v) = (x - x^*, y - y^*)$. To determine whether the disturbance grows or decays, we need to derive a differential equation for u and v, which leads to $\dot{u} = \dot{x}$ and $\dot{v} = \dot{y}$. Using this, we write

$$\dot{u} = f(x,y) = f(x^* + u, y^* + v), \tag{2.14}$$

$$\dot{v} = g(x,y) = g(x^* + u, y^* + v), \tag{2.15}$$

and performing a Taylor expansion we get

$$\dot{u} \approx f(x^*, y^*) + u \left.\frac{\partial f}{\partial x}\right|_{(x^*, y^*)} + v \left.\frac{\partial f}{\partial y}\right|_{(x^*, y^*)}, \tag{2.16}$$

$$\dot{v} \approx g(x^*, y^*) + u \left.\frac{\partial g}{\partial x}\right|_{(x^*, y^*)} + v \left.\frac{\partial g}{\partial y}\right|_{(x^*, y^*)}, \tag{2.17}$$

where the high-order terms in u and v are neglected.

Then, the disturbance (u, v) evolves according to

$$\begin{pmatrix} \dot{u} \\ \dot{v} \end{pmatrix} = \begin{pmatrix} \frac{\partial f}{\partial x} & \frac{\partial f}{\partial y} \\ \frac{\partial g}{\partial x} & \frac{\partial g}{\partial y} \end{pmatrix} \begin{pmatrix} u \\ v \end{pmatrix}, \tag{2.18}$$

where the matrix

$$\mathbb{J}_{(x^*, y^*)} = \begin{pmatrix} \frac{\partial f}{\partial x} & \frac{\partial f}{\partial y} \\ \frac{\partial g}{\partial x} & \frac{\partial g}{\partial y} \end{pmatrix} \tag{2.19}$$

is the Jacobian matrix evaluate at (x^*, y^*). In this way, the system (Eq. (2.18)) is linearized about (x^*, y^*) (52).

Now, we write a general solution $\mathbf{x} = (\mathbf{u}, \mathbf{v})$ for the linearized equations (Eq. (2.18)), which is

$$\mathbf{x}(t) = c_1 e^{\Delta_1 t} \mathbf{w}_1 + c_2 e^{\Delta_2 t} \mathbf{w}_2, \tag{2.20}$$

where $c_{1,2}$ are constants determined by the initial condition, $\Delta_{1,2}$ are the eigenvalues of $\mathbb{J}$ with

associated eigenvectors $\mathbf{w}_{1,2}$ (56). Then, the stability of (x^*, y^*) is determined by the sign of real part of $\Delta_{1,2}$, resulting in three possibilities:

- Stable: If $\Delta_1 < 0$ and $\Delta_2 < 0$, the solution $\mathbf{x}(t)$ converges to $\mathbf{x}^*$ as $t \to \infty$.
- Unstable: If $\Delta_1 > 0$ and $\Delta_2 > 0$, the solution $\mathbf{x}(t)$ diverges to infinity as $t \to \infty$.
- Saddle: If $\Delta_1 < 0$ and $\Delta_2 > 0$, one solution converges to $\mathbf{x}^*$ as $t \to \infty$ and is said to be stable in the $\mathbf{w}_1$ direction, while it is unstable in the $\mathbf{w}_2$ direction.

Although we have discussed stability concepts for a two-dimensional system, these ideas can be extended to higher dimensional systems, e.g., a 3-dimensional system is discussed in Ref. (53), while a 9-dimensional system is analysed in (54).

2.2.2 Hurwitz and Routh criteria

As discussed, stability is determined by the sign of the real part of the eigenvalues (Δ_j) of the linearized system. Sometimes, calculating the eigenvalues explicitly is challenging, as it results in formulas with numerous terms that complicate the analysis of their signs. One way to determine the sign of the eigenvalues without explicit calculation is by using the Routh–Hurwitz criterion (48).

Suppose an n-dynamical system, where the characteristic polynomial of the linearized matrix $\mathbf{A}$ is

$$\Delta^n + a_1\Delta^{n-1} + a_2\Delta^{n-2} + \ldots + a_{n-1}\Delta + a_n = 0. \tag{2.21}$$

The Routh and Hurwitz criterion ensures that all the roots Δ_j of this polynomial have real negative part if the coeficients a_j are positive (48). This is a necessary but not sufficient condition. To ensure that $\Delta_j < 0$ we need additional conditions, which are obtained from the Hurwitz matrix.

The n-Hurwitz matrices for the Eq. (2.21) are defined as

$$\mathbf{H}_1 = \begin{pmatrix} a_1 \end{pmatrix}, \quad \mathbf{H}_2 = \begin{pmatrix} a_1 & 1 \\ a_3 & a_2 \end{pmatrix}, \quad \mathbf{H}_3 = \begin{pmatrix} a_1 & 1 & 0 \\ a_3 & a_2 & a_1 \\ a_5 & a_4 & a_3 \end{pmatrix}, \tag{2.22}$$

where

$$\mathbf{H}_n = \begin{pmatrix} a_1 & 1 & 0 & ... & 0 \\ a_3 & a_2 & a_1 & ... & 0 \\ a_5 & a_4 & a_3 & ... & 0 \\ \vdots & \vdots & \vdots & \vdots & \vdots \\ 0 & 0 & 0 & 0 & a_n \end{pmatrix}, \tag{2.23}$$

and $a_j = 0$ if $j < 0$. Then, $Re(\Delta_j) < 0$ if $a_j > 0$ and the determinants $|\mathbf{H}_j|$ are positive.

As a praticta1 example, consider $n = 3$. The characteristic polynomial is $\Delta^3 + a_1\Delta^2 + a_2\Delta + a_3 = 0$ with the associated Hurwitz matrices equal to

$$\mathbf{H}_1 = \begin{pmatrix} a_1 \end{pmatrix}, \quad \mathbf{H}_2 = \begin{pmatrix} a_1 & 1 \\ a_3 & a_2 \end{pmatrix}, \quad \mathbf{H}_3 = \begin{pmatrix} a_1 & 1 & 0 \\ a_3 & a_2 & a_1 \\ 0 & 0 & a_3 \end{pmatrix}, \tag{2.24}$$

and determinants $|\mathbf{H}_1| = a_1$, $|\mathbf{H}_2| = a_1a_2 - a_3$, $|\mathbf{H}_3| = a_1a_2a_3 - a_3^2$. The condition to ensure the stability requires that $a_1 > 0$, $a_2 > 0$, $a_3 > 0$, and $a_1a_2 > a_3$ (48).

2.3 BIFURCATION

In a broader sense, bifurcation refers to structural changes in the topological structure of the phase space of a given dynamical system (48, 52). One classical example is the change observed in the logistic map, which describe the dynamics of a certain population depending on the growth rate. In this map, for certain growth rate (control parameter), the population approaches a fixed point. As the control parameter increases, an oscillation between high and low population levels emerges, which characterizes a bifurcation (50). In this section, we present some examples of bifurcations that arise in the main topic of the thesis. For a more specialized discussion of bifurcations, we recommend the following books (48, 50, 52).

2.3.1 Transcritical bifurcation

For certain dynamical systems, fixed points can exist for all values of the control parameter (48). However, such fixed points may have one stability for a given range of the control parameters, and change it as the parameter is varied (52). The mechanism behind this change in stability is known as the transcritical bifurcation.

To explain the transcritical bifurcation, consider the following prototypical example

$$\frac{dx}{dt} = f(x) = x(\mu - x), \tag{2.25}$$

where μ is the control parameter. The fixed points are $x_1^* = 0$ and $x_2^* = \mu$, with the stability determined by the sign of $f'(x) = \mu - 2x$, computed at fixed points we get $f'(x_1^*) = \mu$, and $f'(x_2^*) = -\mu$. When $\mu < 0$, the point x_1^* is stable and x_2^* is unstable; on the other hand, when $\mu > 0$, x_1^* is unstable and x_2^* is stable. Therefore, x_1^* and x_2^* have opposite stability (48).

First, assume $\mu < 0$. In this case, x_1^* is stable and x_2^* unstable. Now, as we increase μ from negative values to positive, once the origin is crossed, x_1^* and x_2^* exchange the stability: now x_1^* becomes unstable and x_2^* stable (52). The critical point $\mu_c = 0$ is the point where the bifurcation occurs. Starting in the opposite direction, i.e., with $\mu > 0$, a similar exchange happens at the same μ_c, but the difference is that x_1^* ends up as stable and x_2^* as unstable.

2.3.2 Saddle-Node bifurcation

Saddle-node is a fundamental mechanism for the creation and annihilation of fixed points (52). To understand this, let us consider the following dynamical system:

$$\frac{dx}{dt} = f(x) = \mu - x^2, \tag{2.26}$$

where μ is the control parameter. The fixed points of the system are $x_{1,2}^* = \pm\sqrt{\mu}$. Similarly, the stability is investigated through the sign of $f'(x)$, which returns $f'(x_1^*) = -2\sqrt{\mu}$ and $f'(x_2^*) = 2\sqrt{\mu}$. For $\mu > 0$, the point x_1^* is stable, but x_2^* is unstable. However, for $\mu < 0$ there is no real fixed points.

Starting from $\mu > 0$, there are two fixed points with opposite stability; i.e., the flow is attracted in the x_1^* direction and repelled in the x_2^* direction. As the measure μ decreases, both fixed points approach each other, and the points coalesce into a half-stable point at $x^* = 0$ when $\mu = 0$. As μ becomes negative, the points vanish, and there are no fixed points left in the system; the pair $x_{1,2}^*$ is annihilated at the bifurcation point $(x^*, \mu_c) = (0,0)$ (48). The destruction of this pair occurs when they collide with each other, and the mechanism behind it is known as the saddle-node bifurcation. However, even after they are annihilated, they continue to influence the dynamics as a ghost – a bottleneck region that attracts the trajectories and delays them. Typically, the time spent in the bottleneck increases as $(\mu - \mu_c)^{-1/2}$ (52).

2.3.3 Period-doubling bifurcation

Another mechanism associated with the birth and death of fixed points is the period-doubling bifurcation (50). Let us consider an abstract case. Assume a given fixed point x^* that exists for a certain value of μ, in this case, we call it period 1. As the parameter μ increases and crosses μ_{c_1}, two new fixed points emerge, leading to a two-period orbit. As $\mu > \mu_{c_1}$, further bifurcations occur, doubling the period and creating a cascade of bifurcations. This kind of bifurcation is called period-doubling and is a route to chaos (50). One famous example to illustrate this bifurcation is the logistic map (55).

First, consider the logistic equation

$$\frac{dx}{dt} = \mu x(1-x), \tag{2.27}$$

where μ is a positive constant. The Eq. (2.27) can be replaced by the following map

$$f(x) \equiv x_{n+1} = \mu x_n(1-x_n), \tag{2.28}$$

which is a recurrence equation. The evolution of such equation is defined by the composition of x, i.e., given an initial point $f(x)$, the evolution is $f^2(x) = f(f(x))$, and so on (50). In other words, the evolution of this map is obtained by computing the new state based on the previous one.

To investigate the period-doubling bifurcation, we use a bifurcation diagram, which is a tool widely used to study the stability and the nonlinear dynamics of a given system. Broadly, a bifurcation diagram records a given variable against the control parameter. In our case, for each μ value, we record the last 100 values of x_{n+1}, for n sufficient large (here we use $n = 1500$). Given this, the result is displayed in Fig. 1(a). We use the range $\mu \in [1,4]$, because for $\mu < 1$ the fixed point is a null population, and for $\mu > 4$ the system diverges.

Considering $\mu \in [1,3]$ in Fig. 1(a), the final state is a fixed point, which is marked in the bifurcation diagram (only one branch). This state characterizes an orbit with period 1, e.g., for $\mu = 2$ the steady states is $x_{n+1} = 0.5$. Increasing μ, there is a bifurcation in $\mu = 3$, where the orbit duplicate the period to 2 (two branches). Now, the population oscilatte between two values. Fixing $\mu = 3.25$, the orbit oscillate between 0.49 and 0.81, as observed in the time series in Fig. 1(c). The 2-period orbit exist in the range $\mu \in (3, 3.44)$, after 3.44 another duplification of period occurs, as amplified in Fig. 1(b). As μ increase, other duplification occurs, leading the system to a cascade of bifurcation until reaches the chaotic dynamics, as showed in Fig. 1(b). One example of chaotic time series is displayed in Fig. 1(d), for $\mu = 2.7$. However, note that as μ is varied appear periodic windows, but new chaos appear again.

2.4 CHAOS

Chaos is the irregular motion of a deterministic dynamical systems, exhibiting the following properties: it is irregular, unpredictable in the long term, sensitive to initial conditions, and complex but ordered in the phase space (51). By irregular, we mean non-periodic motion; by unpredictable, we mean that small disturbances in the initial condition leads the system to long-term unpredictable states. Sensitivity to initial conditions means that given two nearby trajectories, starting very close to each other, will diverge exponentially as time advances. By complex, we mean that the attractors are strange but have a defined shape, having fractal dimension. For chaos to exist in time-continuous autonomous dynamical systems, nonlinearity and at least three dimensions are required (48).

Throughout this work, we adopt the following definition of chaos: "*Chaos is defined by a Lyapunov exponent greater than zero*" (50).

Figure 1 – Bifurcation diagram for the logistic map, in panel (a), and the magnification of the range $\mu \in [3.4, 4]$ in panel (b). The numbers inside each graph count the respective period. Figures (c) and (d) shows time series for $\mu = 3.25$ and $\mu = 3.7$, respectively.

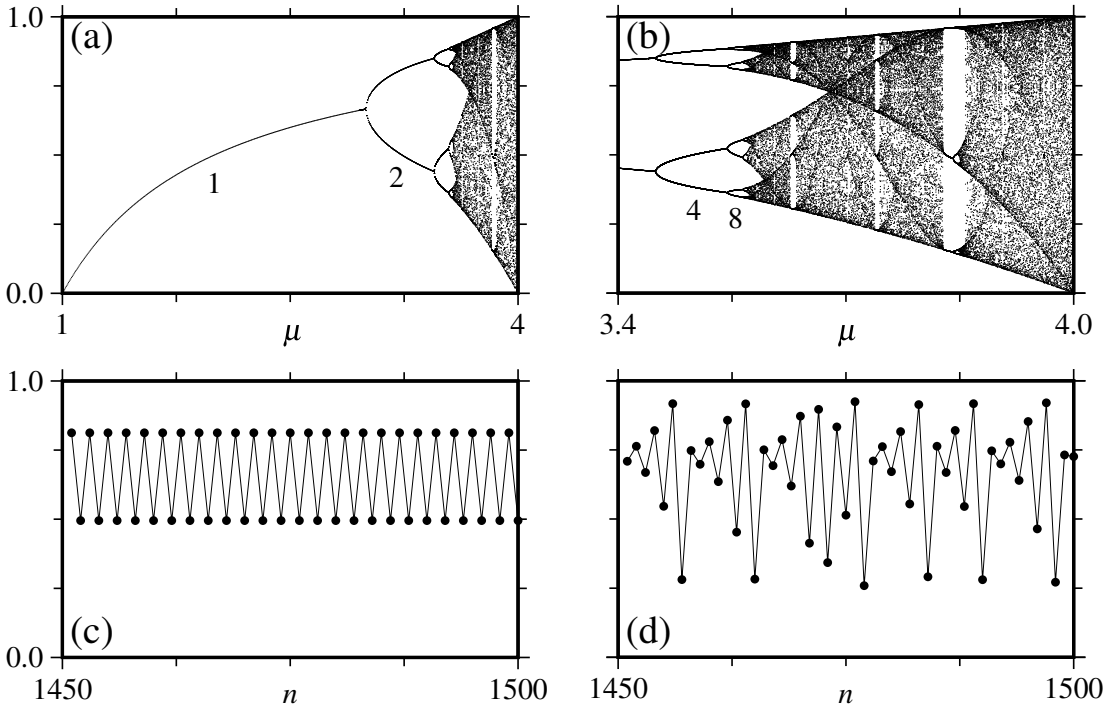

Source: The author.

2.4.1 Lyapunov Exponents

Before presenting the Lyapunov exponents, let us introduce a more formal definition of an attractor.

An attractor is a closed set $\mathscr{A}$ with the following properties (48):

- $\mathscr{A}$ is an invariant set: any trajectory $\mathbf{x}(t)$ in $\mathscr{A}$ remains in $\mathscr{A}$.
- $\mathscr{A}$ attracts an open set of initial conditions, denoted as $\mathscr{B}$. The open set $\mathscr{B}$ contains $\mathscr{A}$, for which given an initial condition $\mathbf{x}_0 \in \mathscr{B}$ the distance between the trajectory $\mathbf{x}(t)$ and $\mathscr{A}$ approaches to zero as t progresses. The open set $\mathscr{B}$ is called basin of attraction.
- $\mathscr{A}$ is minimal, i.e., there are not subsets of $\mathscr{A}$ that satisfy the first two conditions.

In addition, we define the transient as the time it takes for a trajectory $\mathbf{x}(t) \in \mathscr{B}$, where $\mathbf{x}(t) \notin \mathscr{A}$, to reach $\mathscr{A}$. Therefore, the transient is the time for $\mathbf{x}(t)$ to enter $\mathscr{A}$.

Now, we discuss the concept of Lyapunov exponents. As mentioned, a chaotic attractor exhibits sensitive dependence on initial conditions. This means that, given two trajectories

starting very close to each other, they separate exponentially as time progresses, leading to entirely different futures states. The practical implication of this is that long-term predictions become impossible (52). To understand this idea, assume a trajectory $\mathbf{x}(t) \in \mathscr{A}$. Then, $\mathbf{x}(t)$ is a point on the attractor, and we consider a nearby point $\mathbf{x}(t) + \varepsilon(t)$, where $\varepsilon \ll 1$ represents a small disturbance from the original state. As these trajectories diverges exponentially, the growth of ε follows the relation

$$|\varepsilon(t)| \approx |\varepsilon_0| e^{\lambda t}, \tag{2.29}$$

where the number λ is called the Lyapunov exponent. Note that if $\lambda > 0$, the trajectories separate exponentially fast; otherwise, they converge to each other exponentially fast (52).

The logarithmic plot of Eq. (2.29) against t produces a straight line with a positive slope for divergent trajectories. The slope of this line corresponds to the Lyapunov exponent. Additionally, this curve is not perfectly straight; it exhibits oscillations due to the varying strength of exponential divergence. Furthermore, the curve saturates when the divergence reaches the size of the attractor (52).

For an n-dimensional system, the Lyapunov exponents are defined as follows. Consider an infinitesimal sphere of initial conditions. As time progresses, the n-sphere is distorted into an n-ellipsoid due to the nature of the flow, with $\varepsilon_k(t)$ representing the length of the k-th principal axis of the ellipsoid, where $k = 1, 2, \ldots, n$. According to Eq. (2.29), there are λ_k exponents, where, for large t, the diameter of the ellipsoid is governed by the maximum exponent, λ, known as the largest Lyapunov exponent (51, 52).

2.4.2 Numerical determination of Lyapunov Exponents

Consider a flow given by $\dot{\mathbf{x}} = \mathbf{F}(\mathbf{x})$ and a trajectory $\mathbf{x}$, starting from the initial condition $\mathbf{x}(0)$. A second trajectory is obtained from a nearby initial condition, $\mathbf{x}'(0)$, resulting in the trajectory $\mathbf{y}(t)$. If $\mathbf{x}'(0)$ and $\mathbf{x}(0)$ are sufficiently close, we can write:

$$\mathbf{x}'(0) = \mathbf{x}(0) + \mathbf{w}(0), \tag{2.30}$$

where $|\mathbf{w}(0)| \ll |\mathbf{x}(0)|$, and the vector $\mathbf{w}$ is called tangent vector (56). Again, we consider the Euclidian distance.

For any time t, Eq. (2.30) is written as

$$\mathbf{x}'(t) = \mathbf{x}(t) + \mathbf{w}(t), \tag{2.31}$$

with $|\mathbf{w}(t)| \ll |\mathbf{x}(t)|$. The linearization of $\mathbf{F}$ about $\mathbf{x}(t)$ results in

$$\dot{\mathbf{x}}'(t) = \dot{\mathbf{x}}(t) + \dot{\mathbf{w}}(t) = \mathbf{F}(\mathbf{x}+\mathbf{w}), \tag{2.32}$$

$$\dot{\mathbf{x}}'(t) = \mathbf{F}(\mathbf{x}) + \mathbb{J}(\mathbf{x}) \cdot \mathbf{w} + ... \tag{2.33}$$

Rewritten Eq. (2.33) we obtain the time evolution of $\mathbf{w}(t)$, which is

$$\frac{d\mathbf{w}(t)}{dt} = \mathbb{J}(\mathbf{x}) \cdot \mathbf{w}. \tag{2.34}$$

Mostly part of the time, Eq. (2.34) admits only numerical solutions, especially in situations where the coefficients of the flow vary with time.

Analogous to maps (50), the unit vector $\mathbf{w}(t)/|\mathbf{w}(t)|$ gives the direction of the infinitesimal displacement of the trajectory from $\mathbf{x}$, while $\mathbf{w}(t)/|\mathbf{w}(0)|$ represents the factor of the displacement, showing whether it increases or decreases as time progresses. Therefore, the Lyapunov exponent for the trajectory defined from the initial condition $\mathbf{x}(0)$ in the orientation of the infinitesimal displacement given by the unit vector $\mathbf{u}(0) = \mathbf{w}(0)/|\mathbf{w}(0)|$ is given by:

$$\lambda(\mathbf{x}(0), \mathbf{u}(0)) = \lim_{t\to\infty} \frac{1}{t} \ln\left(\frac{|\mathbf{w}(t)|}{|\mathbf{w}(0)|}\right). \tag{2.35}$$

For an n-dimensional flow, there are n Lyapunov exponents, collectively called the Lyapunov spectrum (57). Notice that the Lyapunov exponents are related to the expansion or contraction of different directions in phase space (56, 57). Besides Eq. (2.35) defines the Lyapunov exponents, there are some technique issues in computing them directly from Eq. (2.35). The first is that for chaotic systems there is at least one exponential solution that diverges, leading to a storage problem in the computer memory. The second is that the vectors associated

with the separation evolve on time and tend to fall towards the local directions with fast growth. These problems can be solved by employing the Gram-Schmidt reorthonormalization (GSR) procedure (57). This method is often called the Wolf algorithm, due to the work in Ref. (57).

For an n-dimensional dynamical system, if one of the Lyapunov exponents is positive, we conclude that the system is chaotic (51). In a chaotic system, there exists a time horizon beyond which predictions break down, and this horizon is given by $t_{\text{horizon}} \propto 1/\lambda$ (52).

3 EPIDEMIC MODELS

Epidemiological compartmental models compartmentalize the host population according to the infectious status of the individuals (58). The models are based on mass action principle (59), from chemistry, and assume that the host population (with size N) is well homogeneously mixed (60). This theory establishes that several molecules well mixed within a container are subject to chemical reactions that transform molecules of one species into another, such that the rate of transformation is proportional to the initial concentration. Similarly, individuals in the host population can be thought as chemical species, in which contact processes transform individuals of one species into another. These statements are the basis to build the epidemiological models, however, before that we need to label these "species".

Firstly, we assume a given population and split the individuals between healthy and sick. This brings us to a model with two compartments: Susceptible (S) and Infected (I), where S holds the healthy individuals and I the infectious ones. The dynamical evolution occurs when S contact I and are transformed into I by a given rate, and stay there, such as $S \to I$. Models with this behavior are know as Susceptible–Infected (SI) model (61), and are appropriate to describe diseases like AIDS (62), where the healthy becomes permanently sick, once infected. On the other hand, some disease not confer permanent contamination, they infect the individuals and after a certain time the sick agent become healthy again, such that $S \to I \to S$. Then, a new class of compartmental models emerges, the so called Susceptible–Infected–Susceptible (SIS) model (63), which is adequate to model syphilis data (58).

On the other hand, certain illnesses contaminate the individuals and, after a certain time, they recover, acquiring immunity, or being removed from the population; to simulate this dynamics we use the Recovered (R) compartment. Thus, the dynamical process now is $S \to I \to R$, leading to the Susceptible–Infected–Recovered (SIR) model (64). The SIR class is one of the most useful in the epidemiological compartmental models, once they can model various diseases, e.g., measles (65) and others (11, 18). In this transformation, the final state is characterized by a permanent immunity. Nevertheless, this defense can be temporary, such that $S \to I \to R \to S$, yielding a Susceptible–Infected–Recovered–Susceptible (SIRS) model (66, 67).

Considering the models SI, SIS, SIR and SIRS we can describe a huge range of infectious diseases. Although, there are some diseases that infect the individuals and they not become infectious immediately, but spend a transient time to start spread the infection. In this way, a new compartment between S and I need to be insert, namely Exposed (E). The E compartment is responsible to keep the individuals in latent (68) and/or incubation period (69). The latent period is the time range in which the individuals do not transmit the disease (70), while in the incubation period the individuals can transmit the illness, with a lower probability than the infected individuals (69). With this new compartment the dynamics is represented by $S \to E \to I \to R$, and the model is labeled as Susceptible–Exposed–Infected–Recovered (SEIR) (71). Analogously, we also have $S \to E \to I \to R \to S$, called Susceptible–Exposed–Infected–Recovered–Susceptible (SEIRS) model (72), which are highly adequate to describe diseases such as COVID-19 (73).

Besides we mention the S, E, I, and R comparments, another notable characteristic of compartmental models is the ease to include new classes, such as hospitalization (74), asymptomatic cases (75), quarantine (76), among others (77, 78).

Given the previous background, in this chapter we introduct the SI (Section 3.1), SIS (Section 3.2), SIR (Section 3.3), and SEIR (Section 3.4) models.

3.1 SI MODEL

The SI model is one of the simplest compartmental models, from which is possible to understand an important parameter: the *transmission coefficient* (β) (79). This parameter appears in epidemic models and represents the rate at which S are transformed into I. To fully comprehend the meaning of this parameter, we derive the SI model in detail in this section.

Assuming a constant population (N) and homogeneously well-mixed, the transition $S \to I$ depends on individual behavior and the characteristics of the illness (2). The disease spreads through the population N as contacts occurs between S and I individuals. The nature of these contacts varies depending on the disease, but for simplicity, we will refer just as contacts. We assume that the rate of contact for each infected individual is constant. Since the population is homogeneous, the rate at which S individuals contacted per I agents is given by $S(t)/N$

multiplied by the rate of contact per infected individual at a given time. In other words, we can write

$$\frac{susceptible\ contacted}{infected\ individual \cdot time} = \frac{contacted\ individual}{infected\ individual \cdot time} \cdot \frac{S(t)}{N}. \tag{3.1}$$

Multiplying this relation by the probability of one S get the disease, we obtain the rate of new infected individuals per infected ones, which is

$$\frac{new\ infected}{infected\ individual \cdot time} = \frac{contacted\ individual}{infected\ individual \cdot time} \cdot \frac{S(t)}{N} \cdot transmission\ probability. \tag{3.2}$$

From this relation, we define

$$\beta \equiv \frac{contacted\ individual}{infected\ individual \cdot time} \cdot transmission\ probability. \tag{3.3}$$

This parameter represents the rate of new infections when all contacted individuals are susceptible, i.e., $S(t) = N$. This condition is typically satisfied at the beginning of an epidemic.

It is important to note that β is the product of two factors: the first is associated with the behavior of individuals, and the second is a characteristic of the disease. In this context, it is natural to consider $\beta \geq 0$, since $\beta < 0$ would not correspond to a physically meaningful quantity. When $\beta = 0$, there is no propagation in the system, and defining a transmission rate becomes irrelevant. Considering these points, we assume $\beta > 0$ throughout this work. Furthermore, observe that restriction methods, such as masking or social distance, decrease the contacts, implying a reduction of β.

Using Eqs. (3.2) and (3.3), the rate of new infected per time is written as

$$\frac{new\ infected}{time} = \beta \cdot \frac{S(t)}{N} \cdot I(t). \tag{3.4}$$

It is important to highlight that this is our first equation describing the dynamics of new infected individuals, i.e., Eq. (3.4) explicitly demonstrates how S are converted into new I. This relationship can be summarized using a flow diagram, as shown in Fig. 2.

At this point, we define how the S individuals become I. Assuming a constant population, the rate that we remove from S need to be insert in I, therefore, we get the following description

Figure 2 – Schematic representation of SI model.

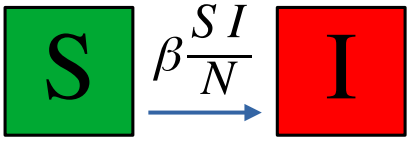

Source: The author.

of SI model:

$$\frac{dS}{dt} = -\beta \frac{SI}{N}, \tag{3.5}$$

$$\frac{dI}{dt} = \beta \frac{SI}{N}. \tag{3.6}$$

Equations (3.5) and (3.6) together with the initial conditions $S(0) = S_0$ and $I(0) = I_0$ define the SI model. Observe that $S+I$ is constant in time.

A constraint is obtained by summing Eqs. (3.5) and (3.6), resulting in $\dot{S} + \dot{I} = 0$, where the solution is $S + I = N$. This constraint allows us to rewrite Eqs. (3.5) and (3.6) in terms of fractions, making them independent of the total population size, through the transformations $s \to S/N$ and $i \to I/N$. In terms of the fractions s and i, the SI model becomes:

$$\frac{ds}{dt} = -\beta si, \tag{3.7}$$

$$\frac{di}{dt} = \beta si, \tag{3.8}$$

with initial conditions $s(0) = s_0$ and $i(0) = i_0$. In this work, italic capital letters denote the number of individuals, while lowercase letters represent fractions.

Despite the non-linearity in Eqs. (3.7) and (3.8), it is possible to derive an analytical solution for the SI model. The first step in obtaining this solution is to decouple Eqs. (3.7) and (3.8), by means of $s + i = 1$. Substituting $s = 1 - i$ into Eq. (3.8), we obtain:

$$\frac{di}{dt} = \beta(1-i)i, \tag{3.9}$$

which is an invariant space reduction due to the conserved quantity.

Equation (3.9) can be rewriten using partial fractions which returns an equation that is easily integrable. Skiping this step and considering $i(0) = i_0$, the solution of Eq. (3.9) is

$$i(t) = \frac{i_0 e^{\beta t}}{1 + i_0(e^{\beta t} - 1)}. \tag{3.10}$$

Therefore, the solution family for Eqs. (3.7) and (3.8) is completely determined by Eq. (3.10) and $s = 1 - i$. To be a consistent epidemiological solution, our functions need to be defined within the set $D = \{(s,i) \in [0,1]^2 \mid s + i = 1\}$, which is a consequence of the model.

The validation that the solution given by Eq. (3.10) remains inside D is as follows. As previously observed, $\beta > 0$. In this sense, $e^{\beta t}$ is always positive when $t \geq 0$. The only term that could be taken negative is i_0, which does not represent a physical solution. Under these conditions, $i(t) \geq 0$.

However, note that we need to preserve $s(t) + i(t) = 1$. For this, the condition $0 \leq i(t) \leq 1$ must be satisfied. The previous assumptions are not sufficient to ensure this inequality. To address this, we impose $i_0 \in [0,1]$, ensuring that $i(t) \in [0,1]$.

Other important features of Eq. (3.10) is the asymptotic states. Note that when $i(t) = 0$ we obtain one equilibrium point for our ODE system. This point is named as *disease-free equilibrium* (DFE) and is given by $(\widehat{s}, \widehat{i}\,) = (1,0)$. In SI model, the DFE occurs when $i_0 = 0$. On the other hand, starting the system with $i_0 > 0$ and taking the limit $\lim_{t\to\infty} i(t)$ we get another equilibrium point: $(s^*, i^*) = (0,1)$, namely *endemic*. From now on, we employ the notation $\widehat{x}$ to DFE and x^* to endemic. The DFE equlibrium is related to a system without disease, while the endemic the illness persist in the population.

The time evolution of SI model is displayed in Fig. 3, where the green line shows s variable, while the red one shows the i evolution. The curves are obtained for $i_0 = 0.05$, $\beta = 0.1$ and $s_0 = 1 - i_0$. This result shows that while one compartment is emptied the other is filled. In other words, while s decrese, i increase. For this parametric configuration, the curves intersect each other when $s(t) = i(t)$, which yields $i(t) = 0.5$. Note that the s compartment leaks individuals until the null value. When this occurs, all the population remains in i state.

Figure 3 – Time evolution of SI model. Parameters: $i_0 = 0.05$, $\beta = 0.1$ and $s_0 = 1 - i_0$.

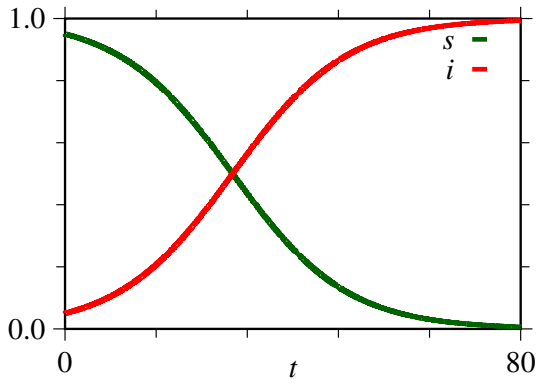

Source: The author.

3.2 SIS MODEL

The class of diseases described by the SI model assumes lifelong infection. However, some illnesses only confer infection for a limited period, after which the individual recovers and becomes healthy again (80, 81). Examples include gonorrhea (82), rotaviruses (83), and some bacterial infections (84). In this way, the SI model is not adequate to model such infections, and a modification is needed.

Assuming that individuals do not acquire immunity against the disease, the modification is straightforward: infected individuals remain in the I compartment for a certain period and, after that, return to the S compartment. This modification leads to the SIS model (85). A schematic representation of SIS is displayed in Fig. 4, where the I individuals are sending a rate γ to S compartment.

Figure 4 – Schematic representation of SIS model.

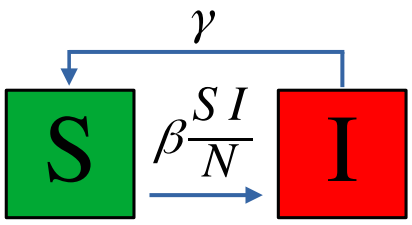

Source: The author.

The mathematical form of SIS model is:

$$\frac{ds}{dt} = -\beta si + \gamma i, \tag{3.11}$$
$$\frac{di}{dt} = \beta si - \gamma i, \tag{3.12}$$

where γ is a rate that transfers i to s, but not says to us the real meaning of this parameter. To interpret γ, let us discover the unit of this parameter.

Here, the time t is measured in time units (e.g., days), while S, I, and N are measured in individual units (s and i are fractions of individuals). To balance the equation, β and γ must have units of 1/time. Consequently, $1/\gamma$ represents a measure of time. Now we can interpret the meaning of $1/\gamma$.

Let us consider a simple situation in which $s(t) = 0$, i.e., all the population is infected. Thus, from Eq. (3.12) we get

$$\frac{di}{dt} = -\gamma i, \tag{3.13}$$

subject to the initial condition $i(0) = 1$. The solution for this initial value problem is $i(t) = e^{-\gamma t}$. Consequently, the rate in which $i(t)$ varies is $\dot{i} = -\gamma e^{-\gamma t}$. As this quantity decreases, the fraction of individuals in the infected compartment decrease as people heal, i.e., $-\dot{i} = \gamma e^{-\gamma t}$. Thus, the final state is characterized by population healing, which means

$$\int_0^\infty \left(-\frac{di}{dt}\right) dt = 1. \tag{3.14}$$

From this result is possibly interpret the quantity $-\dot{i} = \gamma e^{-\gamma t}$ as a probability distribution in $[0, \infty)$ (79). Knowing that all the people become healthy again, the average time to reach this point is given by

$$\int_0^\infty -t\frac{di}{dt}dt = \gamma \int_0^\infty te^{-\gamma t}dt, \tag{3.15}$$

this integral is solved by parts and the result is $1/\gamma$. Therefore, $1/\gamma$ is the average infectious period, i.e., γ is the recovery rate and, to have biological meaning, is a positive quantity.

Now that we understand the meaning of γ, let us focus on the discussion of the model given

by Eqs. (3.11) and (3.12). First, the fixed points of the SIS model are determined by solving

$$0 = -\beta si + \gamma i, \tag{3.16}$$

$$0 = \beta si - \gamma i. \tag{3.17}$$

A trivial solution is $s = i = 0$, and occurs when $s_0 = i_0 = 0$. The trivial solution is not interesting for us. Another solution is $s = \gamma/\beta$, from which it is possible to write the first equilibrium as $(s^*, i^*) = (\gamma/\beta, 1-\gamma/\beta)$, which has physical significance. This solution represents the endemic point. Differently from SI model, the final state is not necessary $i(t) = 1$, but $1-\gamma/\beta$. For this solution to be valid, we require $\gamma/\beta < 1$, or equivalently $\gamma < \beta$. This condition indicates that the infection rate exceeds the recovery rate, leading to an endemic state. However, if $\gamma > \beta$ the system is not driven to endemic state, but converges to DFE, which is $(\widehat{s}, \widehat{i}\,) = (1, 0)$. Thus, both equilibrium points exist for initial conditions greater than zero and their stability depends on values of γ and β.

To investigate the stability of these fixed points, we decoupled Eqs. (3.11) and (3.12) using $s + i = 1$, which yields to

$$\frac{di}{dt} = \beta i \left(1 - i - \frac{\gamma}{\beta}\right). \tag{3.18}$$

The shape of this curve is a parable with fixed points equal to $i = \widehat{i} = 0$ and $i = i^*$, which is graphically represented in a phase portrait (Fig. 5). Moreover, the derivative of Eq. (3.18) with respect to i is $f(i) = -2\beta i + \beta - \gamma$. Calculating $f(i)$ at the equilibrium points, we obtain $f(\widehat{i}\,) = \beta(1-\gamma/\beta)$ and $f(i^*) = -f(\widehat{i}\,)$. Observe that the points have opposite stability.

First, consider $\gamma/\beta < 1$, for which $f(\widehat{i}\,)$ is greater than zero and $f(i^*) < 0$. In this case, both equilibrium points exist, but $\widehat{i}$ is unstable (open circle in Fig. 5(a)), while i^* is stable (black closed circle in Fig. 5(a)). Solutions starting near $i = 0$ are repelled, and those close to $i = 1-\gamma/\beta$ are attracted, as indicated by the arrows in Fig. 5(a).

Now, consider $\gamma/\beta > 1$. In this case, $f(\widehat{i}\,) < 0$ and $f(i^*) > 0$. By changing the ratio γ/β, the stability of $\widehat{i}$ and i^* switches, as shown in Fig. 5(b). This exchange of stability is a transcritical bifurcation (52). Another way to visualize this bifurcation, is by ploting the stable and unstable lines, as exemplified in Fig. 5(c). In Fig. 5(c), the solid lines indicate stable equilibria and

the dotted lines indicate unstable ones, with red representing the fixed point $i = 0$ and blue representing $i = i^*$.

As observed, the ratio γ/β is very important. When $\gamma/\beta < 1$, the disease successfully invades the population, meanwhile if $\gamma/\beta > 1$ the disease fails to invade the population, and the steady state is DFE. For the SIS model, this ratio is the *basic reproductive number*, or R_0. This parameter is crucial in epidemiology as it indicates how many secondary infections one individual can cause. For the SIS model, R_0 is defined by

$$R_0 \equiv \frac{\beta}{\gamma}. \tag{3.19}$$

With this new quantity we summarize the information:

- If $R_0 < 1$ the disease fails to invade the population.
- If $R_0 > 1$ the disease successfully invades the population.

Figure 5 – Phase portrait for SIS model in panels (a) and (b). Panel (c) shows a transcritical bifurcation for SIS model.

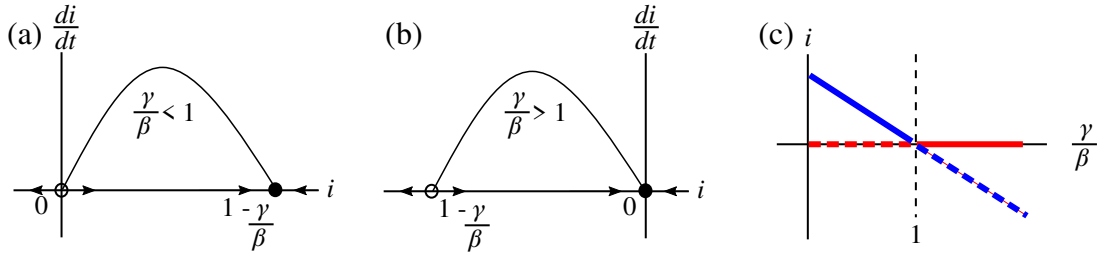

Source: The author.

Considering the basic reproduction number, Eq. (3.18) can be rewritten as

$$\frac{di}{dt} = i\beta[1 - i - R_0^{-1}], \tag{3.20}$$

with analytical solution equal to

$$i(t) = \frac{i_0(1 - R_0^{-1})e^{(1-R_0^{-1})\beta t}}{(1 - R_0^{-1}) + i_0(e^{(1-R_0^{-1})\beta t} - 1)}, \tag{3.21}$$

for $i(0) = i_0$. Here, $s(t)$ is immediately determined, once $s(t) = 1.0 - i(t)$. Considering the

limit $t \to \infty$, Eq. (3.21) results in $1 - R_0^{-1}$, which verify the equilibrium state (11), discussed previously.

Figure 6 display the time series for Eq. (3.21) considering $R_0 = 0.5$, in panel (a), and $R_0 = 2$, in panel (b), for different initial conditions. Observe from panel (a) that independent of the initial condition the solutions go to zero. From the result presented in panel (b), we observe that the solution goes to the steady solution defined by $i = 1 - R_0^{-1}$, represented by the horizontal dotted line.

Figure 6 – Solutions for SIS model with different initial conditions. In the panel (a) the parameters are $\beta = 0.25$, $\gamma = 0.5$ and $R_0 = 0.5$. In the panel (b) the parameters are $\beta = 0.5$, $\gamma = 0.25$ and $R_0 = 2$.

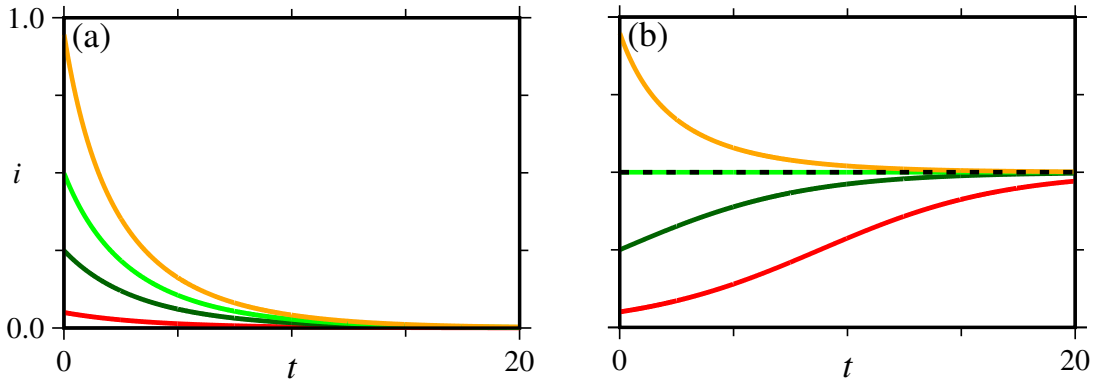

Source: The author.

3.3 SIR MODEL

Until now, we have studied models suitable for simulating the spread of diseases that do not confer immunity to individuals. To this dynamics we use the SIR model (18), represented in Fig. 7. Compared to previous models, the novelty here is the transition from I to R, which occurs at a rate γ. Note that γ is the same parameter introduced in Section 3.2. After the infectious period $(1/\gamma)$, individuals acquire lifelong immunity. An example of a disease described by the SIR model is measles (86).

To introduce the ODE formulation, we consider a closed population, i.e., without deaths, births, or migrations (demographic parameters). Additionally, we assume that the population is

Figure 7 – Schematic representation of SIR model.

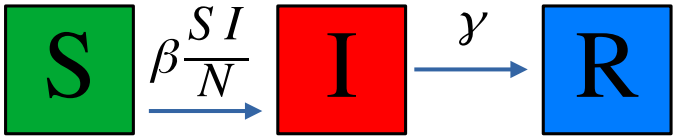

Source: The author.

homogeneously mixed. Under these conditions, the equations for the SIR model are

$$\frac{ds}{dt} = -\beta si, \tag{3.22}$$
$$\frac{di}{dt} = \beta si - \gamma i, \tag{3.23}$$
$$\frac{dr}{dt} = \gamma i, \tag{3.24}$$

where $s+i+r=1$ is preserved. Given the initial conditions $s(0)=s_0$, $i(0)=i_0$, $r(0)=r_0 \geq 0$, and parameters β and $\gamma \geq 0$, the solutions are in the set $D = \{(s,i,r) \in [0,1]^3 \mid s+i+r=1\}$ (87). Due to the non-linear term (si) and the new equation, analytical solutions of the SIR model are very challenging.

The first equilibrium solution is the trivial one, given by $(s,i,r)=(0,0,0)$. This solution does not exhibit any interesting properties. As previously discussed, another important fixed point is the DFE, obtained when $i(t)=0$. To find this point, we rewrite Eq. (3.23) as $\dot{i} = i\beta(s-\gamma/\beta)$. Note that there are two possible solutions: $i=0$ and $s=\gamma/\beta$. In the latter case, when $s > \gamma/\beta$, the fraction of infected individuals begins to increase. This feature is known as the threshold phenomenon and is related to R_0, which for the SIR model is defined as $R_0 = \beta/\gamma$. For the disease to successfully invade the host population, we require $R_0 > 1$, and additionally, the initial fraction of s must be greater than γ/β (11). Under these assumptions, the DFE is $(\widehat{s},\widehat{i},\widehat{r}) = (1,0,0)$. For the considered model, this is the only relevant equilibrium solution.

The asymptotic solution for SIR can be obtained by dividing Eq. (3.22) by Eq. (3.24), which gives

$$\frac{ds}{dr} = -\frac{\beta s}{\gamma} \equiv -R_0 s, \tag{3.25}$$

considering $r_0 = 0$, the solution is

$$s(t) = s_0 e^{R_0 r(t)}. \tag{3.26}$$

This result shows that the progression of an epidemic causes the number of susceptible individuals to decrease, while the number of recovered individuals increases with a delay proportional to $1/\gamma$. Note that s_0 and $e^{R_0 r(t)}$ are always positive, ensuring that $s(t)$ remains above zero. This finding leads to an important and counterintuitive conclusion: the spread eventually stops due to the decline in the number of infectious individuals, not because of the complete absence of susceptible individuals (11).

Assuming $s + i + r = 1$ and that the final of epidemic occurs in $i = 0$, when $t \to \infty$, the constraint reduces to $s = 1 - r$. Using the results in Eq. (3.26), we obtain

$$1 - r(t = \infty) - s_0 e^{R_0 r(t=\infty)} = 0. \tag{3.27}$$

Here, $r(\infty)$ represents the final fraction of recovered individuals, which is equal to the total fraction of individuals who contract the infection. The solution to this equation is obtained numerically, and the result is shown in Fig. 8. Situations where $R_0 < 1$ are highlighted with a green background, indicating no epidemic. For $R_0 > 1$, the infection successfully invades the population. The results show that for $R_0 = 2$, approximately 80% of the population contract the disease.

Figure 8 – Asymptotic solution $r(t = \infty)$ versus R_0.

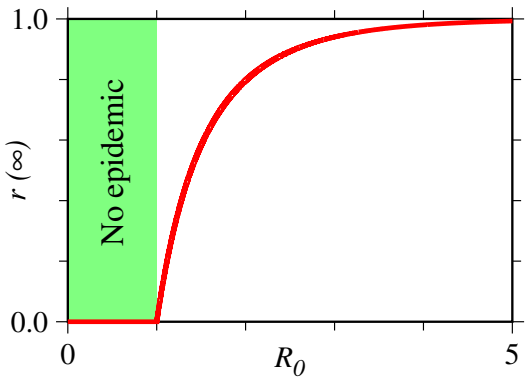

Source: The author.

Understood the basic properties of the SIR model, now we numerically integrate Eqs. (3.22),

(3.23), and (3.24) and present the results in Fig. 9. Panel (a) corresponds to $R_0 = 2$. As shown, when $R_0 = 2$, approximately 80% of the population becomes infected. This result is illustrated in Fig. 9(a) by the recovered curve (green line). Conversely, when $R_0 > 5$, nearly all individuals are infected, as observed in Fig. 8 and Fig. 9(b). From the numerical results, it is evident that one compartment decreases as another fills.

Figure 9 – Solutions for SIR model. In the panel (a) $R_0 = 2$ ($\beta = 0.5$ and $\gamma = 0.25$). In the panel (b) $R_0 = 5$ ($\beta = 0.5$ and $\gamma = 0.1$).

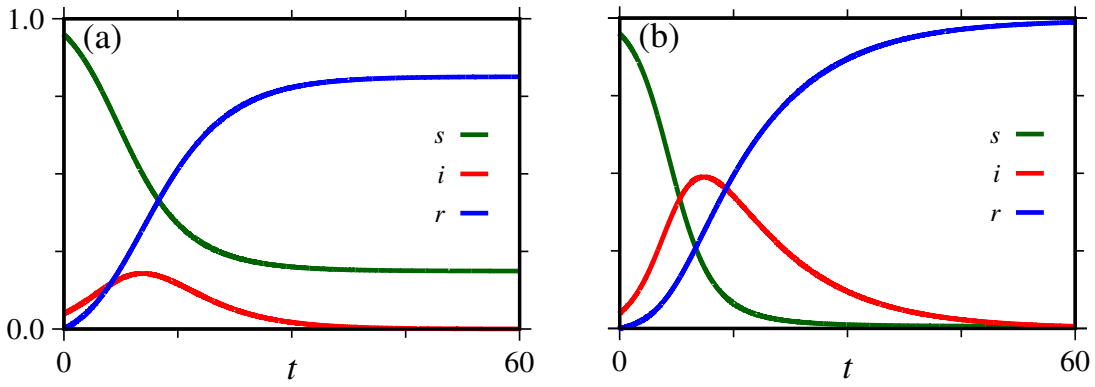

Source: The author.

3.4 SEIR MODEL

An extension of the SIR model is achieved by including a latent period ($1/\alpha$), through the Exposed (E) compartment. The representation of the SEIR model is shown in Fig. 10, where the host population is divided into four compartments (73). Here, the individuals in the E compartment are considered to be in the latent period (69, 88).

Figure 10 – Schematic representation of SEIR model.

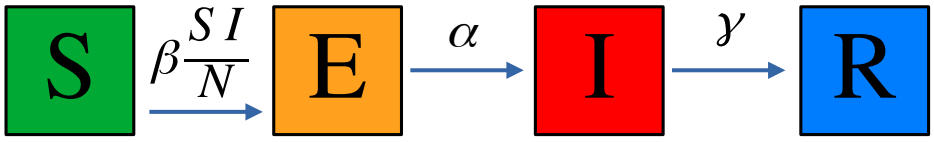

Source: The author.

The SEIR model is described by the following Eqs.

$$\frac{ds}{dt} = -\beta si, \tag{3.28}$$
$$\frac{de}{dt} = \beta si - \alpha e, \tag{3.29}$$
$$\frac{di}{dt} = \alpha e - \gamma i, \tag{3.30}$$
$$\frac{dr}{dt} = \gamma i, \tag{3.31}$$

note that $\dot{s} + \dot{e} + \dot{i} + \dot{r} = 0$. Therefore, as in the previous models, $s + e + i + r = 1$. With this constraint, Eq. (3.31) can be replaced by $r = 1 - s - e - i$. In the absence of demographic factors, $R_0 = \beta/\gamma$. For positive parameters and initial conditions, the solutions lie in the set $D = \{(s,e,i,r) \in [0,1]^4 \mid s + e + i + r = 1\}$.

The formulation given by Eqs. (3.28)-(3.31), without demographic terms, admits the equilibrium $(s,e,i) = (0,0,0)$ and $(\widehat{s},\widehat{e},\widehat{i}\,) = (1,0,0)$, with $r = 1 - s - e - i$. Since the susceptible population is not renewed, the steady state, for $i_0 > 0$ or $e_0 > 0$, is always reached when e and i approach zero, as observed in Fig. 11. The numerical solution (Fig. 11) shows $s(t)$, $e(t)$, $i(t)$, and $r(t)$ by the green, orange, red, and blue lines, respectively. Observe that the S compartment is leaky as the E compartment fills. However, after $1/\alpha$, individuals are transferred to I, which is reflected by an increase in the curve corresponding to these fractions. Once the infectious period ends, individuals transition to R and remain there.

Figure 11 – Solution for SEIR model. We consider $\alpha = 0.2$, $\beta = 0.5$, and $\gamma = 0.1$.

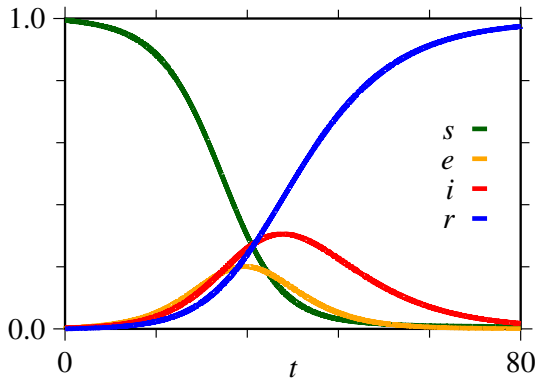

Source: The author.

3.4.1 Application of SEIR

One advantage of compartmental models is the easy way to adapt them by including new compartments. In this application, we show one extension made by us of the SEIR model, which include two vaccination doses (70). As a mathematical formulation, we consider stochastic cellular automata (CA) (89), that are simple structures that allow modeling each individual in a given population. The same mathematical framework also was applied in the SEIR model considering mobility in Ref. (72), where we study how individual's mobility affects the whole epidemic by exploring control strategies such as social restriction and relaxation.

CA models are considered discrete idealizations of partial differential equations (90, 91). This formulation is based on discrete time, space, and state variables. The time evolution of CA is governed by the previously defined local transition rules. These rules can be deterministic (92), stochastic (93), or mixed (94). A deterministic transition rule implies that a transition always occurs when the conditions are accepted. In a stochastic case, such transition occurs by a given probability. In the last case, both kinds of transitions are taken into consideration, i.e., the transitions for certain rules are probabilistic while others are purely deterministic. In this application, we build a two-dimensional CA mixing deterministic and probabilistic transition rules.

The model is in a lattice (L) structure composed of $\mathscr{N} \times \mathscr{N}$ identical cells (95), given by

$$L = (i, j), \;\; i, j \in Z_+^* \mid \; 1 \leq i, j \leq \mathscr{N}. \tag{3.32}$$

For each cell is attributed one state $x(i, j, t) \in \{1, 2, 3, 4\} = \{S, E, I, R\}$. Given a cell (i, j) on the grid, a neighbourhood V is defined by the set

$$V = \{(0,0), (-1,0), (-1,-1), (-1,1), (1,0), (1,-1), (1,1), (0,-1), (0,1)\}. \tag{3.33}$$

Then, the total neighborhood is given by $M(i, j) = (i, j) + v$, where $v \in V$. This neighborhood that considers the first 8 closest cells is called Moore. We consider null boundary conditions, i.e., the cells live in a plan. Defined this structure, we consider one time step when all cells in

the lattice are updated by the following transition rules, which defines SEIR standard model:

- Given an infected cell ($x(i,j,t) = 3$), it can infect a neighbour in the S state ($x(i,j,t) = 1$) by a probability β. If the cell is infected, then it evolves in the next step to E compartment ($x(i,j,t) = 2$).

- Given a cell in E state ($x(i,j,t) = 2$), the cells stay in this state by τ_1 time steps. In $\tau_1 + 1$, a fraction λ of these cells evolve to $x(i,j,t) = 3$.

- If $x(i,j,t) = 3$, then it remain in this state by τ_2 time steps. Thereafter, I individuals evolve to a recovered state ($x(i,j,t) = 4$) and stay there.

Until the moment this formulation gives a classical SEIR (Fig. 10). To include the new states $x(i,j,t) = 5$ and $x(i,j,t) = 6$, that model the first (V_1) and second (V_2) doses of vaccination, we include the new rules:

- Given a $x(i,j,t) = 5$ individual, if this cell has one or more I neighbors, it can be infected with $1 - \psi$ probability, where ψ is the first dose efficacy. If the infection is successful, the V_1 individual evolves to E. Otherwise, evolves to V_2 after τ_3.

- Once in V_2, the cells can be infected when in contact with I individuals by a probability $1 - \delta$, where δ is the booster efficacy. If the infection fails, the cells evolve to R after τ_4. Otherwise, it goes to E.

A flow diagram for the modified SEIR model is exhibited in Fig. 12, where the new compartments are represented by the dark blue squares, namely V_1 and V_2. In this diagram, a fraction f_v of S receives the first dose.

In the schematic representation in Fig. 12, a fraction f_v of S individuals receive the vaccine every time step until the S compartments leak. We named this strategy as (i) unlimited doses. This strategy is essential to understand the model properties, and can be considered as a large stock of vaccines for a small population. Furthermore, we propose two different strategies: (ii) limited doses into S population, and (iii) limited doses applied randomly overall to the host population. Therefore, strategy (ii) models a vaccine campaign where the population is tested

Figure 12 – Schematic representation for SEIR model with two vaccination doses.

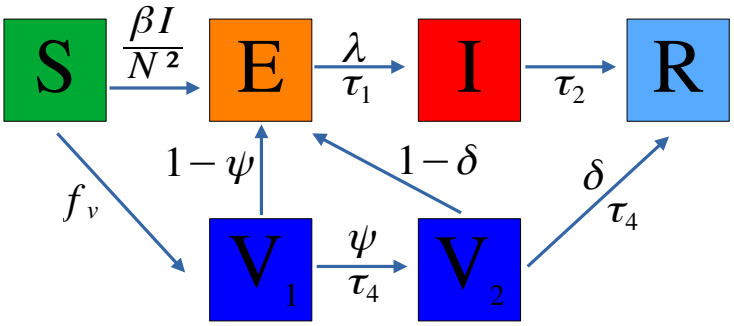

Source: The author.

before applying the vaccine; and (iii) the campaign vaccine randomly all the individuals, but we consider that the vaccine only works on S.

For (ii) and (iii) we predefined a certain amount of doses (D_{T}) for V_1 and V_2 states, representing the number of S that will receive the first and second doses. In this way, given a fixed number of doses, we apply this amount in the first group of S cells (strategy (ii)) or all individuals (strategy (iii)). After a time δt_{v}, another group receives the same amount of doses. This procedure is repeated until the S compartment becomes empty. In this way, these vaccination strategies can be conducted intermittently for $\delta t_{\mathrm{v}} > 1$, or continuously for $\delta t_{\mathrm{v}} = 1$. The evolution from V_1 to V_2 obeys the predefined rules. In the strategy (iii), the vaccine only works on S, then the doses applied in I, E, or R are wasted and the fraction of wasted doses (f_{w}) is measured. One essential finding of Ref (70) is to compare how much doses are wasted due to non-testing. Another characteristic of these strategies is that D_{T} can be split or not in any number of applications equally spaced. For example, given D_T doses this number can be applied one time ($N_{\mathrm{app}} = 1$) or several times ($N_{\mathrm{app}} > 1$) by small amounts given by $D_{\mathrm{T}}/N_{\mathrm{app}}$.

Figure 13(a) and (b) display the results for the strategy (i). In the panel (a), we display the time when the vaccination campaign starts (t_{v_1}) against f_{v}, where the color scale is the time to obtain DFE (T_0). These results show that the earlier the vaccination campaign starts and the larger the number of individuals that receive the vaccination, the earlier the epidemic is stopped. Panel (b) exhibits in the color scale the normalized area under the infected curve (A_{n}). The result presented in Fig. 13(b) corroborates the interpretation of Fig. 13(a).

Figure 14(a) and (b) display f_{w} as a function of N_{app}, where the circles are related to (ii)

Figure 13 – (a) Time to obtain DFE (T_0) and (b) normalized area under the infected curve (A_n) in color scale as function of t_{v_1} and f_v. We consider: $\mathcal{N} = 100$, $\lambda = 1/3$, $\beta = 1/4$, $\tau_1 = 6$, $\tau_2 = 14$, $\tau_4 = 10$, $\psi = 0.66$, and $\delta = 0.75$.

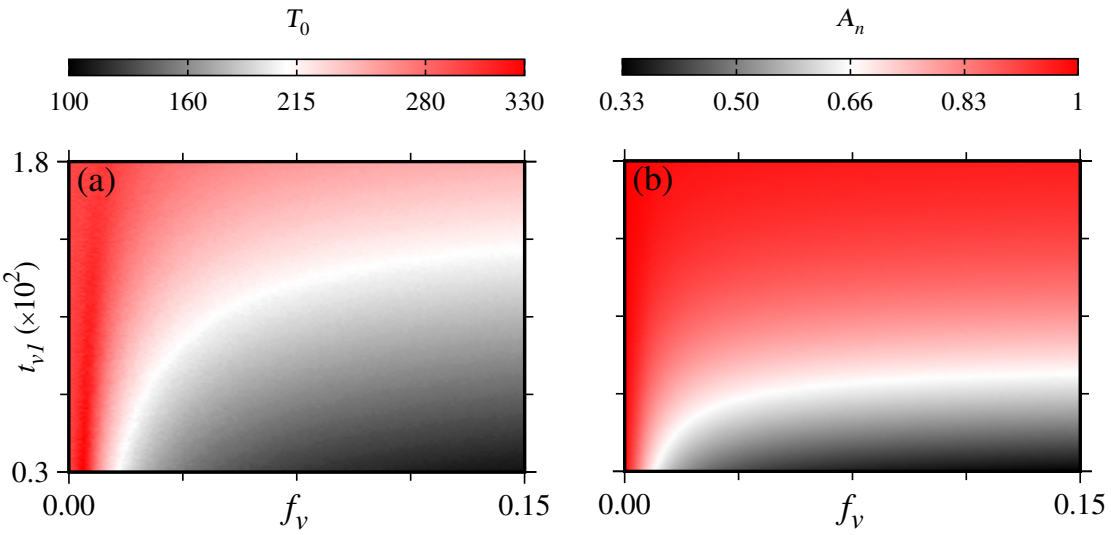

Source: The author.

and the squares to (iii). The green, black, and red objects are for $D_T = 3621$, $D_T = 4835$, and $D_T = 6073$, respectively. These numbers are the minimum D_T necessary to ensure DFE. The panel (a) is the wasted doses related to V_1 and panel (b) with V_2. These results show that for the strategy (ii) the number of wasted doses is always less than 0.2 independent of N_{app}. In some cases occurs wasted doses because the number of available S is less than D_T/N_{app}. On the other hand, the strategy (iii) present a linear increase of f_w as a function of N_{app}. This occurs since for many applications we need more time, and as time advances, more individuals get the infection and evolve to other compartments. The panel (b) also present a linear increase for (iii) while (ii) is practically constant. This occurs because the wasted of doses in V_2 is intrinsic to the model, i.e., given a certain amount of doses, some individuals in V_1 can be infected and the doses separated to evolve them to V_2 are wasted. Therefore, our model shows that is better to test the individuals before applying the vaccination, which is an important and practical result. Explained by the fact that without tests many doses are wasted, thus, reducing the number of vaccinated individuals and wasting resources.

Figure 14 – Fraction of wasted doses (f_w) relatives to first vaccine application (panel (a)) and second one (panel (b)). Circles are related to (ii) and squares with (iii). When the number of applications is greater than 1, the vaccine is applied every 7 days ($\delta t_v = 7$). We consider: $N = 100$, $\lambda = 1/3$, $\beta = 1/4$, $\tau_1 = 6$, $\tau_2 = 14$, $\tau_4 = 10$, $\psi = 0.66$, $\delta = 0.75$, $t_{v_1} = 60$, and $t_{v_2} = 84$.

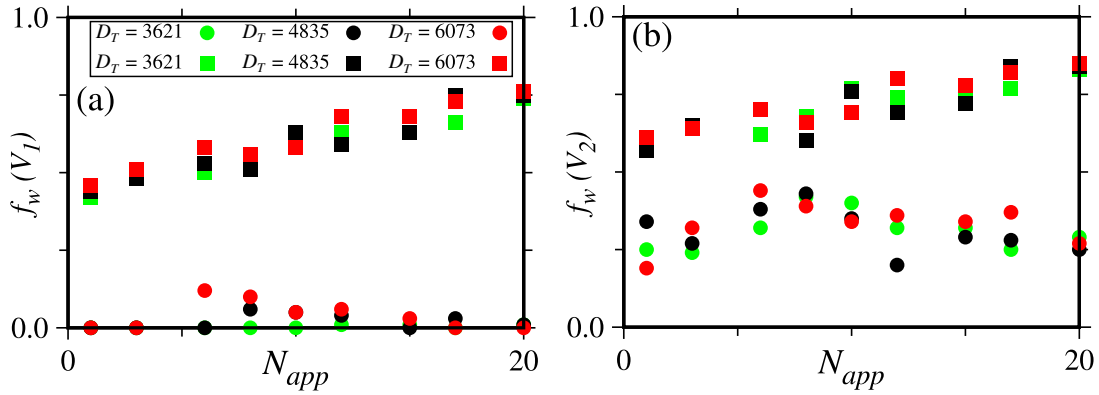

Source: The author.

3.5 SUMMARY

In this chapter, we revise some traditional epidemiological models, such as SI, SIS, SIR, and SEIR. We discussed important equilibrium points, namely endemic and DFE, and we obtain that parameter R_0. For the SEIR model, we showed one application that is an extension of this model to include vaccination doses. Therefore, the content of this chapter is essential to introduce the basic concepts of epidemiological compartment models.

4 MULTI-STABILITY, CHAOS, AND TIPPING POINT IN SEIRS

In this chapter, we study the dynamic behavior of the Susceptible–Exposed–Infected–Recovered–Susceptible (SEIRS) model with a time-dependent contact rate. The results were published in the Refs. (96, 97). Time-dependent contact rates are usually employed to describe the behavior of outbreaks that occur periodically (98). Several diseases present this seasonal pattern, such as influenza (99), pertusis (86), measles (100), chickenpox (32), and others. One important reference that contains many seasonal infectious diseases and the mechanism of seasonality is Ref. (25).

4.1 MODEL WITHOUT FORCING

Firstly, let us introduce the model and the basic properties in the absence of forcing. The considered model is described by

$$\frac{dS}{dt} = bN(t) - \mu S(t) - \beta \frac{S(t)I(t)}{N(t)} + \delta R(t), \tag{4.1}$$

$$\frac{dE}{dt} = \beta \frac{S(t)I(t)}{N(t)} - (\alpha + \mu)E(t), \tag{4.2}$$

$$\frac{dI}{dt} = \alpha E(t) - (\gamma + \mu)I(t), \tag{4.3}$$

$$\frac{dR}{dt} = \gamma I(t) - \mu R(t) - \delta R(t), \tag{4.4}$$

the new parameters $b \geq 0$ and $\mu \geq 0$ are the birth and natural death rates, respectively (101), and the population is not constant when $b \neq \mu$.

Summing Eqs. (4.1)-(4.4), we get

$$\dot{S} + \dot{E} + \dot{I} + \dot{R} = bN - \mu(S + E + I + R). \tag{4.5}$$

The total population is written as $S + E + I + R = N$, yielding

$$\dot{N} = N(b - \mu). \tag{4.6}$$

If $b > \mu$ the population increases, otherwise decreases. The solution of Eq. (4.6) is $N(t) = N_0 e^{(b-\mu)t}$, where N_0 is the initial population. For our simulations, we assume $b = \mu$, obtaining $N(t) = N_0$, where $N_0 \equiv N$. The assumption of $b = \mu$ is valid under certain conditions, i.e., a population that does not experience crises, such as wars or pandemics, isolated populations, i.e., that do not suffer from extreme migratory events, and is valid for certain time ranges. Under this condition, we are able to use the transformations $S = sN$, $E = eN$, $I = iN$, and $R = rN$ and rewrite Eqs. (4.1)-(4.4) in terms of fractions, i.e., independent of population size. Then, the normalized version become

$$\dot{s} = b - \mu s - \beta si + \delta(1 - s - e - i), \tag{4.7}$$

$$\dot{e} = \beta si - (\alpha + \mu)e, \tag{4.8}$$

$$\dot{i} = \alpha e - (\gamma + \mu)i, \tag{4.9}$$

where $\dot{r}$ is replaced by $r = 1 - s - e - i$.

Equations (4.7)-(4.9) define the normalized SEIRS model with demographic characteristics. It is possible to obtain three equilibrium points for these equations: (i) null population: $(s,e,i) = (0,0,0)$; (ii) DFE: $(s,e,i) = \left(\widehat{s},\widehat{e},\widehat{i}\right)$; and (iii) endemic $(s,e,i) = (s^*,e^*,i^*)$. Equilibrium (i) is trivial and does not give any interesting information, but (ii) and (iii) are important to the dynamic evolution. Then, we discuss both equilibriums separately.

4.1.1 DFE solution

DFE solutions are given when $e = i = 0$, under this condition Eqs. (4.7)-(4.9) reduces to

$$\dot{s} + s(\mu + \delta) = b + \delta. \tag{4.10}$$

The solution for Eq. (4.10) is analytical determined (49) and, for $s(0) = s_0$, is equal to

$$s(t) = 1 + (s_0 - 1)e^{-(\mu+\delta)t}, \tag{4.11}$$

where $b = \mu$. In the equilibrium, i.e., $\lim_{t\to\infty} s(t) = 1$. For intermediate values of time, the initial S population exponentially decay, and the end state is $s = 1$ because the individuals that goes to r return by a rate δ to S compartment. If we increase δ, the time to lose the immunity decreases, and the individuals return fast to s, i.e., the exponential decay is amplified in Eq. (4.11). Therefore, the DFE is $\left(\widehat{s},\widehat{e},\widehat{i}\right) = (1,0,0)$.

The local stability of the fixed point is investigated by the eigenvalues of the Jacobian matrix ($\mathbb{J}$) (49, 52), which for Eqs. (4.7)-(4.9) reads

$$\mathbb{J}_{(s,e,i)} = \begin{bmatrix} -\mu-\beta i-\delta & -\delta & -\beta s-\delta \\ \beta i & -(\alpha+\mu) & \beta s \\ 0 & \alpha & -(\gamma+\mu) \end{bmatrix}. \tag{4.12}$$

In the equilibrium point $\left(\widehat{s},\widehat{e},\widehat{i}\right)$, we obtain

$$\mathbb{J}_{\left(\widehat{s},\widehat{e},\widehat{i}\right)} = \begin{bmatrix} -\mu-\delta & -\delta & -\beta-\delta \\ 0 & -(\alpha+\mu) & \beta \\ 0 & \alpha & -(\gamma+\mu) \end{bmatrix}, \tag{4.13}$$

with associated eigenvalues (Δ) equal to

$$\Delta_1 = \frac{1}{2}\left(-\alpha-\gamma-2\mu-\sqrt{4\alpha\beta+(\alpha-\gamma)^2}\right), \tag{4.14}$$

$$\Delta_2 = \frac{1}{2}\left(-\alpha-\gamma-2\mu+\sqrt{4\alpha\beta+(\alpha-\gamma)^2}\right), \tag{4.15}$$

$$\Delta_3 = -\delta-\mu. \tag{4.16}$$

The stability of DFE is ensured when $\Delta_{1,2,3} < 0$. As the parameters are positive, the eigenvalues Δ_1 and Δ_3 satisfy this condition, but Δ_2 is less than zero when

$$\alpha+\gamma+2\mu > \sqrt{4\alpha\beta+(\alpha-\gamma)^2}. \tag{4.17}$$

The solution to this inequality is

$$1 > \frac{\alpha\beta}{(\alpha+\mu)(\gamma+\mu)}, \tag{4.18}$$

where the quantity on the right side is the R_0 for the SEIRS model . Therefore, if $R_0 < 1$ the DFE point is stable, otherwise is unstable.

In the presence of demographic characteristics the basic reproductive number for the SEIRS model is

$$R_0 = \frac{\alpha\beta}{(\alpha+\mu)(\gamma+\mu)}. \tag{4.19}$$

4.1.2 Endemic solution

The endemic solution of SEIRS model in terms of R_0 is

$$s^* = \frac{1}{R_0}, \tag{4.20}$$

$$e^* = \frac{(\alpha+\mu)[b+\mu-(\delta+\mu)R_0]}{\alpha\beta R_0+\alpha(\gamma+\delta+\mu)}, \tag{4.21}$$

$$i^* = \frac{\alpha[b+\delta-(\delta+\mu)R_0]}{(\gamma+\mu)(\delta+\mu)+\alpha(\gamma+\delta+\mu)}, \tag{4.22}$$

with Jacobian matrix equal to

$$\mathbb{J}_{(s^*,e^*,i^*)} = \begin{bmatrix} -\dfrac{\beta\alpha(b+\delta-R_0(\delta+\mu))}{\alpha(\gamma+\delta+\mu)+(\gamma+\mu)(\delta+\mu)} - \delta - \mu & -\delta & -\delta - \dfrac{\beta}{R_0} \\ \dfrac{\beta\alpha(b+\delta-R_0(\delta+\mu))}{\alpha(\gamma+\delta+\mu)+(\gamma+\mu)(\delta+\mu)} & -\alpha-\mu & \dfrac{\beta}{R_0} \\ 0 & \alpha & -\gamma-\mu \end{bmatrix}. \tag{4.23}$$

The analysis of the eingevalues from $\mathbb{J}_{(s^*,e^*,i^*)}$ becomes complex due to the presence of many parameters in the model. To solve this problem, we consider the characteristic polynomial of $\mathbb{J}_{(s^*,e^*,i^*)}$, which is given by

$$P(\Delta) = \Delta^3 + c_2\Delta^2 + c_1\Delta + c_0, \tag{4.24}$$

where

$$c_0 = \xi\left[\frac{\beta}{R_0} - (\alpha+\mu)(\gamma+\mu)\right] - \xi_1\left[\frac{\beta}{R_0}\alpha - (\gamma+\mu)\delta - \alpha\delta\right], \tag{4.25}$$

$$c_1 = \frac{\beta}{R_0} - (\alpha+\mu)(\gamma+\mu) - \xi(\alpha+\gamma+2\mu) - \delta\xi_1, \tag{4.26}$$

$$c_2 = -(\alpha-\gamma-\xi), \tag{4.27}$$

and

$$\xi = \delta+\mu+\frac{\beta\alpha(\alpha+\delta+\mu-R_0(\delta+\mu))}{\alpha(\gamma+\delta+\mu)+(\gamma+\mu)(\delta+\mu)}, \tag{4.28}$$

$$\xi_1 = \frac{\beta\alpha(\alpha+\delta+\mu-R_0(\delta+\mu))}{\alpha(\gamma+\delta+\mu)+(\gamma+\mu)(\delta+\mu)}. \tag{4.29}$$

In this way, the point (s^*, e^*, i^*) is stable if $\mathrm{Re}\{\Delta_{1,2,3}\} < 0$, where Re is the real part of Δ. Considering the coefficents $c_{0,1,3}$ and the Routh–Hurwitz criterion (48), we can find a condition for the fixed point be stable. The stability is ensure if and only if

$$c_0, c_1, c_2 > 0, \tag{4.30}$$

and

$$c_0 < c_1 c_2. \tag{4.31}$$

When these conditions are satisfied, endemic solution is stable. In our simulations, we observe that this point is asymptotically stable.

4.2 FORCED MODEL

The time-dependent formulation of the model described by Eqs. (4.7), (4.8), and (4.9) is obtained by introducing the transformation $\beta \to \beta(t)$. Based on the literature (101), we assume that $\beta(t)$ is governed by

$$\beta(t) = \beta_0(1+\beta_1\cos(\omega t)), \tag{4.32}$$

where β_0 represents the average contact rate, $\beta_1 \in [0,1]$ denotes the degree of seasonality, and ω is the frequency (102). Other forms of $\beta(t)$ are discussed in Ref. (103). The inclusion of a time-dependent contact rate transforms our model into a nonautonomous system, thereby the analysis of stability cannot be conducted as previously.

In the presence of the forcing, the basic reproduction number also changes and now is defined in the interval

$$R_0^- \leq R_0 \leq R_0^+, \tag{4.33}$$

where

$$R_0^\pm = \frac{\alpha\beta_0(1\pm\beta_1)}{(\alpha+b)(\gamma+b)}. \tag{4.34}$$

We define $R_0 > 1$ when $R_0^+ \geq R_0^- > 1$, and $R_0 < 1$ when $R_0^- \geq R_0^+ < 1$. These two bounds appear due to the maximum and minimum condition of Eq. (4.32). A condition for the convergence of DFE is obtained when $\langle R_0 \rangle < 1$, which is computed over a long-term evolution of the system (104).

As the system is now nonautonomous, we consider a transformation in Eq. (4.32) to change the system into an autonomous one. To do that, we consider $\omega t \equiv \tau$, such that $\tau \in [0, 2\pi)$, which gives us a new differential equation defined by $d\tau/dt = \omega$. Therefore, the complete system is described by

$$\dot{s} = b - \mu s - \beta_0(1+\beta_1\cos(\tau))si + \delta(1-s-e-i), \tag{4.35}$$

$$\dot{e} = \beta_0(1+\beta_1\cos(\tau))si - (\alpha+\mu)e, \tag{4.36}$$

$$\dot{i} = \alpha e - (\gamma+\mu)i, \tag{4.37}$$

$$\dot{\tau} = \omega. \tag{4.38}$$

A numerical solution for the SEIRS forced model is displayed in Fig. 15, where the time unit is years. The solution is obtained using the 4th-order Runge–Kutta integration method (49) with $h = 0.001$, as presented in Chapter 2. The green, orange, red, and blue curves in panel (a) show the time evolution of s, e, i, and r, respectively. A logarithmic scale for e and i is shown in panel (b). This solution illustrates the oscillatory dynamics of the system, with oscillations

occurring with a period of one year.

Figure 15 – Time evolution of SEIRS model with a time-dependent contact rate. (a) Solution for s, e, i, and r by green, orange, red, and blue curves, respectively. (b) Log scale of e and i. We consider: $\mu = 0.02$, $\omega = 2\pi$, $\alpha = 37.35$, $\gamma = 100$, $\delta = 0.25$, $\beta_1 = 0.15$, and $\beta_0 = 800$.

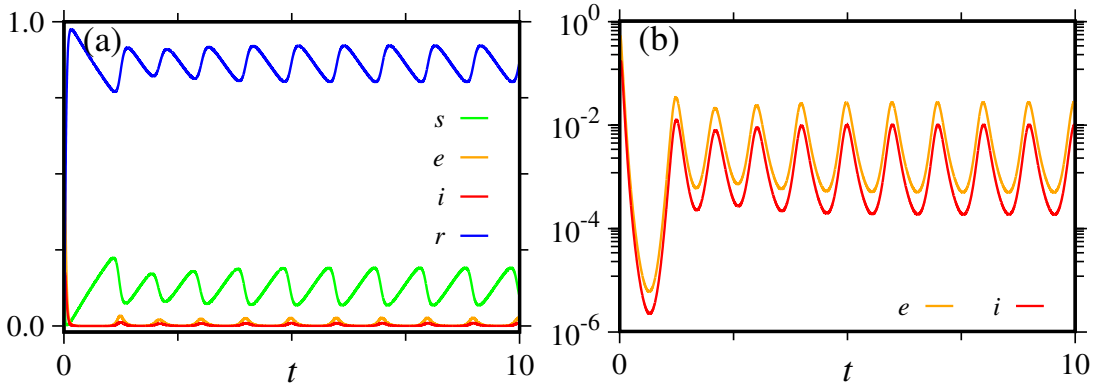

Source: The author.

The solution presented in Fig. 15 exhibits the periodic dynamics of the model. However, it is well known that the inclusion of a time-dependent rate in the SEIR and SEIRS models can also produce chaotic solutions for specific parameter sets (18, 101–103, 105). Most of the literature about chaos in seasonally forced models focuses on the influences of β_0 and β_1, while less is known about the effects of other parameters. In the next section, we investigate the impact of ω. It is worth mentioning that we study a wide range of parameters, but certain ranges are used in real diseases. To cite some examples, Measles $\alpha = 38.5$ and $\gamma = 100$, Chickenpox $\alpha = 24$ and $\gamma = 40$, Mumps $\alpha = 20$ and $\gamma = 31.18$, and Rubella $\alpha = 34.3$ and $\gamma = 31.7$ (101), with $\omega = 2\pi$, corresponding to a period of one year. The parameters β_0, β_1, b, and μ depends on each community, and the time unit is year.

4.3 INFLUENCE OF FREQUENCY INTO THE DYNAMICAL SYSTEM

We explore the effects of ω on the dynamics by computing the Lyapunov exponents (λ_j, where $j = 1,2,3,4$) for the parameter planes: $\alpha \times \omega$, $\gamma \times \omega$, $\beta_0 \times \omega$, and $\beta_1 \times \omega$. These results are part of the paper published in Ref. (97). The Lyapunov exponents are calculated using the Wolf algorithm (57), as discussed in Chapter 2. In all simulations, the integration step is set to 10^{-3}, the transient is 5×10^5 integration steps, and the solutions are computed over a time window of 10^6. The parameter planes are computed on uniform grids of 1000×1000. To

calculate the Lyapunov exponents, we use Eqs. (4.35)-(4.38).

In the results, when λ is greater than zero, we plot the largest one. Otherwise, we plot the second-largest exponent. This approach is adopted because the transformation from a non-autonomous to an autonomous system yields a null exponent. The initial conditions are $s_0 = 1 - e_0 - i_0$, $e_0 = 0$, and $i_0 = 0.001$.

Figure 16(a) illustrates the $\alpha \times \omega$ plane, where $\alpha \in (0, 400]$ and $\omega \in [0, 6\pi]$. The color scale represents λ. To compute this plane, we use the parameter values $\gamma = 100$, $b = 0.02$, $\delta = 0.25$, $\beta_0 = 270$, and $\beta_1 = 0.28$. Under this configuration, $0 < R_0 \leq 3.455$. The results shown in panel (a) reveal that the chaotic dynamics of the system are predominantly influenced by ω. However, for a fixed ω, some chaotic bands can also emerge by varying α. Forcing cycles with periods shorter than 6 months ($\omega < 4\pi$) exhibit predominantly periodic dynamics. Regardless of ω, a considerable part of the range $\alpha < 33$ exhibit periodic dynamics, corresponding to a latency period of 11 days. In this context, a disease with a latency period greater than 11 days exhibits periodic dynamics for the given parameters.

Fixing $\alpha = 100$ and varying γ in the range $[50, 250]$, we obtain the result shown in Fig. 16(b). For this configuration, we have $R_0 > 1$ for $\gamma < 194.4$, and for $194.4 < \gamma \leq 250$, we obtain $0.777 < R_0^- < 1$ and $R_0^+ > 1$. The structures formed by the pair $\gamma \times \omega$ are more complex when compared to the structures in panel (a). For γ, the chaotic structures are delimited in the parameter plane by a non-linear relationship between γ and ω. However, for $\omega > 3.5\pi$, a huge part of the parameter space shows periodic dynamics. For values of $\omega < 3.5\pi$, chaotic structures appear for $50 < \gamma \leq 250$. This range corresponds to infectious periods between approximately 7.3 and 1.46 days.

The results in Fig. 16(a) show a wide range of parameters and λ values, which persist in the next results. To provide an illustration of the time series for different values of the largest Lyapunov exponent (λ_1), we select two points in the $\alpha \times \omega$ plane with distinct λ_1 values. Our goal is to exemplify what happens with the time series when λ_1 is magnified by a factor of 11. To achieve this, we first evolve the solutions until they reach the attractor and, after that, plot the i time series over the last 50 years. The results are displayed in Figs. 17(a) and 17(b), where $\lambda_1 = 0.07$ for (a) and $\lambda_1 = 0.77$ for (b). In the first case, the parameters are $\alpha = 80$

Figure 16 – Parameter planes $\alpha \times \omega$ and $\gamma \times \omega$ in the panels (a) and (b), respectively. The color scale shows the Lyapunov exponents (λ). We consider $b = 0.02$, $\delta = 0.25$, $\beta_0 = 270$ and $\beta_1 = 0.28$. For (a) we use $\gamma = 100$ and for (b) $\alpha = 100$.

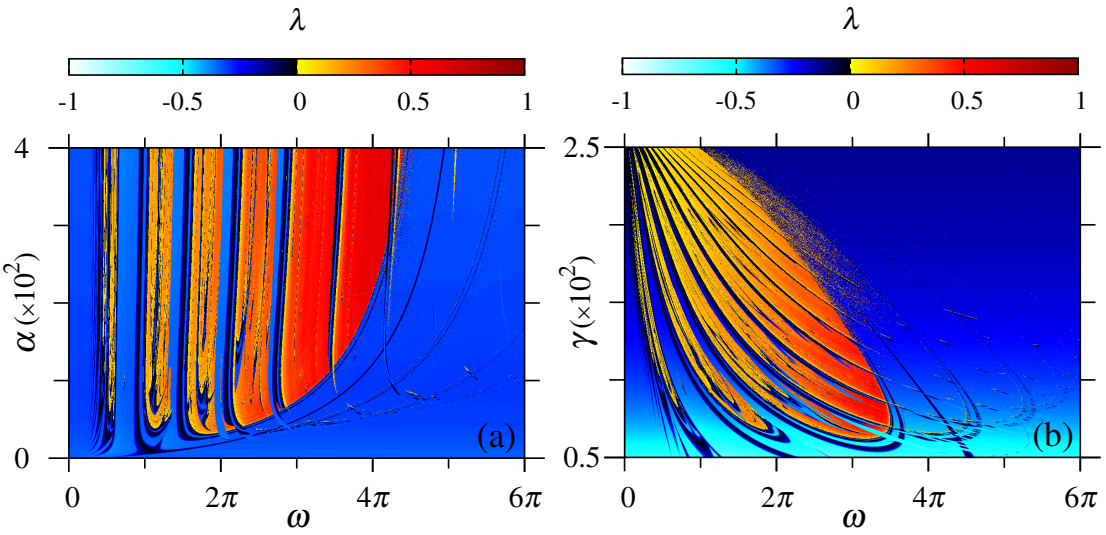

Source: Adapted from Ref. (97).

and $\omega = 3.20$, corresponding to a latent period of approximately 4.5 days and a forcing period of about 2 years. On the other hand, in Fig. 17(b), the parameters are $\alpha = 340$ and $\omega = 4\pi$, corresponding to a latent period of approximately 1 day and a forcing period of around half a year.

Comparing these curves, we observe that as λ_1 increases, the time series becomes more unpredictable. This is confirmed by the forecasting horizon, which is $t_{\text{horizon}} \propto 14$ years for $\lambda_1 = 0.07$ and $t_{\text{horizon}} \propto 1.3$ years for $\lambda_1 = 0.77$. This behavior is also reflected in the attractor, with the projection in the $i \times s$ plane shown in Figs. 17(c) and (d). The attractor displayed in Fig. 17(d) exhibits a more complex structure compared to the one present in Fig. 17(c). Therefore, for a time series with higher λ_1 values, the forecasting horizon is significantly reduced due to the increased complexity in the phase space. To the best of our knowledge, these parameters do not correspond to any real disease and are used only to illustrate differences in the dynamics.

As observed in the results presented in Fig. 16, the ω parameter exerts a significant influence on the dynamics of the SEIRS model. Figure 18 shows the parameter planes $\beta_0 \times \omega$ in panel (a) and $\beta_1 \times \omega$ in panel (b). These parameters are generated with $\alpha = \gamma = 100$, and the remaining parameters are the same as in Fig. 16. For panel (a), we fix $\beta_1 = 0.28$, and for panel (b), $\beta_0 = 270$. In panel (a), we use the range $\beta_0 \in [100, 600]$, because for $\beta_0 < 100$, only DFE solutions

Figure 17 – Time series for distinct largest Lyapunov exponents (λ_1) in panels (a) and (b), for $\lambda_1 = 0.07$ and $\lambda_1 = 0.77$, respectively. Attractor projection in the plane $i \times s$ in (c) and (d). We consider $b = 0.02$, $\delta = 0.25$, $\gamma = 100$, $\beta_0 = 270$, and $\beta_1 = 0.28$. For (a) and (c) we use $\alpha = 80$ and $\omega = 3.20$, while for (b) and (d) $\alpha = 340$ and $\omega = 4\pi$.

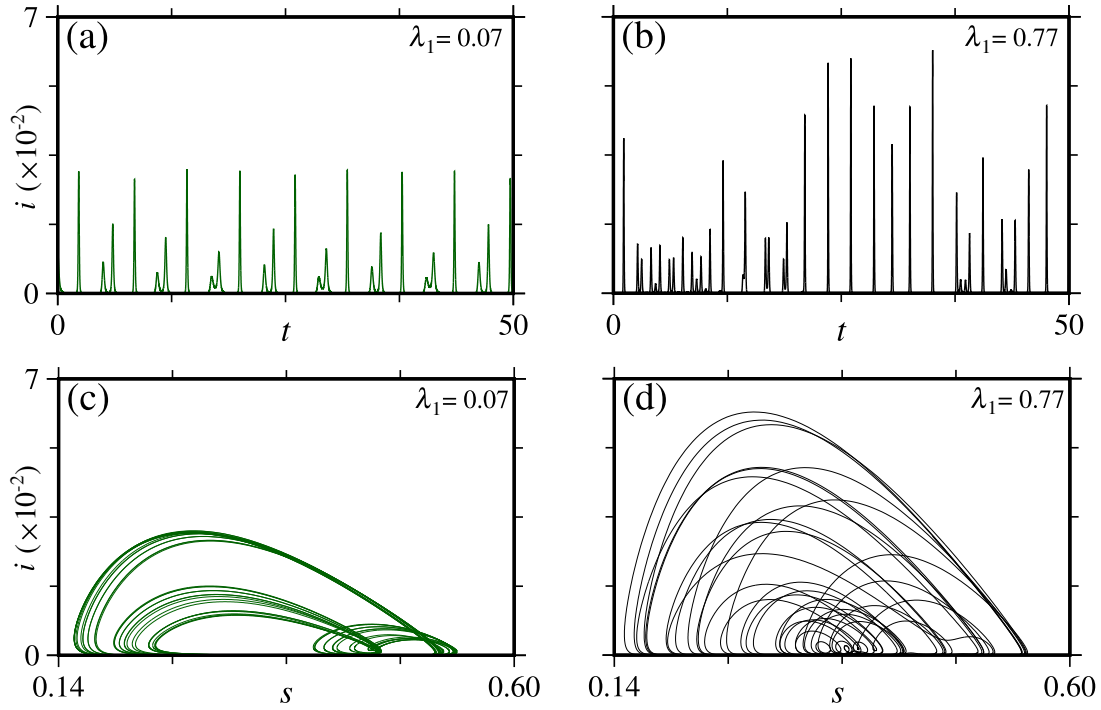

Source: The author.

exist, and for $\beta_0 > 600$, the solutions are periodic. In terms of R_0, we obtain $0.720 < R_0^- < 1$ and $R_0^+ > 1$ in the range $100 < \beta_0 < 138.944$. For $\beta_0 > 138.944$, our results suggest $R_0 > 1$. There is no clear relationship between β_0 and ω that establishes a limit for the chaotic structures. Thus, it shows that the pair $\beta_0 \times \omega$ is equally important in determining the dynamics.

Figure 18(b) displays the influence of β_1 on the dynamics. Chaotic solutions are possible for $\beta_1 > 0.14$ over a large range of ω. This result demonstrates that β_1 is a highly relevant parameter in determining whether the dynamics is chaotic or not. In these results, it is possible to observe that, for a given β_1, periodic and chaotic structures are created and destroyed. These bifurcations are mostly characterized by saddle-node points. In the range $0 < \beta_1 < 0.629$, R_0 is strictly greater than 1. For $0.629 < \beta_1 \leq 1$, the minimum and maximum values are $0 \leq R_0^- < 1$ and $R_0^+ > 1$.

Figure 18 – Parameter planes $\beta_0 \times \omega$ and $\beta_1 \times \omega$ in the panels (a) and (b), respectively. The color scale shows the Lyapunov exponents (λ). We consider $b = 0.02$, $\delta = 0.25$, $\gamma = 100$ and $\alpha = 100$. For (a) we use $\beta_1 = 0.28$ and for (b) $\beta_0 = 270$.

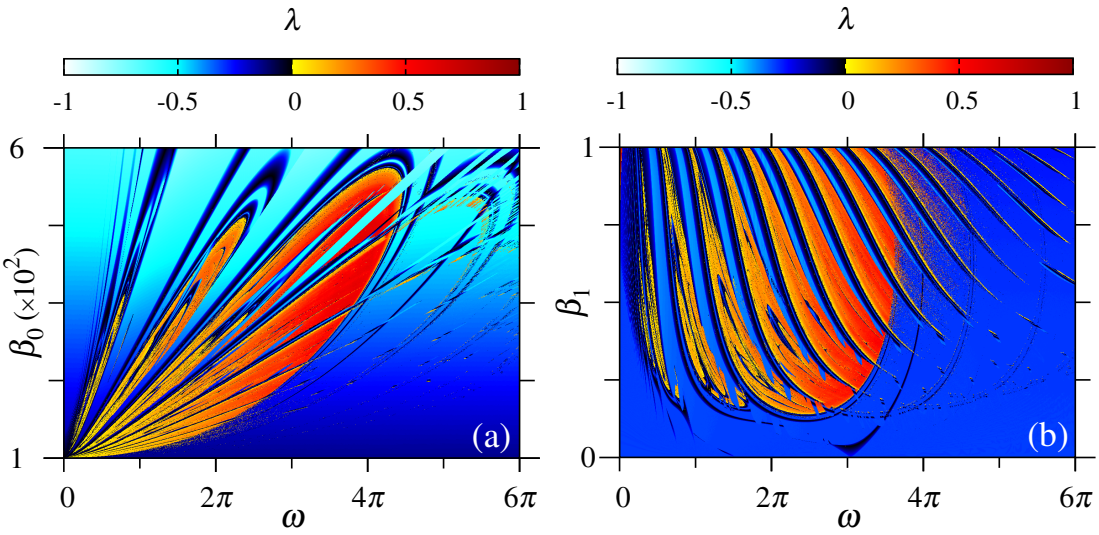

Source: Adapted from Ref. (97).

4.4 MULTISTABILITY

The parameter planes shown in Figs. 16 and 18 are calculated for a fixed initial condition. It is possible to observe that in some regions of the panels, the color pattern is abruptly disrupted. For example, in Fig. 18(b), along the line $\beta_1 = 0.2$, this phenomenon can be visualized. This occurs due to the presence of bi or multistability in the system. The presence of multistability is crucial in dynamical systems, as a small perturbation in the initial condition can drive the system to a different attractor with distinct characteristics (106–108).

Setting the parameters to $b = 0.02$, $\delta = 0.25$, $\gamma = 100$, $\alpha = 100$, $\beta_0 = 270$, and $\beta_1 = 0.2$, we search for multistable solutions by varying ω. For this parameter configuration, for each ω value, we generate 100 trajectories from randomly chosen initial conditions bounded by $0 < e_0, i_0 < 1$, and $s_0 = 1 - e_0 - i_0$. The randomly chosen initial conditions are uniformly distributed and always satisfy $e_0 + i_0 \leq 1$. We evolve the system for 10^6 integration steps and collect the local maxima of i, denoted by i_{p} (peak value), over the last 7.5×10^4 steps. Additionally, we compute the global maximum point in the i time series, denoted by $i_{\max}$.

Figure 19 displays the bifurcation diagram for the 100 random initial conditions, where the y-axis shows i_{p}, the x-axis displays ω, and the color scale represents $i_{\max}$. For a given

parameter configuration, it is possible to distinguish different orbits based on $i_{\max}$. In this way, we observe the existence of many attractors, which can be either periodic or chaotic. A large band of chaotic attractors coexists, starting from $\omega \approx 2.5\pi$ until $\omega \approx 3\pi$, where the value of $i_{\max}$ changes according to the initial condition. For higher frequencies, e.g., $\omega = 4.25\pi$, many periodic attractors coexist.

Figure 19 – Bifurcation diagram showing i_{p} versus ω and $i_{\max}$ in color scale. We use $b = 0.02$, $\delta = 0.25$, $\gamma = 100$ $\alpha = 100$, $\beta_0 = 270$, and $\beta_1 = 0.2$. The bifurcation diagram is generated from 100 randomly initial conditions.

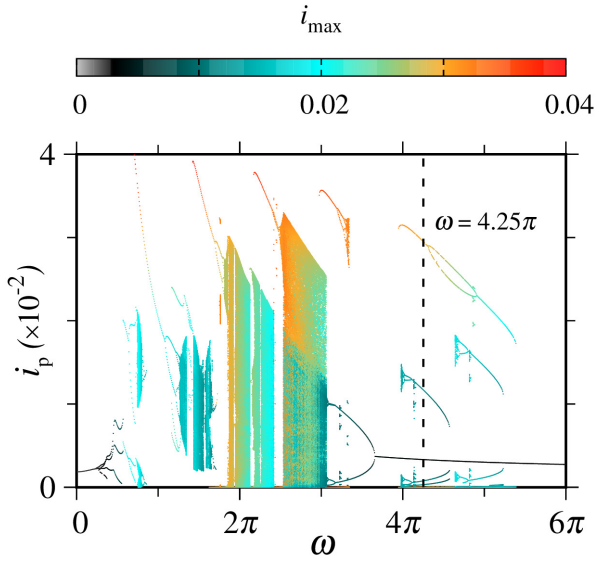

Source: Adapted from Ref. (97).

Considering $\omega = 4.25\pi$ (vertical dotted line in Fig. 19), we observe the existence of three distinct periodic attractors:

- period 1, with $i_{\max} \approx 0.003$ (black color);
- period 2, with $i_{\max} \approx 0.030$ (orange color); and
- period 3, with $i_{\max} \approx 0.012$ (teal color).

Based on these attractors, we compute the basin of attraction for this parameter configuration. To decide for each attractor the different trajectories evolve, we discard the transient and build a range in i, such that $i_{\max} \in (i_{\max} - \varepsilon, i_{\max} + \varepsilon)$, where $\varepsilon = 10^{-5}$. For example, the trajectories that evolve to the attractor of period 1 are in the set $i_{\max} \in (0.003 - \varepsilon, 0.003 + \varepsilon)$. The basin is displayed in Fig. 20, where the color code follows the colors of the attractors. The gray region

represents a prohibited regime where $e_0 + i_0 > 1$. This basin exhibits an interesting pattern of the three colors emerges as line segments in the plane $e_0 \times i_0$, revealing the complex dynamics of our system.

Figure 20 – Basin of attraction for $\omega = 4.25\pi$, where the color code displays three distinct periodic attractors. Black color: period 1 and $i_{\max} \approx 0.003$; Teal color: period 3 and $i_{\max} \approx 0.012$; Orange color: period 2 and $i_{\max} \approx 0.030$. We use $b = 0.02$, $\delta = 0.25$, $\gamma = 100$ $\alpha = 100$, $\beta_0 = 270$, and $\beta_1 = 0.2$.

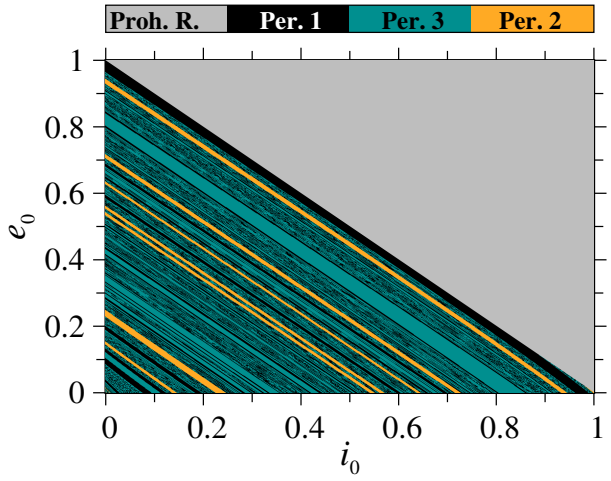

Source: Adapted from Ref. (97).

4.5 BISTABILITY AND TIPPING POINT FOR SEASONAL FORCING

Having observed the multistable solutions in the previous section, we now focus on bistable ones by computing bifurcation diagrams type hysteresis (109). This kind of diagram is composed of two bifurcation diagrams: one that follows the attractor in the positive direction of the control parameter (forward direction) and another that follows it in the negative direction (backward direction). If the system does not exhibit bistability, the diagrams overlap. For simplicity, we refer to hysteresis-type bifurcation diagrams as HTBDs. To compute the HTBD, we considered the maxima of the infected time series ($i_{\rm p}$) as well as the stroboscopic section of i, denoted by $i_{\rm s}$. We adopt these two approaches because, in epidemics, we are typically interested in the maxima of i, while in driven dynamical systems, the focus is on the stroboscopic section (51). The stroboscopic section is constructed by taking snapshots of the system at integer multiples of the driving period.

Using β_0 and δ as control parameters, the HTBDs for these parameters are displayed in Fig. 21, in logarithmic scale. Panels (a) and (b) correspond to β_0, while (c) and (d) correspond to δ.

Figures (a) and (c) display i_{p}, whereas (b) and (d) show i_{s}. The red points are recorded in the forward direction, and the blue ones in the backward direction of each parameter.

The results presented in Figs. 21(a) and (b) show the existence of two bistable ranges, highlighted by the gray background, in the intervals $\beta_0 \in [287, 332]$ and $\beta_0 \in [480, 491]$. In panel (a), the first bistable solution exhibits the coexistence of a chaotic and a 2-periodic attractor, while the second range demonstrates the coexistence of two periodic attractors. When considering the stroboscopic section in panel (b), the bistable range is located within the same interval, but the periods of the attractors differ. For instance, in the first bistable limit, the periodic attractor has period 3, while in the second range, both attractors have period 2. However, these bifurcation diagrams show transitions from periodic to chaotic orbits via period-doubling bifurcations and crises at certain critical values of β_0. Additionally, β_0 plays a crucial role in determining whether the system settles into a chaotic or periodic attractor.

Similarly, Figs. 21(c) and 21(d) display the HTBD for δ. Observe that the HTBD for δ shares some similarities with the HTBD for β_0, as the general shape of these bifurcations appears very similar. Nonetheless, for the set of parameters considered, there is only one bistable region in $\delta \in [0.19, 0.22]$, which represents 7.5% of the analyzed δ range and shows the coexistence of a chaotic and a periodic attractor. We restric δ in the interval $[0.1, 0.5]$ because outside of this range, but in $\delta \in [0, 1]$, the solutions are periodic.

Figures 22(a) and (b) show the HTBD for β_1, while Figs. 22(c) and (d) correspond to γ. For β_1, there is a single bistable range, highlighted by the gray background, within the interval $\beta_1 \in [0.25, 0.32]$, which is 7% of the β_1 range. As β_1 increases, the amplitude of the chaotic attractors in the i_{p} section also grows. However, for $\beta_1 > 0.9$, the opposite behavior is observed in the i_{s} section (Fig. 22(b)). This discrepancy arises due to the method used to construct the bifurcation diagrams.

Additionally, numerous transitions from periodic to chaotic dynamics occur as β_1 varies, with some of these transitions being period-doubling bifurcations. For higher values of β_1 (i.e., $\beta_1 > 0.9$), only chaotic solutions are observed. This behavior is expected, as β_1 amplifies the influence of the nonlinear term in Eqs. (4.35) and (4.36).

By fixing $\beta_1 = 0.28$ and using γ as the control parameter (Figs. 22(c) and (d)), a bistable

Figure 21 – Hysteresis type bifurcations diagram (HTBD) for β_0, in the panels (a) and (b), and for δ in the panels (c) and (d). Panels (a) and (c) show the local i maxima point, while panels (b) and (d) exhibit the stroboscopic section. We consider: $\alpha = 35.84$, $b = 0.02$, $\omega = 2\pi$, $\gamma = 100$, $\beta_1 = 0.28$. In panels (a) and (b): $\delta = 0.20$. In panels (c) and (d): $\beta_0 = 300$.

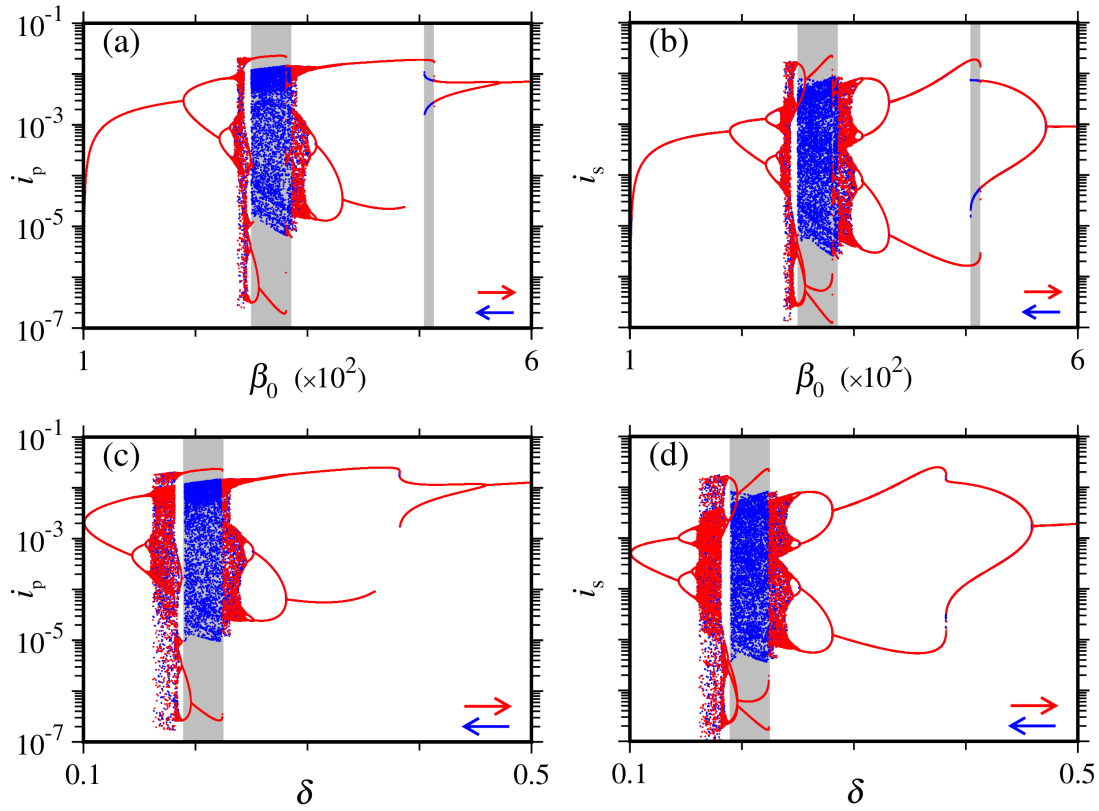

Source: Adapted from Ref. (96).

region emerges in $\gamma \in [108, 123]$, corresponding to 19% of the analyzed range. For this parametric configuration, chaotic solutions appear only in the interval $90 < \gamma < 150$. In this range, bifurcations drive the dynamics to chaos and subsequently to a bistable state, where a 2-period attractor coexists with a chaotic one. Regarding the period of the periodic attractor, it is observed that in the i_s section, the period briefly increases to 3 in a narrow range.

4.5.1 Bifurcation diagram for the inverse of latent period

The final parameter analyzed is α, which is associated with the latent period and plays a key role in understanding the dynamics of many diseases (110). For this part of the study, we use the following parameter configuration: $\delta = 0.25$, $\beta_0 = 270$, $\beta_1 = 0.28$, $\gamma = 100$, and $b = 0.02$.

Figures 23(a) and 23(b) display the HTBD for i_p and i_s, respectively. Unlike the results shown in Figs. 21 and 22, these figures are predominantly highlighted by the gray background.

Figure 22 – Hysteresis type bifurcations diagram (HTBD) for β_1, in the panels (a) and (b), and for γ in the panels (c) and (d). Panels (a) and (c) show the local i maxima point, while panels (b) and (d) exhibit the stroboscopic section. We consider: $\alpha = 35.84$, $b = 0.02$, $\omega = 2\pi$, and $\delta = 0.25$. In panels (a) and (b): $\gamma = 100$ and $\beta_0 = 270$. In panels (c) and (d): $\beta_1 = 0.28$ and $\beta_0 = 300$.

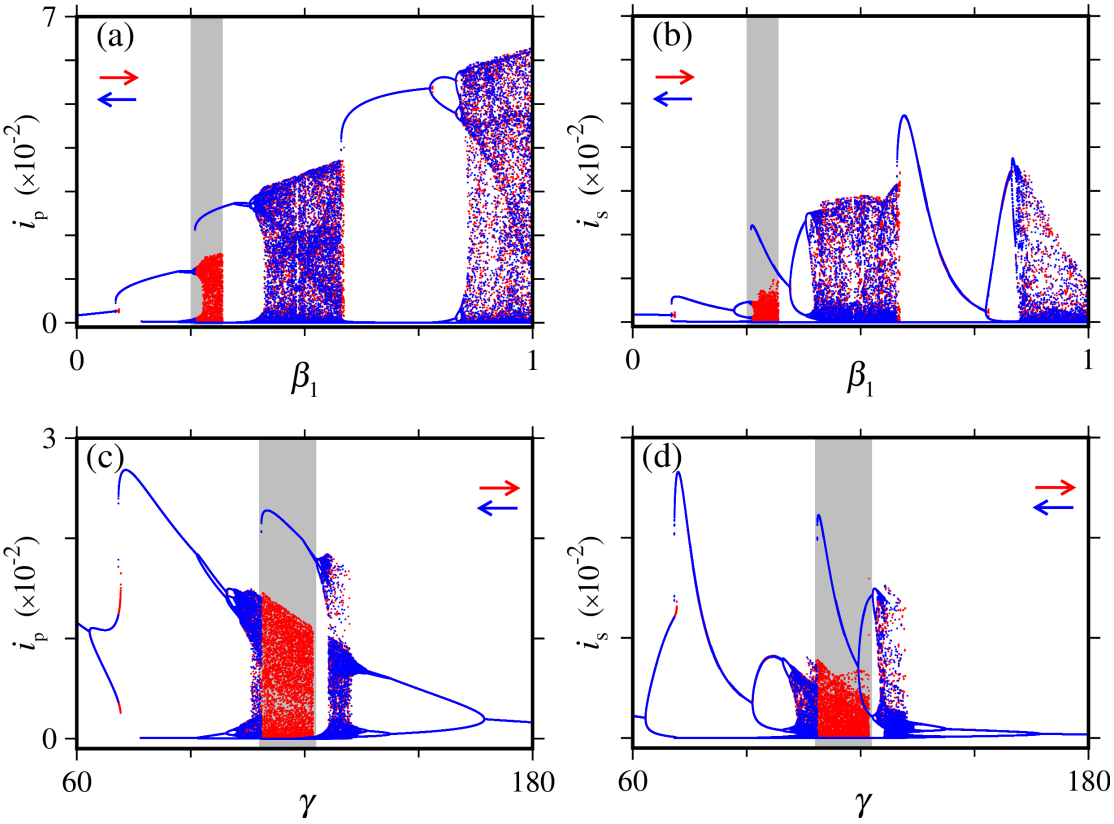

Source: Adapted from Ref. (96).

This is because approximately 70% of the analyzed α range is characterized by a bistable solution, involving the coexistence of periodic and chaotic attractors.

Figure 23 – Hysteresis type bifurcations diagram (HTBD) for α. Panels (a) and (b) show the local i maxima point and the stroboscopic section, respectively. We consider: $\delta = 0.25$, $\beta_0 = 270$, $\beta_1 = 0.28$, $\gamma = 100$, and $\omega = 2\pi$.

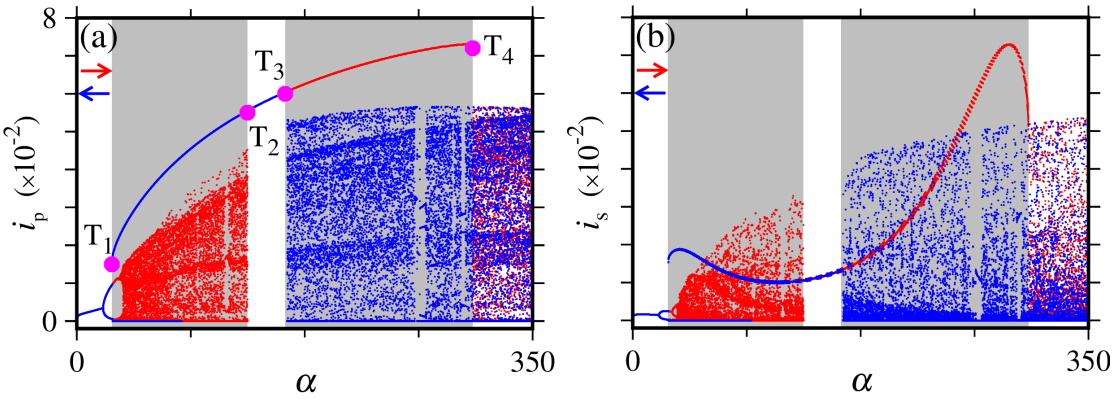

Source: Adapted from Ref. (96).

In Fig. 23(a), four critical points, marked by magenta circles and labeled as T_1, T_2, T_3, and T_4, are identified at $\alpha = 27$, 130.88966, 161.69990, and 303.88407, respectively. These points mark transitions where the system changes its dynamical behavior between periodic and chaotic states. Let us analyze these transitions in detail.

As α increases from 0, the system first reaches point T_1. At this point, the blue branch undergoes a sudden change in values, while the red branch continues along the same path. This indicates the coexistence of two distinct periodic attractors. The blue branch represents periodic solutions, whereas the red branch undergoes cascades of period-doubling bifurcations before transitioning into a chaotic attractor.

This behavior persists until point T_2, where a crisis occurs. A crisis is defined as a sudden change in a chaotic attractor, caused by a collision between a chaotic attractor, and an unstable fixed point or periodic orbit (111, 112). Such events can alter the size of the chaotic attractor or lead to the abrupt destruction of its basin of attraction. Additionally, transient chaos may emerge as a consequence.

Transient chaos (113) is observed in the range $[T_2, 130.89666]$. To evaluate the average transient lifetime ($\langle\tau\rangle$), we consider 200 initial conditions from the chaotic basin. Our results indicate that $\langle\tau\rangle$ follows a Gaussian distribution centered at 28×10^4 years. In this range, the basin of attraction comprises both chaotic and periodic orbits. However, the chaotic basin is extinct linearly and smoothly as the transient lifetime increases.

Between points T_2 and T_3, the system exhibits only one periodic attractor. When this attractor reaches T_3, a new crisis occurs for the blue branch, giving rise to a chaotic attractor. Although the blue branch becomes chaotic, the red branch remains periodic. In the interval $[T_3, 161.70849]$, another transient chaotic regime emerges, with $\langle\tau\rangle = 3 \times 10^4$ years. In this regime, transient chaos also leads to a linear and smooth reduction of the basin as the transient lifetime increases.

The range $[T_3, T_4]$ features the coexistence of a periodic attractor (red branch) and a chaotic attractor (blue branch). The chaotic attractor includes some periodic windows for certain values of α, but remains predominantly chaotic. The bistability ends at T_4, where a saddle-node bifurcation occurs and the red branch become chaotic. However, the periodic orbit (red branch)

goes to chaos slowly; i.e., a transient solution exists. To verify the saddle-node bifurcation, we consider a ball of initial conditions around to the critical point. After that, we plot the evolution of these initial conditions in the phase space, observing the contraction and expasion in different directions. Moreover, we compute the transient dynamics in this bifurcation.

To analyze this transition, we consider 200 initial conditions from the periodic basin and compute $\langle\tau\rangle$. In this case, $\langle\tau\rangle \propto (\alpha - T_4)^{\eta}$, with $\eta = -0.5025 \pm 0.0002$ for $\alpha > T_4$. After this transient, the periodic points coalesce into chaotic orbits through the saddle-node bifurcation. The transient solution persists until 1% beyond T_4. During the transient dynamics, 19% of the points in the basin evolve into periodic orbits. However, after a transient duration of 50,800 years, an abrupt change occurs, leaving only chaotic orbits in the basin.

Due to the coexistence of two attractors in the intervals $[T_1, T_2]$ and $[T_3, T_4]$, we compute the basins of attraction for $\alpha = 100$ and $\alpha = 200$. The results are shown in Figs. 24(a) and 24(b), respectively. In both panels, the following color scheme is used: black represents chaotic orbits and yellow represents periodic orbits.

For $\alpha = 100$, 53.6% of the considered initial conditions evolve into chaotic orbits, with the remaining 46.4% leading to periodic orbits. To compute these basins, we consider $s_0, e_0, i_0 \in [0, 0.2]$. As α varies within the range $[T_1, T_2]$, the fractions of initial conditions leading to chaotic or periodic attractors also change dynamically.

Figure 24(b) illustrates the basin of attraction for $\alpha = 200$. In this case, approximately 56.6% of the considered initial conditions lead to chaotic attractors, while the remaining 43.4% lead to periodic attractors. As α increases, the probability of an initial condition evolving to a periodic attractor decreases following a cubic function. Near T_3, this probability is around 43%, but as α approaches T_4, it decreases to approximately 22%.

4.5.2 Tipping point

One of the key characteristics of chaotic solutions is their unpredictability (114, 115), which is proportional to $1/\lambda$, where λ is the largest Lyapunov exponent (51). In this context, the solution presented in Fig. 23 is particularly interesting because it demonstrates a transition from a desirable state (periodic) to an undesirable one (chaotic) as α is slowly varied. Such

Figure 24 – Basins of attraction for $\alpha = 100$ (a) and $\alpha = 200$ (b). We consider: $\delta = 0.25$, $\beta_0 = 270$, $\beta_1 = 0.28$, $\gamma = 100$, and $\omega = 2\pi$.

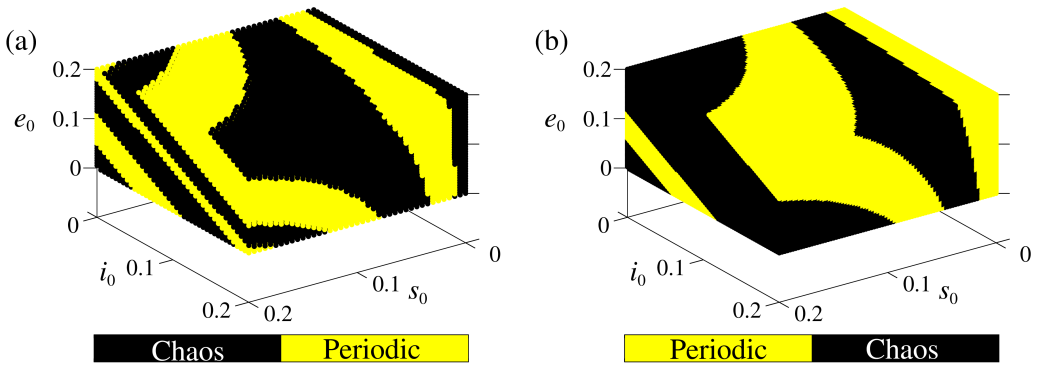

Source: Adapted from Ref. (96).

transitions can be interpreted as tipping phenomena.

When a control parameter is varied beyond a certain threshold, the system may switch between alternative states. These variations can result from external perturbations or gradual shifts in the parameter. The points at which such changes occur are known as tipping points (116). Mathematically, these transitions often correspond to saddle-node bifurcations (109). Between these thresholds, the system may exhibit bistability, where both solutions coexist (117).

From Fig. 23, we observe that the range $[T_2, T_3]$ contains only periodic solutions, whereas for $\alpha > T_4$, only chaotic attractors are present. This transition from the periodic state in $[T_2, T_3]$ to the chaotic state for $\alpha > T_4$ is shown in Fig. 25.

Starting on the green branch (predictable state), we gradually increase the control parameter, entering the bistable region. As seen in Fig. 23, this corresponds to following the periodic branch. Once reaching threshold 1, a saddle-node bifurcation occurs, causing the system to shift to an unpredictable state, represented by the red branch in Fig. 25.

Conversely, if we start on the red branch (chaotic state) and decrease the control parameter, the system crosses the bistable region and reaches threshold 2. At this point, the system transitions back to a predictable state. In this scenario, the transition at threshold 2 is not a saddle-node bifurcation but a crisis. This behavior differs from the conventional.

Additionally, both solutions are connected by an unstable branch within the bistable interval. For instance, if we take the unstable component near T_4 and decrease the control parameter, the

system reverts to a periodic solution for $\alpha < T_3$.

Figure 25 – Representation of a tipping point solution. The green branch represents a predictable (desirable) solution while the red one is related to unpredictable solutions (undesirable).

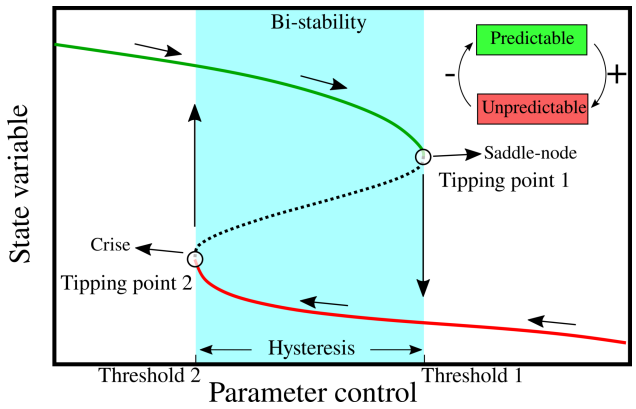

Source: The author.

4.6 SUMMARY

In this chapter, we demonstrated that a simple SEIRS model with a time-dependent contact rate leads to very complex solutions. The solutions can be periodic, chaotic, bistable, or multistable. Besides this model has been studied for a long time, we uncover a new complex dynamics, that was not observed previously. In addition, we also show that the latent period is a crucial parameter for understanding the spread of certain diseases, once it can be related to tipping point solutions.

5 CONSTANT VACCINATION CAMPAIGN AND DYNAMICAL ASPECTS

As presented in the previous chapter, the seasonal forced SEIRS model presents various complex solutions. Now, we include a constant vaccination on the S individuals and newborns in the model and explore the effects of such modification. The results present in this chapter are part of the papers (118, 119). In the Ref. (118) we mainly explore constant and periodic vaccination campaigns, and in Ref. (119) we discuss the effects into the dynamical behavior of these modifications as well as implications of seasonal immunization programs.

Constant vaccination rates can be used to model mass vaccination campaigns (120). Such campaigns involve vaccinating a given population in a short period. Examples include mass campaign against measles (121), smallpox (122), and COVID-19 (123).

5.1 MODEL

The constant vaccination can be modeled by transferring S individuals to R compartment, such that $S \xrightarrow{\kappa\nu} R$, where κ and ν are the vaccination efficacy and rate, respectively. Another mechanism is the vaccination of newborn individuals, which takes a rate p of newborns (from S) and move to R (124). Including these modifications, we obtain a new representation of SEIRS model, according to Fig. 26.

Figure 26 – Representation of SEIRS model with vaccination in S individuals and in newborns.

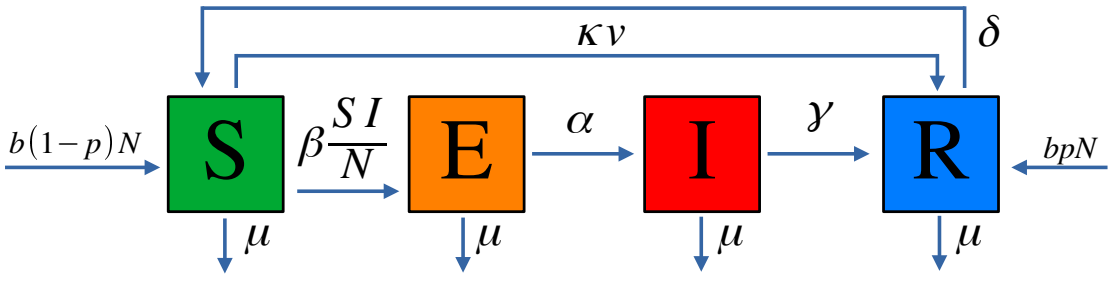

Source: The author.

Considering these modifications, the model become

$$\frac{ds}{dt} = b(1-p) - \mu s - \beta si + \delta(1-s-e-i) - \kappa vs, \tag{5.1}$$
$$\frac{de}{dt} = \beta si - (\alpha+\mu)e, \tag{5.2}$$
$$\frac{di}{dt} = \alpha e - (\gamma+\mu)i, \tag{5.3}$$

where $r = 1-s-e-i$. Observe that $b = \mu$, but we keep both notation just to elucidate the contributions of births and deaths. Now, we explore how the equilibrium points are affected by the inclusion of p, κ, and v.

5.1.1 DFE solution

Analogously to Chapter 4, the DFE solution for Eqs. (5.1), (5.2), and (5.3) is $(s,e,i) = (s,0,0) \equiv \left(\widehat{s},\widehat{e},\widehat{i}\right)$. Following the same steps as did in Chapter 4, we obtain

$$\left(\widehat{s},\widehat{e},\widehat{i}\right) = \left(\frac{b(1-p)+\delta}{\kappa v+\delta+b},0,0\right). \tag{5.4}$$

The stability of this fixed point is guaranteed if all eigenvalues of the Jacobian matrix $(\mathbb{J}_{\left(\widehat{s},\widehat{e},\widehat{i}\right)})$ have negative real part (51).

Computing the Jacobian matrix at $\left(\widehat{s},\widehat{e},\widehat{i}\right)$, we get

$$\mathbb{J}_{\left(\widehat{s},\widehat{e},\widehat{i}\right)} = -\begin{bmatrix} (\kappa v+\delta+b) & \delta & (\beta\widehat{s}+\delta) \\ 0 & (\alpha+b) & -\beta_0\widehat{s} \\ 0 & -\alpha & (\gamma+b) \end{bmatrix}, \tag{5.5}$$

with associated eigenvalues equal to

$$\Delta_1 = -(\kappa v+\delta+b), \tag{5.6}$$
$$\Delta_2 = \frac{-(\alpha+\gamma+2b) - \sqrt{(\alpha-\gamma)^2+4\alpha\beta\widehat{s}}}{2}, \tag{5.7}$$
$$\Delta_3 = \frac{-(\alpha+\gamma+2b) + \sqrt{(\alpha-\gamma)^2+4\alpha\beta\widehat{s}}}{2}. \tag{5.8}$$

Once the parameters of the model are positive, $\Delta_{1,2}$ is negative and the only eigenvalue that needs to be examined is Δ_3. The stability is ensure if $\Delta_3 < 0$, where the solutions of this inequality leads to

$$R_0 \equiv \frac{\alpha\beta\widehat{s}}{(\alpha+\mu)(\gamma+\mu)} < 1, \tag{5.9}$$

where $\widehat{s} = (b(1-p)+\delta)/(\kappa v+\delta+b)$. Thus, the equilibrium occurs if $R_0 < 1$. As $R_0 \propto 1/v$, as v increase, R_0 decrease. Furthermore, observe that, if $p = \kappa v = 0$, then $\widehat{s} = 1$ and we recover the R_0 for the model without vaccine.

5.1.2 Endemic solution

The endemic point (s^*, e^*, i^*) in terms of R_0 is equal to

$$s^* = \frac{(\alpha+b)(\gamma+b)}{\alpha\beta} = \frac{\widehat{s}}{R_0}, \tag{5.10}$$

$$e^* = \frac{(\gamma+b)\,[b(1-p)+\delta]}{\alpha\beta\widehat{s}+\delta(\alpha+\gamma+b)R_0}\,(R_0-1)\,, \tag{5.11}$$

$$i^* = \frac{\alpha\,[b(1-p)+\delta]}{\alpha\beta\widehat{s}+\delta(\alpha+\gamma+b)R_0}\,(R_0-1)\,, \tag{5.12}$$

with the corresponding Jacobian matrix written as

$$\mathbb{J}_{(s^*,e^*,i^*)} = -\begin{bmatrix} (\beta i^*+\kappa v+\delta+b) & \delta & (\beta s^*+\delta) \\ -\beta i^* & (\alpha+b) & -\beta s^* \\ 0 & -\alpha & (\gamma+b) \end{bmatrix}. \tag{5.13}$$

The characteristic polynomial is given by

$$P(\Delta) = \Delta^3 + c'_2\Delta^2 + c'_1\Delta + c'_0, \tag{5.14}$$

where the coefficients are

$$c'_0 = (\beta i^* + \kappa v + \delta + b)\left[(\alpha + b)(\gamma + b) - \alpha\beta s^*\right] + \\ + \beta i^*\left[\alpha(\beta s^* + \delta) + \delta(\gamma + b)\right], \tag{5.15}$$

$$c'_1 = (\beta i^* + \kappa v + \delta + b)(\alpha + \gamma + 2b) + \\ + (\alpha + b)(\gamma + b) + \beta(\delta i^* - \alpha s^*), \tag{5.16}$$

$$c'_2 = \beta i^* + \kappa v + \alpha + \gamma + \delta + 3b. \tag{5.17}$$

Considering $c'_{0,1,2}$ and the Routh–Hurwitz criterion (125), it is possible to find a relationship for the endemic equilibrium stability. In this sense, the real part of $\Delta_{1,2,3}$ is less than zero if and only if

$$c'_0, c'_1, c'_2 > 0, \tag{5.18}$$

and

$$c'_0 < c'_1 c'_2. \tag{5.19}$$

Accomplished the above conditions, the endemic solution is attractive. During the simulations, we observe that this point is asymptotically stable, for the considered parameters.

5.2 VACCINATION THRESHOLD

As done in Chapter 4, we consider a time-dependent contact rate given by Eq. (4.32), with $\omega = 2\pi$. Therefore, the complete model is

$$\dot{s} = b(1-p) - \mu s - \beta_0(1 + \beta_1\cos(\tau))si + \delta(1 - s - e - i) - \kappa v s, \tag{5.20}$$

$$\dot{e} = \beta_0(1 + \beta_1\cos(\tau))si - (\alpha + \mu)e, \tag{5.21}$$

$$\dot{i} = \alpha e - (\gamma + \mu)i, \tag{5.22}$$

$$\dot{\tau} = \omega. \tag{5.23}$$

The basic reproduction number obtained previously (Eq. (5.9)) is valid for the autonomous case, which is equivalent when we have $\beta_1 = 0$ in Eqs. (5.20)-(5.23). However, to obtain

R_0 for $\beta_1 \neq 0$, we adopt the same techniques as discussed in Chapter 4, getting R_0^+ and R_0^-. Considering these limits and imposing the DFE condition in the complete system, we obtain two quotas for minimum vaccination coverage, which are

$$v_- > \frac{\alpha[b(1-p)+\delta]}{\kappa(\alpha+b)(\gamma+b)}\beta_0 - \frac{(\delta+b)}{\kappa}, \tag{5.24}$$

$$v_+ > \frac{\alpha[b(1-p)+\delta]}{\kappa(\alpha+b)(\gamma+b)}\beta_0(1+\beta_1) - \frac{(\delta+b)}{\kappa}. \tag{5.25}$$

The extinction of the disease can be obtained under the condition $v \geq v_+$ is verified. However, in some cases, the upper limit can be greater than enough, and $v \geq v_-$ is enough to reach DFE. In this chapter, we show that for most of the investigated cases the relation v_- describes very well the limits for DFE.

The relations given by the inequalities (5.24) and (5.25), establishes a minimum of v to extinct the disease in the population. To have a practical example, let us assume $\kappa = 1$, $p = 0.25$ $b = 0.02$, $\beta_0 = 270$, $\delta = 0.25$, $\alpha = 100$ and $\gamma = 100$. For these parameters, a vaccination rate equal to $v_- = 0.445$ (or 44.5% of s individuals) is enough to ensure DFE.

5.3 CONSTANT VACCINATION STRATEGY

The numerical integration of the system is given by the same method employed in Chapter 4 considering now $\kappa = 1$. This consideration does not affect the results, once the term κ is absorved by v.

Figure 27 shows three numerical results for $p = v = 0$ (red line), $(p,v) = (0.25, 0.2)$ (blue line), and $(p,v) = (0.25, 0.4)$ (green line). Figure 27(a) show the projection of the attractor in the plane $i \times s$, while 27(b) exhibit the i time series. In these results, we consider $b = 0.02$, $\beta_0 = 800$, $\beta_1 = 0.20$, $\delta = 0.25$, $\alpha = 40$, $\gamma = 100$ and $\omega = 2\pi$. As initial condition we adopt $(s_0, e_0, i_0) = (0.9, 0, 0.1)$ and discard the first 10^5 integration steps as transient. For this parameter set, the solutions are limit cycles! As v increases the cycles contract showing a decrease in the i values. A significant decrease in the local maxima of i is observed in panel (b) comparing the curves. Looking at the red and the blue curves, a reduction of 21.4% in the peak infections occurs in the presence of a vaccine. When the vaccination campaign is intensified, i.e., $v = 0.4$, the peak

of infected reduces to $\approx 38.9\%$.

Figure 27 – Numerical solutions for SEIRS model for different vaccination rates. The red line is the reference curve for $p = v = 0$, the blue for $p = 0.25$ and $v = 0.2$, and the green one for $p = 0.25$ and $v = 0.4$. Panel (a) shows the projection of the attractor in the plane $i \times s$. Panel (b) displays the time series for i. We consider $b = 0.02$, $\beta_0 = 800$, $\beta_1 = 0.20$, $\delta = 0.25$, $\alpha = 40$, $\gamma = 100$ and $\omega = 2\pi$.

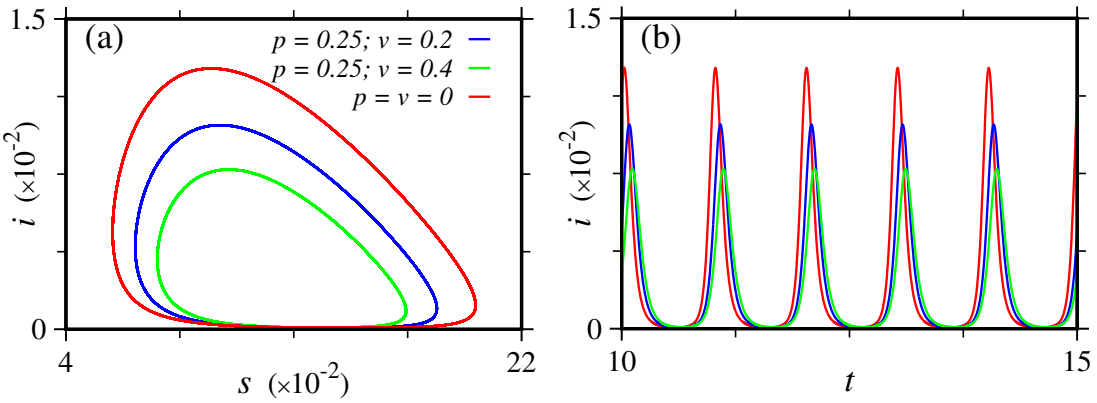

Source: Adapted from Ref. (118).

In the next numerical simulations, we consider the following parameters: $b = 0.02$, $\beta_0 = 270$, $\beta_1 = 0.28$, $\delta = 0.25$, $\alpha = 100$, $\gamma = 100$ and $\omega = 2\pi$.

As observed in Fig. 27, the vaccination campaign is able to reduce the number of infected individuals. To measure this reduction, we propose a measure based on the ratio between the area under the i curve with (A_v) and without (A_0) vaccine, given by

$$\theta = \frac{A_\mathrm{v}}{A_0}. \tag{5.26}$$

Therefore, to compute θ, first we generate an i time series for a given set of parameters with $p = v = 0$ and calculate A_0. After that, we fix the same parameters, but with $p \neq 0$ and $v \neq 0$, and generate another i time series, computing the A_v variable. The quantities A_v and A_0 are easily computed in the time window $t \in [t_0, t_0 + \Delta t]$ by means of

$$A_\mathrm{v} = \int_{t_0}^{t_0+\Delta t} i(t)dt, \tag{5.27}$$

$$A_0 = \int_{t_0}^{t_0+\Delta t} i(t; p = v = 0)dt. \tag{5.28}$$

Equation (5.26) establishes an important relation. If $\theta < 1$, the vaccination campaign can reduce the number of infections. On the other hand, since $\theta > 1$ the vaccination campaign has negative effects, and with $\theta \approx 1$ the vaccination does not affect the dynamics.

Considering a time interval of 75 years, Fig. 28 shows θ as a function of v in panel (a) and p in panel (b). In panel (a), we fix $p = 0.25$ and explore the range $v \in [0, 1]$. The black curves in both panels represent the first 75 years of simulation, including the transient, while the blue curve represents results after 100 years of simulation, excluding the transient.

When the transient is included, θ does not reach 0 for any value of v. This occurs because the initial condition for i individuals ensures that $A_v > 0$. From panel (a), we also validate our analytical expression given by Eq. (5.24), where the DFE is achieved for $v \approx 0.44$. As the limit given by Eq. (5.24) does not depends on time, increasing the window time to 100 or 125 years the result $v \geq 0.44$ does not changes.

Fixing $v = 0.1$, we obtain the results shown in Fig. 28(b). This results show that is necessary to vaccinate all the newborns to obtain a reduction of $\approx 12.5\%$ in the i curve. Therefore, is more effective to vaccinate adults than newborns.

Figure 28 – Effects of v and p on the ratio θ. In the panel (a) we use $p = 0.25$ and in the panel (b) $v = 0.1$. We consider $b = 0.02$, $\beta_0 = 270$, $\beta_1 = 0.28$, $\delta = 0.25$, $\alpha = 100$, $\gamma = 100$ and $\omega = 2\pi$.

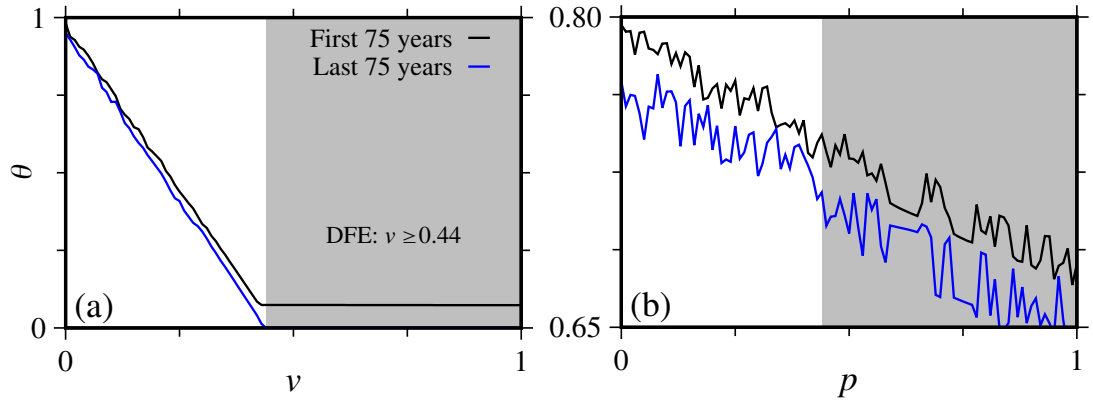

Source: Adapted from Ref. (118).

To investigate the broader relationship between v, p, and θ, we construct the parameter plane $p \times v$ (Fig. 29), where the color scale represents θ. Using the same time window of 75 years after the transient, the results indicate that v is more relevant than p in decreasing θ. Specifically, for this parameter configuration, the DFE is achieved when $v \geq v_c$, with $v_c = (8.22 - p)/18.55$ represented by the dashed white line in Fig. 29. To better understand the condition $v \geq v_c$, let

us consider the worst case, i.e., $p = 0$. In this case, the DFE is achieved for $v_c = 0.44$, meaning that any $v \geq v_c$ leads to DFE. The best case occurs when $p = 1$, where $v_c = 0.39$.

Figure 29 – Parameter plane $p \times v$ with θ in color scale. θ is calculated for a time interval equal to 75 years. The dashed white line indicates the limit for DFE. We consider $b = 0.02$, $\beta_0 = 270$, $\beta_1 = 0.28$, $\delta = 0.25$, $\alpha = 100$, $\gamma = 100$ and $\omega = 2\pi$.

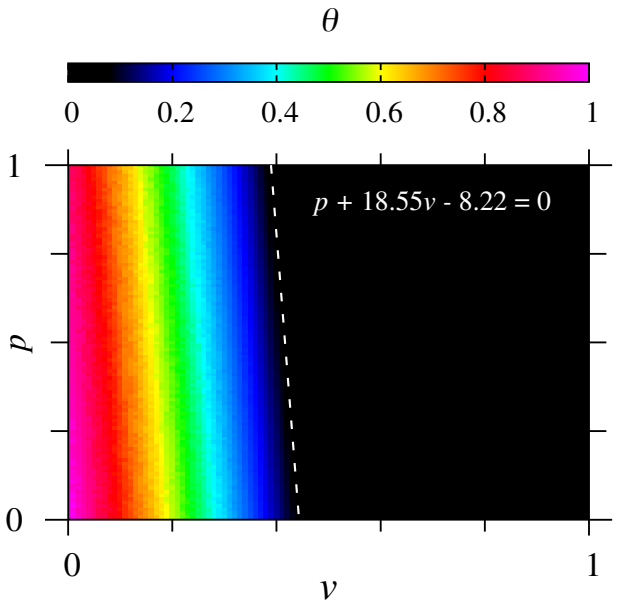

Source: Adapted from Ref. (118).

As observed, the effects of v on the decrease of i are more significant than those of p. To explore the effects of v into the dynamics, we fix $p = 0.25$ and study the implications of v on the system behavior by analyzing the HTBD (Fig. 30). To compute i_p, we discard the first 10^5 integration steps as transient and evaluate the i time series over the last 75 years. The set of parameters used to construct this HTBD corresponds to a bistable regime when $p = v = 0$. In this context, constant vaccination can act as a control mechanism for bistability at certain values. However, bistability persists for other parameter ranges, as highlighted by the gray backgrounds. In the interval $v \in (0.155, 0.165)$ corresponding to the gray background, the periodic orbit (blue branch) has a maximum value of $i_{max} \approx 0.032$, whereas the chaotic orbit (red branch) exhibits a smaller maximum of $i_{max} \approx 0.026$. The second bistable range is in $v \in (0.256, 0.263)$, where the periodic orbit has extreme values of i slightly higher than those of the chaotic one. As v increases, the system goes to periodic behavior until the DFE, which is reached at $v = 0.44$.

Figures 31(b) and 31(c) show the projection of the attractors on the $i \times s$ plane. These

Figure 30 – Hysteresis type bifurcations diagram (HTBD) for v. We consider $p = 0.25$, $b = 0.02$, $\beta_0 = 270$, $\beta_1 = 0.28$, $\delta = 0.25$, $\alpha = 100$, $\gamma = 100$ and $\omega = 2\pi$.

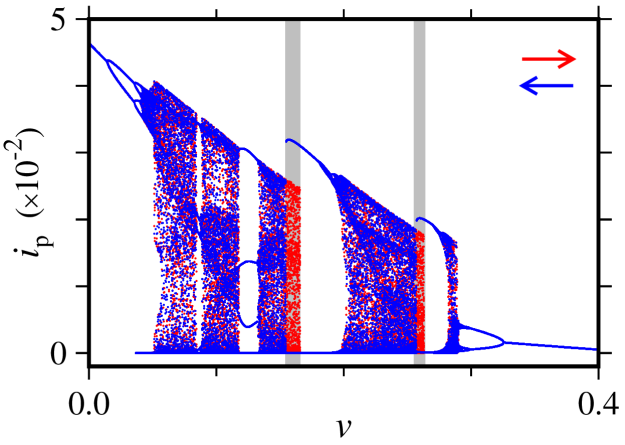

Source: Adapted from Ref. (118).

attractors are computed for the bistable dynamics, in particular for $v = 0.16$ and $v = 0.26$. To obtain the chaotic attractor for $v = 0.16$, we use the initial condition $P_1(s_0, e_0, i_0) = (0.9, 0, 0.1)$, while for the periodic attractor, the initial condition is $P_2(s_0, e_0, i_0) = (0.3, 0.03, 0.03)$.

On the other hand, for $v = 0.26$, P_1 results in the periodic attractor, while P_2 leads to the chaotic one. In both cases, it is observed that the peak value of the periodic solution is higher than that of the chaotic solution.

Figure 31 – Projection in the plane $i \times s$ of periodic (blue line) and chaotic (red line) attractors coexisting for $v = 0.16$ (panel (a)) and $v = 0.26$ (panel (b)). The initial conditions are $P_1(s_0, e_0, i_0) = (0.9, 0, 0.1)$ and $P_2(s_0, e_0, i_0) = (0.3, 0.03, 0.03)$. For $v = 0.16$, P_1 leads to a chaotic attractor, while P_2 to a periodic one. For $v = 0.26$, P_1 leads to periodic and P_2 to chaotic attractor. We consider $p = 0.25$, $b = 0.02$, $\beta_0 = 270$, $\beta_1 = 0.28$, $\delta = 0.25$, $\alpha = 100$, $\gamma = 100$ and $\omega = 2\pi$.

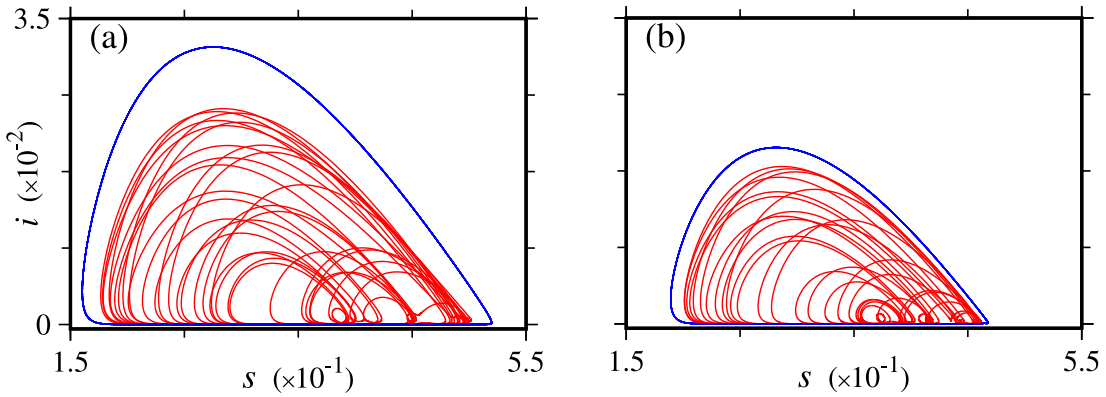

Source: Adapted from Ref. (118).

5.4 DYNAMICAL BEHAVIOR FOR CONSTANT VACCINATION

As observed, the most significant parameter for constant vaccination is v. To investigate more deeply the influence of v on the dynamical behavior, we compute the Lyapunov exponents for each pair $v \times [\cdot]$, where $[\cdot]$ represents one of the model parameters described by Eqs. (5.20), (5.21), (5.22), and (5.23). To compute and plot the Lyapunov exponents, we employ the same methodology discussed in Chapter 4. In this section, the initial condition is $s_0 = 1 - e_0 - i_0$, with $i_0 = 10^{-3}$ and $e_0 = 0$, and the transient is fixed at 5×10^5 integration steps.

The results for the parameter planes $v \times \alpha$ and $v \times \gamma$ are shown in Fig. 32(a) and 32(b), respectively. The color scale represents the Lyapunov exponent (λ). To generate the same pattern in the color scale for the next planes, we restrict $\lambda \in [-0.4, 0.4]$.

To numerically determine the DFE solutions, we analyze A_{v} over i and e. When A_{v} associated with the i and e curves is less than 10^{-6}, we identify the solution as DFE. Based on this criterion, we extract the points from the parameter planes that separate the DFE from the non-DFE regions. These points are represented by the magenta curve in both panels.

For panel (a), we fit these points and obtain the relation $v(\alpha) = a/(1 + b\alpha^{-1}) + c$, where $a = 0.7089 \pm 0.0001$, b is the birth rate, and $c = 0.2702 \pm 0.0001$. Using the parameters described in the caption of Fig. 32(a) in Eq. (5.24), we get $v(\alpha) = 0.715/(1 + 0.02\alpha^{-1}) - 0.27$. Notably, the numerical and theoretical expressions are nearly identical.

For a fixed α, variations in v can change the dynamical behavior from periodic to chaotic dynamics (Fig. 32(a)). To exemplify, we mark some transitions induced by period-doubling by the gray squares and via crises by green circles. We select just some transitions, but can exist other kinds of bifurcations. By computing A_{v} over the infected curve, our simulations suggest that A_{v} is independent of the type of orbits.

Fixing $\alpha = 100$, the parameter plane $v \times \gamma$ is shown in Fig. 32(b). In this case, the DFE is also determined by a non-linear relationship given by $v(\gamma) = a/(\gamma + b) + c$, where $a = 70.47 \pm 0.02$, $c = 0.2699 \pm 0.0002$, and b represents the birth rate. This relationship establishes $v \propto \gamma^{-1}$. The same behavior is observed in Eq. (5.24).

The relation $v \propto \gamma^{-1}$ indicates that as γ increases, less vaccination is required to achieve DFE. This is because, as γ increases, individuals transition faster to R and then return to S,

where they receive vaccination and move back to R. This flow helps maintain DFE and other parameters are not enough to sustain the disease spread.

Conversely, as γ decreases to $\gamma = 56.56$, more vaccination is needed to achieve DFE. For values $\gamma < 56.56$, even with $v = 1.0$, DFE cannot be obtained. For a fixed γ value, bifurcations via period-doubling and crises can also occur, as indicated by the gray squares and green circles, respectively.

Figure 32 – Parameter planes $v \times \alpha$ and $v \times \gamma$ in the panels (a) and (b), respectively. For (a) we use $\gamma = 100$ and for (b) $\alpha = 100$. The color scale shows the Lyapunov exponent λ. We consider $b = 0.02$, $\omega = 2\pi$, $\delta = 0.25$, $\beta_0 = 270$, $\beta_1 = 0.28$, and $p = 0.25$.

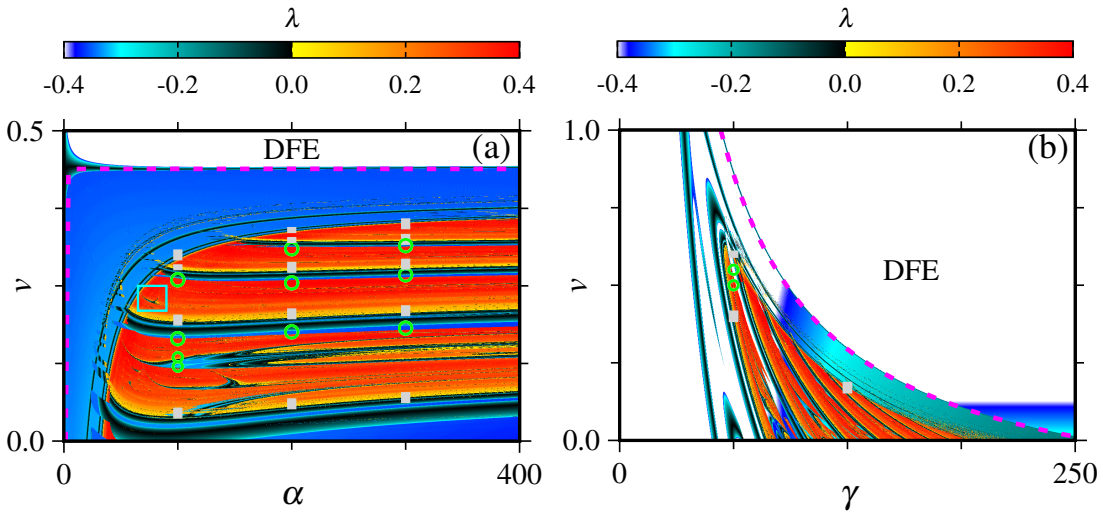

Source: The author.

The cyan square in Fig. 32(a) highlights a region where a shrimp structure exists (126), this region is magnified in Fig. 33. Shrimps are periodic structures embedded within chaotic bands (127). These structures frequently appear in parameter planes of non-linear dynamical systems (128–131), resulting from a peculiar arrangement of two saddle-node bifurcation curves and routes to chaos via period doubling (126,132). Shrimps are significant because, in their vicinity, cascades of similar periodic structures can lead to chaotic routes (133). Near these structures, small parameter changes can drastically alter the dynamics (131). In our case, we do not find a family of shrimps, but just the one highlighted in Fig. 33, which has period 5 in the main body. As far as we know, this result, together with our work in Ref. (97), are the only works that report the existence of this structures in epidemiological models, highlighting the complexity of this simple model.

Figure 33 – Shrimp structure located at the plane $\nu \times \alpha$. We consider $b = 0.02$, $\omega = 2\pi$, $\delta = 0.25$, $\beta_0 = 270$, $\beta_1 = 0.28$, and $p = 0.25$.

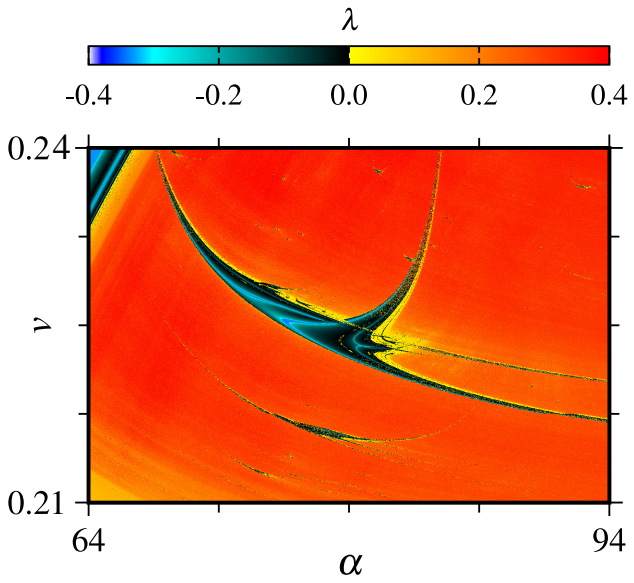

Source: The author.

The parameter plane $\nu \times \beta_0$, for $\gamma = 100$ and $\alpha = 100$, is shown in Fig. 34(a). For this configuration, the DFE is achieved above the line $\nu(\beta_0) = a\beta_0 - c$, with $a = 0.002 \pm 9 \times 10^{-7}$ and $c = -0.2701 \pm 0.0003$. A similar expression is derived from Eq. (5.24). In this parametric configuration, even for $\nu > 0.95$, chaotic orbits exist in the range $\beta_0 \in (560, 614)$. Additionally, some crises and period-doubling bifurcations are observed for specific β_0 values, marked by gray squares and green circles. For $\beta_0 \geq 488.5$, only non-DFE solutions are found, even when $\nu > 0.95$, with the orbits being either periodic or chaotic. However, for $\beta_0 > 604$, only periodic solutions persist. In this case, a high contact rate leads exclusively to periodic solutions.

Figure 34(b) shows the parameter plane $\nu \times \delta$, for $\beta_0 = 270$, which exhibits a similar structure to Fig. 34(a). In this case, the DFE is also achieved above a linear relationship between ν and δ, described as $\nu = a\delta - c$, where $a = 1.6724 \pm 0.0004$ and $c = 0.1848 \pm 0.0001$. This relation is consistent with Eq. (5.24). Some bifurcations via period-doubling and crises are highlighted by gray squares and green circles. For $\delta > 0.624$, only periodic solutions are observed. This range corresponds to an average to lost the immunity less than 1.6 years. In this context, for the given parametric setup, diseases with an immunity loss time of less than 1.6 years ($1/\delta < 1.6$) only periodic orbits exist. In contrast, illnesses with $1/\delta$ greater than 1.6 years can show chaotic or periodic dynamics.

Figure 34 – Parameter planes $v \times \beta_0$ and $v \times \delta$ in the panels (a) and (b), respectively. For (a) we use $\delta = 0.25$ and for (b) $\beta_0 = 270$. The color scale shows the Lyapunov exponent λ. We consider $b = 0.02$, $\omega = 2\pi$, $\delta = 0.25$, $\gamma = 100$, $\alpha = 100$, and $p = 0.25$.

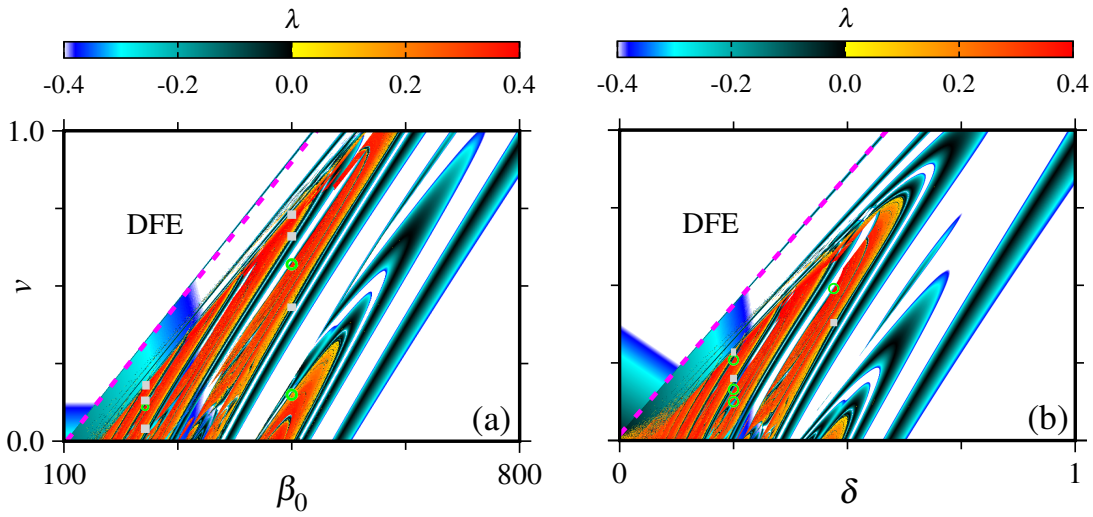

Source: The author.

The last two parameter planes are display in Fig. 35, with panel (a) representing $v \times \omega$ and panel (b) showing $v \times \beta_1$. First, we discuss the results for panel (a), where $\beta_1 = 0.28$. From Eq. (5.24), no dependence of ω is observed since this relation is derived for the limits of $\beta(t)$. In this case, a constant curve delimiting DFE solutions is expected. Our results confirm that, and the constant is $v = 0.44$. For $v > 0.44$, DFE is always achieved. Conversely, for $v < 0.44$ and $\omega \in (0.48, 3.26)\pi$, the orbits can be periodic or chaotic. For $\omega < 0.48\pi$ or $\omega > 3.26\pi$, only periodic orbits are observed. Additionally, we note that ω does not affect A_v. For $\omega = 2\pi$, some transitions induced by crises (green circles) or period-doubling (gray square) are marked.

Figure 35(b) is calculated for $\omega = 2\pi$. It is important to note that Eq. (5.24) is derived for $\beta_1 = 0$. Consequently, we expect that Eq. (5.24) provide an accurate description only for small values of β_1. Additionally, we have v_+ (Eq. (5.25)), but this equation also does not fully describe the DFE curve in Fig. 35(b). This limitation arises due to the strong non-linear contributions. From our fit, we propose $v(\beta_1) = a + c\beta_1 + d\beta_1^e$, where the coefficients are determined as: $a = 0.4398 \pm 0.0003$, $c = 0.7103 \pm 0.0006$, $d = -0.8114 \pm 0.0006$, and $e = 1.108 \pm 0.001$. Thus, Eqs. (5.24) and (5.25) are valid only in a certain range of β_1, which we estimate to be $\beta_1 < 0.4$. Therefore, deriving an equation that defines the thresholds for $\beta_1 \in [0, 1]$ remains an open question. For $\beta_1 > 0.12$ and $v < 0.38$, many chaotic structures

emerge as a function of β_1. When $\beta_1 = 0.5$ and v is varied, we observe transitions from periodic to chaotic behavior, induced by crises (green circles) and period-doubling bifurcations (gray squares).

Figure 35 – Parameter planes $v \times \omega$ and $v \times \beta_1$ in the panels (a) and (b), respectively. For (a) we use $\beta_1 = 0.28$ and for (b) $\omega = 2\pi$. The color scale shows the Lyapunov exponent λ. We consider $b = 0.02$, $\beta_0 = 270$, $\delta = 0.25$, $\alpha = 100$, $\gamma = 100$, and $p = 0.25$.

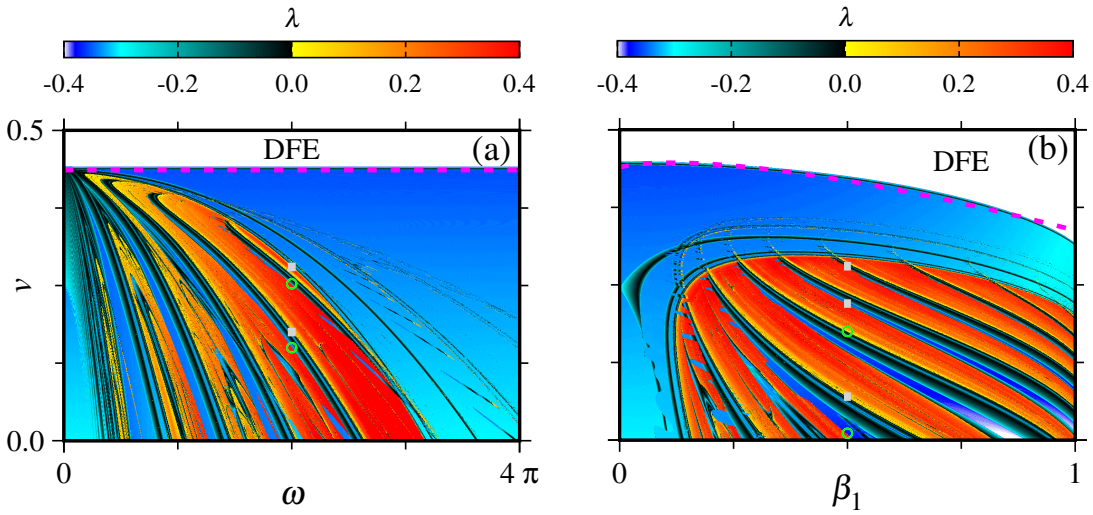

Source: The author.

5.5 SUMMARY

In this chapter, we examined the effects of constant vaccination in the SEIRS model with seasonal forcing. First, we derived an analytical expression for the minimum vaccination coverage, which provides insight into the vaccination rate required to ensure disease extinction. Subsequently, we explore numerical solutions of the model. Initially, we analyze the influence of vaccination on both susceptible and newborn individuals. Our findings reveal that vaccinating newborns has a smaller impact compared to vaccinating other susceptible individuals. In the second part, we investigate the effects of the vaccination rate on the dynamic behavior of the system. To achieve this, we construct parameter planes combining vaccination rates with other model parameters and compute the Lyapunov exponents to distinguish different types of orbits. Our results demonstrate that complex structures, such as shrimps, can emerge. Furthermore, we porpose a vaccination threshold that is valid for low seasonality degree.

6 FINAL REMARKS

In this thesis, we have analyzed a Susceptible–Exposed–Infected–Recovered–Susceptible (SEIRS) model with a time-dependent contact rate. Besides this model has been studied for a long time and many scholars (26), we have found new solutions and features of the model. We expect that these findings contribute to the mathematical epidemiology and the nonlinear dynamics theory.

In Chapter 2, we have presented the basic concepts of nonlinear dynamics that were employed in this work. The definitions involve a brief introduction to ordinary differential equations, stability of stationary solution, bifurcation, chaos, and Lyapunov exponents. Thus, this chapter is essential to establish some basic definitions that appear in the analysis of the considered epidemiological model.

In Chapter 3, we have introduced some basic definitions of mathematical epidemiology, such as the compartments, basic reproduction number, epidemic size, and the different kinds of steady solutions. We made this by introducing simple epidemic models, such as SI, SIS, SIR, and SEIR, in their simplest form, i.e., without forcing and demography characteristics. We demonstrated basic properties and showed the stability analysis for each model. In addition, regarding SEIR we showed one application, which is an extension to include two vaccination doses.

We introduced the SEIRS model in Chapter 4. For this, we deduced the basic reproduction number and studied the stability of the endemic and disease-free solutions. By adding the time-dependent contact rate, we explore how the frequency of the forcing associated with another parameter from the model affects the Lyapunov exponents. From this, we discovered the emergence of complex structures in the parameter plane. Motivated by these solutions, we discovered multistability in the model. We showed that many attractors can exist for the same parametric configuration. After that, we explored the bistable solutions, where periodic and chaotic attractors coexist. Regarding this point, we uncover that the latent period is a very important parameter from the modeling point of view because variations in this parameter can lead to unpredictable states.

In Chapter 5, we investigated the influence of a constant campaign in the model. For this, we also derived the steady solutions and demonstrated their stability properties. We showed an expression that gives the minimum vaccination coverage to obtain disease-free. By combining the constant vaccination and another parameter from the model, we explored how these parameter planes affect the Lyapunov exponents. We observed the emergence of typical complex structures, such as shrimps.

Overall, we demonstrated new features of the SEIRS model and its complexity dynamics. As open problems, we address two: i) verify if the structures reported in this thesis can be found in real diseases; and ii) derivation of a general an expression that establishes the disease-free solution when a time-dependent contact rate and vaccination are considered.

REFERENCES

1 World Health Organization. **Disease outbreaks**. Available on: https://www.emro.who.int/health-topics/disease-outbreaks/index.html Accessed on: 29 May 2024.

2 BRAUER, F.; CASTILLO-CHAVEZ, C.; FENG, Z. **Mathematical Models in Epidemiology**. 1. ed. Springer Nature, 2019.

3 LAST, J. M. **A dictionary of epidemiology**. 4th ed. New York: Oxford University Press, 2001.

4 GLATTER, K. A.; FINKELMAN, P. History of the Plague: An Ancient Pandemic for the Age of COVID-19. **The American Journal of Medicine**, v. 134, p. 176-181, 2021.

5 TUMPEY, T. M.; BASLER, C. F.; AGUILAR, P. V.; ZENG, H.; SOLÓRZANO, A.; SWAYNE, D. E.; COX, N. J.; KATZ, J. M.; TAUBENBERGER, J. K.; PALESE, P.; GARCÍA-SASTRE, A. Characterization of the Reconstructed 1918 Spanish Influenza Pandemic Virus. **Science**, v. 310, p. 77-80, 2005.

6 CIOTTI, M.; CICCOZZI, M.; TERRINONI, A.; JIANG, W. C.; WANG, C. B.; BERNARDINI, S. The COVID-19 pandemic. **Critical Reviews in Clinical Laboratory Sciences**, v. 57, p. 365-388, 2020.

7 World Health Organization. **WHO COVID-19 dashboard**. Available on: https://data.who.int/dashboards/covid19/deaths?n=o Accessed on: 15 Feb. 2025.

8 JESTER, B.; UYEKI, T. M.; JERNIGAN, D. B.; TUMPEY, T. M. Historical and clinical aspects of the 1918 H1N1 pandemic in the United States. **Virology**, v. 527, p. 32-37, 2019.

9 FERGUSON, N. M.; FRASER, C.; DONNELY, C. A.; GHANI, A. C.; ANDERSON, R. M. Public Health Risk from the Avian H5N1 Influenza Epidemic. **Science**, v. 304, no. 5673, p. 968-969, 2004.

10 FAUCI, A. S. The AIDS Epidemic – Considerations for the 21st Century. **The New England Journal of Medicine**, v. 341, no. 14, p. 1046-1050, 1999.

11 KEELING, M. J.; ROHANI, P. **Modeling Infectious Diseases**: In humans and animals. 1. ed. Princeton: Princeton University Press, 2007.

12 FÁVARO, V. H. A.; GABRICK, E. C.; BATISTA, A. M.; CALDAS, I. L.; VIANA, R. L. Epidemiological model based on networks with non-local coupling. **Chaos, Solitons and Fractals**, v. 177, p. 114256, 2023.

13 SILVA, S. T.; GABRICK, E. C.; PROTACHEVICZ, P. R.; IAROSZ, K. C.; CALDAS, I. L.; BATISTA, A. M.; KURTHS, J. When climate variables improve the dengue forecasting: a machine learning approach. **The European Physical Journal Special Topics**, v. 2024, p. 1-15, 2024.

14 HOSSAIN, M. P.; JUNUS, A.; ZHU, X.; JIA, P.; WEN, T. H.; PFEIFFER, D.; YUAN, H. Y. The effects of border control and quarantine measures on the spread of COVID-19. **Epidemics**, v. 32, p. 100397, 2020.

15 YORKE, J. A.; HETHCOTE, H. W.; NOLD, A. Dynamics and control of the transmission of gonorrhea. **Sexually Transmitted Diseases**, v. 5, no. 2, p. 51-56, 1978.

16 IMAI, C.; ARMSTRONG, B.; CHALABI, Z.; MANGTANI, P.; HASHIZUME, M. Time series regression model for infectious disease and wheather. **Environmental Research**, v. 142, p. 319-327, 2015.

17 CARVAJAL, T. M.; VIACRUSIS, K. M.; HERNANDEZ, L. F. T.; HO, H. T.; AMALIN, D. M.; WATANABE, K. Machine learning methods reveal the temporal pattern of dengue incidence using meteorological factors in metropolitan Manila, Philippines. **BMC Infectious Diseases**, v. 18, no. 183, 2018.

18 BJORNSTAD, O. N. Epidemics: Models and Data using R. 1st. ed. Springer Cham, 2018.

19 KERMACK, W. O.; MCKENDRICK, A. G. A contribution to the mathematical theory of epidemics. **Proceedings of the Royal Society A**, v. 115, p. 700-721, 1927.

20 KERMACK, W. O.; MCKENDRICK, A. G. Contributions to the mathematical theory of epidemics. II. – The problem of endemicity **Proceedings of the Royal Society A**, v. 138, p. 55-83, 1932.

21 KERMACK, W. O.; MCKENDRICK, A. G. Contributions to the mathematical theory of epidemics – III. Further studies of the problem of endemicity **Proceedings of the Royal Society A**, v. 141A, p. 94-122, 1933.

22 MANCHEIN, C.; BRUGNAGO, E. L.; SILVA, R. M.; MENDES, C. F. O.; BEIMS, M. W. Strong correlations between power-law growth of COVID-19 in four continents and the inefficiency of soft quarantine strategies. **Chaos**, v. 30, no. 4, 2020.

23 BRUGNAGO, E. L.; SILVA, R. M.; MANCHEIN, C.; BEIMS, M. W. How relevant is the decision of containment measures against COVID-19 applied ahead of time? **Chaos, Solitons and Fractals**, v. 140, p. 110164, 2020.

24 KEELING, M. J.; GRENFELL, B. T. Understanding the persistence of measles: reconciling theory, simulation and observation. **Proceedings of the Royal Society B**, v. 269, p. 335-343, 2002.

25 ALTIZIER, S.; DOBSON, A.; HOSSEINI, P.; HUDSON, P.; PASCUAL, M.; ROHANI, P. Seasonality and the dynamics of infectious diseases. **Ecology Letters**, v. 9, p. 467-487, 2006.

26 BUONOMO, B.; CHITNIS, N.; d'ONOFRIO, A. Seasonality in epidemic models: a literature review. **Ricerche di Matematica**, vol. 67, p. 7-25, 2018.

27 HOSHEN, M. B.; MORSE, A. P. A weather-driven model of malaria transmission. **Malaria Journal**, v. 3, no. 32, 2004.

28 FINKENSTADT, B. F.; GRENFELL, B. T. Time series modelling of childhood diseases: a dynamical systems approach. **Journal of the Royal Statistical Society Series C Applied Statistics**, v. 49, no. 2, p. 187-205, 2000.

29 DAVE, K.; LEE, P. C. Global geographical and temporal patterns of seasonal influenza and associated climatic factors. **Epidemiologic Reviews**, v. 41, p. 51-68, 2019.

30 XIA, S.; GULLICKSON, C. C.; METCALF, C. J. E.; GRENFELL, B. T.; MINA, M. J. Assessing the Effects of Measles Virus Infections on Childhood Infectious Disease Mortality in Brazil. **The Journal of Infectious Diseases**, v. 227, p. 133-140, 2023.

31 AGUIAR, M.; STOLLENWERK, N.; KOOI, B. W. Torus bifurcations, isolas and chaotic attractors in a simple dengue fever model with ADE and temporary cross immunity. **International Journal of Computer Mathematics**, v. 86, no. 10-11, p. 1867-1877, 2009.

32 OLSEN, L. F.; SCHAFFER, W. M. Chaos Versus Noisy Periodicity: Alternative Hypotheses for Childhood Epidemics. **Science**, v. 249, n. 4968, p. 499-504, 1990.

33 GRENFELL, B.; KLECZKOWSKI, A.; GILLIGAN, C.; BOLKER, B. Spatial heterogeneity, nonlinear dynamics and chaos in infectious diseases. **Statistical Methods in Medical Research**, v.4, no. 2, p. 160-183, 1995.

34 GRENFELL, B.; BOLKER, B.; KLECZKOWSKI, A. Seasonality and extinction in chaotic metapopulations. **Proceedings of the Royal Society B**, v. 259, p. 97-103, 1995.

35 FISMAN, D. N. Seasonality of infectious diseases. **Annual Review of Public Health**, v. 28, p. 127-143, 2007.

36 DALZIEL, B. D.; BJORNSTAD, O. N.; VAN PANHUIS, W. G.; BURKE, D. S.; METCALF, C. J. E.; GRENFELL, B. T. Persistent chaos of measles epidemics in the prevaccination United States caused by a small change in seasonal transmission patterns. **Plos Computational Biology**, v. 12, no. 2, p. e1004655, 2016.

37 O'REGAN, S. M.; KELLY, T. C.; KOROBEINIKOV, A.; O'CALLAGHAN, M. J. A.; POKROVSKII, A. V.; RACHINSKII, D. Chaos in a seasonally perturbed SIR model: avian influenza in a seabird colony as a paradigm. **Journal of Mathematical Biology**, v. 67, p. 293-327, 2013.

38 KUZNETSOV, Y. A.; PICCARDI, C. Bifurcation analysis of periodic SEIR and SIR epidemic models. **Journal of Mathematical Biology**, v. 32, p. 109-121, 1994.

39 XUEYU, M.; ZHIQIANG, C.; SHUBIN, S.; DONGLI, D. Analysis of epidemic vaccination strategies on heterogeneous networks: Based on SEIRV model and evolutionary game. **Applied Mathematics and Computation**, v. 403, p. 126172, 2021.

40 MOLINARI, N. A. M.; ORTEGA-SANCHEZ, I. R.; MESSONNIER, M. L.; THOMPSON, W. W.; WORTLEY, P. M.; WEINTRAUB, E.; BRIDGES, C. B. The annual impact of seasonal influenza in the US: Measuring disease burden and costs. **Vaccine**, v. 25, no. 27, p. 5086-5096, 2007.

41 ATCHISON, C.; LOPMAN, B.; EDMUNDS, W. J. Modelling the seasonality of rotavirus disease and the impact of vaccination in England and Wales. **Vaccine**, v. 28, p. 3118–3126, 2010.

42 GAO, S.; LIU, Y.; NIETO, J. J.; ANDRADE, H. Seasonality and mixed vaccination strategy in an epidemic model with vertical transmission. **Mathematics and Computers in Simulation**, v. 81, p. 1855-1868, 2011.

43 SHULGIN, B.; STONE, L.; AGUR, Z. Pulse vaccination strategy in the SIR epidemic model. **Bulletin of Mathematical Biology**, v. 60, p. 1123-1148, 1998.

44 DUARTE, J,; JANUÁRIO, C.; MARTINS, N.; SEOANE, J. M.; SANJUÁN, M. A. F. Controlling Infectious Diseases: The Decisive Phase Effect on a Seasonal Vaccination Strategy. **International Journal of Bifurcation and Chaos**, v. 31, no. 15, p. 2130044, 2021.

45 AGUR, Z.; COJOCARU, L.; MAZOR, G.; ANDERSON, R. M.; DANON, Y. L. Pulse mass measles vaccination across age cohorts. **Proceedings of the National Academy of Sciences of the USA**, v. 90, p. 11698-11702, 1993.

46 HO, S. H.; HE, D.; EFTIMIE, R. Mathematical models of transmission dynamics and vaccine strategies in Hong Kong during the 2017-2018 winter influenza season. **Journal of Theoretical Biology**, v. 476, p. 74-94, 2019.

47 METCALF, C. J. E.; LESSLER, J.; KLEPAC, P.; CUTTS, F.; GRENFELL, B. T. Impact of birth rate, seasonality and transmission rate on minimum levels of coverage needed for rubella vaccination. **Epidemiology and Infection** , v. 140, no. 12, p. 2290-2301, 2012.

48 MONTEIRO, L. H. A. **Sistemas Dinâmicos**. 4th ed. São Paulo: Livraria da Física, 2019.

49 BOYCE, W. E.; DIPRIMA, R. C. **Elementary Differential Equations and Boundary Value Problems**. 10th ed. New Jersey: John Wiley and Sons Ltd, 2012.

50 ALLIGOOD, K. T.; SAUER, T. D.; YORKE, J. A. **Chaos**: An introduction to Dynamical Systems. 1st ed. New York: Springer, 1997.

51 TÉL, T.; GRUIZ, M. **Chaotic dynamics**: an introduction based on classical mechanics. Cambridge: Cambridge University Press; 2006.

52 STROGATZ, S. H. **Nonlinear Dynamics and Chaos**: Applications to Physics, Biology, Chemistry, and Engineering. 2 ed. CRC Press, Boca Raton, 2015.

53 TRAWICKI, M. B. Deterministic Seirs Epidemic Model for Modeling Vital Dynamics, Vaccinations, and Temporary Immunity. **Mathematics**, v. 5, p. 1-19, 2017.

54 HASSMAN, R. L.; MCCABE, I. M. H.; SMITH, K. M.; ALLEN, L. J. S. Stochastic Models of Zoonotic Avian Influenza with Multiple Hosts, Environmental Transmission, and Migration in the Natural Reservoir. **Bulletin of Mathematical Biology**, v. 87, p. 14, 2025.

55 MAY, R. M. Simple mathematical models with very complicated dynamics. **Nature**, v. 261, p. 459-467, 1976.

56 VIANA, R. L. **Introdução à Dinâmica Não-Linear e Caos**. Available on: https://www.105groupscience.com/materials. Last access 30th Dec. 2024.

57 WOLF, A.; SWIFT, J. B.; SWINNEY, H. L.; VASTANO, J. A. Determining Lyapunov exponents from a time series. **Physica D**, v. 16, p. 285-317, 1985.

58 BATISTA, A. M.; SOUZA, S. L. T.; IAROSZ, K. C.; ALMEIDA, A. C. L.; Jr SZEZECH, J. D.; GABRICK, E. C.; MUGNAINE, M.; SANTOS, G. L.; CALDAS I. L. Simulation of deterministic compartmental models for infectious diseases dynamics. **Revista Brasileira Ensino Física.**, v. 43, p. e20210171, 2021.

59 TOMÉ, T.; de OLIVEIRA, M. J. Epidemic spreading. **Revista Brasileira Ensino Física.**, v. 42, e20200259, 2020.

60 GREENHALGH, D.; MONEIM, I. A. SIRS Epidemic Model and Simulations Using Different Types of Seasonal Contact Rate. **Systems Analysis Modelling Simulation**, v. 43, n. 5, p. 573-600, 2003.

61 LÓPEZ, R.; KUANG, Y.; TRIDANE, A. A simple SI model with two age groups and its application to us HIV epidemics: to treat or not to treat? **Journal of Biological Systems**, v. 15, n. 2007, p. 169-184, 2007

62 RANA, P. S.; SHARMA, N. Mathematical modeling and stability analysis of a SI type model for HIV/AIDS. **Journal of Interdisciplinary Mathematics**, v. 23, p. 257-273, 2020.

63 NAKAMURA, G. M.; MARTINEZ, A. S. Hamiltonian dynamics of the SIS epidemic model with stochastic fluctuations. **Scientific Reports**, v. 9, n. 15841, 2019.

64 COOPER, I.; MONDAL, A.; ANTONOPOULOS, C. G. A SIR model assumption for the spread of COVID-19 in different communities. **Chaos, Solitons and Fractals**, v. 139, n. 110057, 2020.

65 GRENFELL, B. T.; BJORNSTAD, O. N.; FINKENSTÄDT, B. F. Dynamics of measles epidemics: scaling noise, determinism, and predictability with the TSIR model. **Ecological Monographs**, v. 72, p. 185-202, 2002.

66 SOUZA, D. R.; TOMÉ, T. Stochastic lattice gas model describing the dynamics of the SIRS epidemic process. **Physica A**, v. 389, p. 1142-1150, 2010.

67 GUEDES, A. R.; OLIVEIRA, M. S.; TAVARES, B. M.; LUNA-MUSCHI, A.; LAZARI, C. S.; MONTAL, A. C.; FARIA, E.; MAIA, F. L.; BARBOZA, A. S.; LEME, M. D.; TOMAZINI, F. M.; COSTA, S. F.; LEVIN, A. S. Reinfection rate in a cohort of healthcare workers over 2 years of the COVID-19 pandemic. **Scientific Reports**, v. 13, n. 712, 2023.

68 SHARMA, N.; VERMA, A. K.; GUPTA, A. K. Spatial network based model forecasting transmission and control of COVID-19. **Physica A**, v. 581, n. 126223, 2021.

69 AMAKU, M.; COVAS, D. T.; COUTINHO, F. A. B.; AZEVEDO, R. S.; MASSAD, E. Modelling the impact of delaying vaccination against SARS-CoV-2 assuming unlimited vaccine supply. **Theoretical Biology and Medical Modelling**, v. 18, n. 14, 2021.

70 GABRICK, E. C.; PROTACHEVICZ, P. R.; BATISTA, A. M.; IAROSZ, K. C.; SOUZA, S. L. T.; ALMEIDA, A. C. L.; SZEZECH Jr, J. D.; MUGNAINE, M.; CALDAS, I. L. Effect of two vaccine doses in the SEIR epidemic model using a stochastic cellular automaton. **Physica A**, v. 597, n. 127258, 2022.

71 SOUZA, S. L. T.; BATISTA, A. M.; CALDAS, I. L.; IAROSZ, K. C.; SZEZECH Jr, J. D. Dynamics of epidemics: Impact of easing restrictions and control of infection spread. **Chaos, Solitons and Fractals**, v. 142, n. 110431, 2021.

72 MUGNAINE, M.; GABRICK, E. C.; PROTACHEVICZ, P. R.; IAROSZ, K. C.; SOUZA S. L. T.; ALMEIDA, A. C. L.; BATISTA, A. M.; CALDAS, I. L.; Jr SZEZECH, J. D.; VIANA, R. L. Control attenuation and temporary immunity in a cellular automata SEIR mode. **Chaos, Solitons and Fractals**, v. 155, n. 111784, 2022.

73 CARCIONE, J. M.; SANTOS, J. E.; BAGAINI, C.; BA, J. A Simulation of a COVID-19 Epidemic Based on a Deterministic SEIR Model. **Frontiers in Public Health**, v. 8, n. 239, 2020.

74 DAI, J.; ZHAI, C.; AI, J.; MA, J.; WAND, J.; SUN, W. Modeling the spread of epidemics based on Cellular Automata. **Processes**, v. 9, p. 2227-9717, 2021.

75 AMAKU, M.; COVAS, D. T.; COUTINHO, F. A. B.; NETO, R. S. A.; STRUCHINER, C.; WILDER-SMITH, A.; MASSAD, E. Modelling the test, trace and quarantine strategy to control the COVID-19 epidemic in the state of São Paulo, Brazil. **Infectious Disease Modelling**, v. 6, p. 46-55, 2021.

76 SAFI, M. A.; GUMEL, A. B. Mathematical analysis of a disease transmission model with quarantine, isolation and an imperfect vaccine. **Computers and Mathematics with Applications**, v. 61, no. 10, p. 3044-3070, 2011.

77 STEINDORF, V.; SRIVASTAV, A. K.; STOLLENWERK, N.; KOOI, B.; AGUIAR, M. Modeling secondary infections with temporary immunity and disease enhancement factor: Mechanisms for complex dynamics in simple epidemiological models. **Chaos, Solitons and Fractals**, v. 164, p. 112709, 2022.

78 MARQUIONI, V. M.; AGUIAR, M. A. M. Modeling neutral viral mutations in the spread of SARS-CoV-2 epidemics. **Plos One**, v. 16, no. 7, p. 1-18, 2021.

79 LÓPEZ-FLORES, M. M.; MARCHESIN, D.; MATOS, V.; SCHECTER, S. **Equações diferenciais e modelos epidemiológicos**. 1. ed. Editora do IMPA, 2021.

80 ANDERSON, R. M.; MAY, R. M. **Infectious diseases of humans**: Dynamics and control. Oxford University Press, Oxford, 1991.

81 EL-SAKA, H. The fractional-order sis epidemic model with variable population size. **Journal of the Egyptian Mathematical Society**, v. 22, p. 50-54, 2014.

82 HETHCOTE, H. W.; YORKE, J. A. **Gonorrhea Transmission Dynamics and Control**. 1st Edition, Springer Berlin, Heidelberg, 1984.

83 DIAN, Z.; SUN, Y.; ZHANG, G.; XU, Y.; FAN, X.; YANG, X.; PAN, Q.; PEPPE-LENBOSCH, M.; MIAO, Z. Rotavirus-related systemic diseases: clinical manifestation, evidence and pathogenesis. **Critical Reviews in Microbiology**, v. 47, 580-595, 2021.

84 FENG, X.; LIU, L.; TANG, S.; HUO, X. Stability and bifurcation analysis of a two-patch SIS model on nosocomial infections. **Applied Mathematics Letters**, v. 102, n. 106097, 2020.

85 HETHCOTE, H. W.; VAN DEN DRIESSCHE, P. An SIS epidemic model with variable population size and a delay. **Journal of Mathematical Biology**, v. 34, p. 177-194, 1995.

86 METCALF, C. J. E.; BJORNSTAD, O. N.; GRENFELL, B. T.; ANDREASEN, V. Seasonality and comparative dynamics of six childhood infections in pre-vaccination Copenhagen. **Proceedings of the Royal Society B**, v. 276, p. 4111-4118, 2009.

87 HALE, J. K. **Ordinary Differential Equations**. Wiley, New York, 1969.

88 QUAN-XING, L.; CHEN, J. Cellular automata modelling of SEIRS. **Chinese Physics**, v. 14, n. 1370, 2005.

89 SHARMA, N.; GUPTA, A. K. Impact of time delay on the dynamics of SEIR epidemic model using cellular automata. **Physica A**, v. 471, p. 114-125, 2017.

90 WOLFRAM, S. **Cellular automata and complexity: collected papers**. 1. ed. Reading, MA: Addison-Wesley, 1994.

91 WOLFRAM, S. Statistical mechanics of cellular automata. **Reviews of Modern Physics**, v. 55, n. 601, 1983.

92 WOLFRAM, S. **Cellular Automata.** Los Alamos Science, Los Alamos, 1983.

93 SCHNECKENREITHER, G.; POPPER, B.; ZAUNER, G.; BREITENECKER, F. Modelling SIR-type epidemics by ODEs, PDEs, difference equations and cellular automata – A comparative study. **Simulation Modelling Practice and Theory**, v. 16, p. 1014-1023, 2008.

94 BORGES, F. S.; PROTACHEVICZ, P. R.; SANTOS, V.; SANTOS, M. S.; GABRICK, E. C.; IAROSZ, K. C.; LAMEU, E. L.; BAPTISTA, M. S.; CALDAS, I. L.; BATISTA, A. M. Influence of inhibitory synapses on the criticality of excitable neuronal networks. **Indian Academy of Sciences Conference Series**, v. 3, 2020.

95 ILACHISNKI, A. **Cellular automata: a discrete universe**. World Scientific, 2001.

96 GABRICK, E. C.; SAYARI, E.; PROTACHEVICZ, P. R.; SZEZECH Jr., J. D.; IAROSZ, K. C.; SOUZA, S. L. T.; ALMEIDA, A. C. L.; VIANA, R. L.; CALDAS, I. L.; BATISTA, A. M. Unpredictability in seasonal infectious diseases spread. **Chaos, Solitons and Fractals**, v. 166, p. 113001, 2023.

97 BRUGNAGO, E. L.; GABRICK, E. C.; IAROSZ, K. C.; SZEZECH Jr., J. D.; VIANA, R. L.; BATISTA, A. M.; CALDAS, I. L. Multistability and chaos in SEIRS epidemic model with a periodic time-dependent transmission rate. **Chaos**, v. 33, p. 123123, 2023.

98 GRASSLY, N. C.; FRASER, C. Seasonal infectious disease epidemiology. **Proceedings of the Royal Society**, v. 273, p. 2541-2550, 2006.

99 THOMPSON, W. W.; COMANOR, L.; SHAY, D. K. Epidemiology of Seasonal Influenza: Use of Surveillance Data and Statistical Models to Estimate the Burden of Disease. **The Journal of Infectious Diseases**, v. 194, n. 2, p. S82–S91, 2006.

100 KEELING, M. J.; GRENFELL, B. T. Disease Extinction and Community Size: Modeling the Persistence of Measles. **Science**, v. 275, n. 5296, p. 65-67, 1997.

101 BAI, Z.; ZHOU, Y. Global dynamics of an SEIRS epidemic model with periodic vaccination and seasonal contact rate. **Nonlinear Analysis: Real World Applications**, v. 13, p. 1060–1068, 2012.

102 YI, N.; ZHANG, Q.; MAO, K.; YANG, D.; LI, Q. Analysis and control of an SEIR epidemic system with nonlinear transmission rate. **Mathematical and Computer Modelling**, v. 50, p. 1498-1513, 2009.

103 TANAKA, G.; AIHARA, K. Effects of seasonal variation patterns on recurrent outbreaks in epidemic models. **Journal of Theoretical Biology**, v. 317, p. 87-95, 2013.

104 MA, J.; MA, Z. Epidemic threshold conditions for seasonally forced SEIR models. **Mathematical Biosciences and Engineering**, v. 3, n. 161, 2006.

105 BILAL, S.; SINGH, B. K.; PRASAD, A.; MICHAEL, E. Effects of quasiperiodic forcing in epidemic models. **Chaos**, v. 26, n. 093115, 2016.

106 FEUDEL, U.; GREBOGI, C. Multistability and the control of complexity . **Chaos**, v. 7, p. 597–604, 1997.

107 FEUDEL, U.; GREBOGI, C. Why Are Chaotic Attractors Rare in Multistable Systems? **Physical Review Letters**, v. 91, n. 134102, 2003.

108 FEUDEL, U. Complex dynamics in multistable systems. **International Journal of Bifurcation and Chaos**, v. 18, n. 6, p. 1607-1626, 2008.

109 MEDEIROS, E. S.; CALDAS, I. L.; BAPTISTA, M. S.; FEUDEL, U. Trapping Phenomenon Attenuates the Consequences of Tipping Points for Limit Cycles. **Scientific Reports**, v. 7, n. 42351, 2017.

110 LESSLER, J.; REICH, N. G.; BROOKMEYER, R.; PERL, T. M.; NELSON, K. E.; CUMMINGS, D. A. T. Incubation periods of acute respiratory viral infections: a systematic review. **The Lancet Infectious Diseases**, v. 9, p. 291-300, 2009.

111 GREBOGI, C.; OTT, E.; YORKE, J. A. Crises, sudden changes in chaotic attractors, and transient chaos. **Physica D: Nonlinear Phenomena**, v. 7, p. 181-200, 1983.

112 GREBOGI, C.; OTT, E.; YORKE, J. A. Chaotic Attractors in Crisis. **Physical Review Letters**, v. 48, n. 1507, 1982.

113 TÉL, T.; LAI, Y. C. Chaotic transients in spatially extended systems. **Physics Reports**, v. 460, p. 245-275, 2008.

114 STOLLENWERK, N.; AGUIAR, M.; BALLESTEROS, S.; BOTO, J.; KOOI, B.; MATEUS, L. Dynamic noise, chaos and parameter estimation in population biology. **Interface Focus**, v. 2, p. 156-169, 2012.

115 SCARPINO, S. V.; PETRI, G. On the predictability of infectious disease outbreaks. **Nature Communications**, v. 10, n. 898, 2019.

116 VAN NES, E. H.; ARANI, B. M. S.; STAAL, A.; VAN DER BOLT, B.; FLORES, B. M.; BATHIANY, S.; SCHEFFER, M. What Do You Mean, 'Tipping Point'? **Trends in Ecology and Evolution**, v. 31, p. 902-904, 2016.

117 DAKOS, V.; MATTHEWS, B.; HENDRY, A. P.; LEVINE, J.; LOEUILLE, N.; NORBERG, J.; NOSIL, P.; SCHEFFER, M.; DE MEESTER, L. Ecosystem tipping points in an evolving world. **Nature Ecology and Evolution**, v. 3, p. 355-362, 2019.

118 GABRICK, E. C.; BRUGNAGO, E. L.; DE SOUZA, S. L. T.; IAROSZ, K. C.; SZEZECH JR., J. D.; VIANA, R. L.; CALDAS, I. L.; BATISTA, A. M.; KURTHS, J. Impact of periodic vaccination in SEIRS seasonal model. **Chaos**, v. 34, p. 013137, 2024.

119 GABRICK, E. C.; BRUGNAGO, E. L.; MORAES, A. L. R.; PROTACHEVICZ, P. R.; SILVA, S. T.; BORGES, F. S.; CALDAS, I. L.; BATISTA, A. M.; KURTHS, J. Control, bi-stability, and preference for chaos in time-dependent vaccination campaign. **Chaos**, v. 34, p. 093118, 2024.

120 GRABENSTEIN, J. D.; NEVIN, R. L. Mass Immunization Programs: Principles and Standards. **CTMI**, v. 304, p. 31-51, 2006.

121 MCLEAN, A. R.; ANDERSON, R. M. Measles in developing countries. Part II. The predicted impact of mass vaccination. **Epidemiology and Infection**, v. 100, no. 3, p. 419-442, 1998.

122 FENNER, F.; HENDERSON, D. A.; ARITA, I.; JEZEK, Z.; LADNYI, I. D. World Health Organization. Smallpox and its eradication. **History of international public health**, v. 6, p. 1371-1409, 1998.

123 BAGCCHI, S. The world's largest COVID-19 vaccination campaign. **The Lancet Infectious Diseases**, v. 21, no. 3, p. 323, 2021.

124 MONEIM, I. A.; GREENHALGH, D. Use of a periodic vaccination strategy to control the spread of epidemics with seasonally varying contact rate. **Mathematical Biosciences and Engineering**, v. 2, n. 3, p. 591-611, 2005.

125 MEINSMA, G. Elementary proof of the Routh-Hurwitz test. **Systems and Control Letters**, v. 25, p. 237-242, 1995.

126 GALLAS, J. A. C. Dissecting shrimps: results for some one-dimensional physical models. **Physica A**, v. 202, p. 196-223, 1994.

127 MARTINS, L. C.; GALLAS, J. A. C. Multistability, phase diagrams and statistical properties of the kicked rotor: a map with many coexisting attractors. **International Journal of Bifurcation and Chaos**, v. 18, p. 1705-1717, 2008.

128 GALLAS, J. A. C. Structure of the parameter space of the Hénon map. **Physical Review Letters**, v. 70, n. 18, 2714, 1993.

129 CASTRO, V.; MONTI, M.; PARDO, W. B.; WALKENSTEIN, J. A.; ROSA JR, E. Characterization of the Rössler system in parameter space. **International Journal of Bifurcation and Chaos**, v. 17, n. 3, p. 965-973, 2007.

130 BARRIO, R.; BLESA, F.; SERRANO, S.; SHILNIKOV, A. Global organization of spiral structures in biparameter space of dissipative systems with Shilnikov saddle-foci. **Physical Review E**, v. 84, n. 3, 035201, 2011.

131 RECH, P. C. How to embed shrimps in parameter planes of the Lorenz system. **Physica Scripta**, v. 92, 045201, 2017.

132 VARGA, R.; KLAPCSIK, K.; HEGEDÜS, F. Route to shrimps: Dissipation driven formation of shrimp-shaped domains. **Chaos, Solitons and Fractals**, v. 130, 109424, 2020.

133 GALLAS, J. A. C. Degenerate routes to chaos. **Physical Review E**, v. 48, p. R4156(R), 1993.

134 GALLAS, J. A. C. Structure of the parameter space of a ring cavity. **Applied Physics B: Lasers and Optics**, v. 60, p. S203-S213, 1995.